

First principles based multiparadigm modeling of electronic structures and dynamics

Thesis by

Hai Xiao

In Partial Fulfillment of the Requirements

for the Degree of

Doctor of Philosophy



California Institute of Technology

Pasadena, California

2015

(Defended January 15, 2015)

© 2015

Hai Xiao

All Rights Reserved

To the memory of my grandma Ding-Xiang and grandpa Yong-Chu
and
to my wife Ying and our son Jun

Acknowledgments

I wish to thank my advisor, Prof. Bill Goddard, for his constant support and guidance over the past six years. I appreciate very much the flexibility Bill offered me in both choosing research topics and working pace, as well as the broad knowledge of theory, modeling, and experiments he shared with me, and the key ideas he proposed that greatly sped up my research progress.

I would like to thank other group members I have collaborated with: Julius T. Su, Jamil Tahir-Kheli, Andrés Jaramillo-Botero, Patrick L. Theofanis, Sergey V. Zybin, Wei-Guang Liu, Qi An, and Sijia Dong. Additionally, I have also enjoyed in our group chatting and friendship with Mu-Jeng Cheng, Sha Yao, Wei-Guang Liu, Qi An, Yi Liu, Ted Yu, Himanshu Mishra, Fan Liu, Lianchi Liu, Tingting Zhou, Vaclav Cvicek, Ho-Cheng Tsai, Tao Cheng, Sijia Dong, and José Mendoza-Cortes. It's quite a pleasure being a member of this big family.

I would like to thank my committee members, Prof. Harry Gray, Prof. Rudy Marcus, and Prof. Nate Lewis, for constructive comments and discussions on my candidacy, proposals, and thesis. I would also like to thank my candidacy committee chair, Prof. Aron Kuppermann, who is not with us any more, for his caring about both my research and life in the early stage of my graduate student life.

I would love to thank all my friends, though it's too big a list to put here, for helping me get through rough times and enriching my life these years.

Finally I would like to thank my parents for unconditional love and support, and I wish to thank my wife Ying. Ying and I have been together for more than ten years, and I dread to think what my life would be without her. I would very much love to dedicate this thesis to her and our beloved son Jun.

List of Abbreviations

QM	quantum mechanics
BO	Born-Oppenheimer
PES	potential energy surface
MD	molecular dynamics
HF	Hartree-Fock
UHF	unrestricted Hartree-Fock
VB	valence bond
GVB	generalized valence bond
TDHF	time-dependent Hartree-Fock
DFT	density functional theory
TDDFT	time-dependent density functional theory
KS	Kohn-Sham
GKS	generalized Kohn-Sham
XC	exchange and correlation
LDA	local density approximation
GGA	generalized gradient approximation
meta-GGA	meta-generalized gradient approximation
AO	atomic orbital
MO	molecular orbital
HOMO	highest occupied molecular orbital
LUMO	lowest unoccupied molecular orbital
VBM	valence band maximum
CBM	conduction band minimum
VBO	valence band offset
CBO	conduction band offset
DOS	density of states
SOC	spin-orbit coupling
ECP	effective core potential

USPP	u ltrasoft p seudopotential
PAW	p rojector a ugmented- w ave
BSSE	b asis set s uperposition e rror
PBC	p eriodic b oundary c onditions
IP	i onization p otential
EA	e lectron a ffinity
AEP	a verage e lectrostatic p otential
EOS	e quation o f s tate
ZPE	z ero p oint e nergy
TS	t ransition s tate
eFF	e lectron f orce f ield
FSG	f loating s pherical G aussian
EOM	e quations o f m otion
GHA-QM	G aussian H artree a pproximated q uantum m echanics
AMPERE	a ngular m omentum p rojected e ffective c ore p seudopotential
MAD	m ean a bsolute d eviation
MRD	m ean r elative d eviation
RMSD	r oot m ean s quare d eviation
GA	g enetic a lgorithm
<i>n</i>D	<i>n</i> = 0, 1, 2, 3 d imensional
CIGS	CuIn_{<i>x</i>}Ga_{1-<i>x</i>}Se₂

Abstract

Electronic structures and dynamics are the key to linking the material composition and structure to functionality and performance.

An essential issue in developing semiconductor devices for photovoltaics is to design materials with optimal band gaps and relative positioning of band levels. Approximate DFT methods have been justified to predict band gaps from KS/GKS eigenvalues, but the accuracy is decisively dependent on the choice of XC functionals. We show here for CuInSe_2 and CuGaSe_2 , the parent compounds of the promising CIGS solar cells, conventional LDA and GGA obtain gaps of 0.0–0.01 and 0.02–0.24 eV (versus experimental values of 1.04 and 1.67 eV), while the historically first global hybrid functional, B3PW91, is surprisingly the best, with band gaps of 1.07 and 1.58 eV. Furthermore, we show that for 27 related binary and ternary semiconductors, B3PW91 predicts gaps with a MAD of only 0.09 eV, which is substantially better than all modern hybrid functionals, including B3LYP (MAD of 0.19 eV) and screened hybrid functional HSE06 (MAD of 0.18 eV).

The laboratory performance of CIGS solar cells ($> 20\%$ efficiency) makes them promising candidate photovoltaic devices. However, there remains little understanding of how defects at the CIGS/CdS interface affect the band offsets and interfacial energies, and hence the performance of manufactured devices. To determine these relationships, we use the B3PW91 hybrid functional of DFT with the AEP method that we validate to provide very accurate descriptions of both band gaps and band offsets. This confirms the weak dependence of band offsets on surface orientation observed experimentally. We predict that the CBO of perfect $\text{CuInSe}_2/\text{CdS}$ interface is large, 0.79 eV, which would dramatically degrade performance. Moreover we show that band gap widening induced by Ga adjusts only the VBO, and we find that Cd impurities do not significantly affect the CBO. Thus we show that Cu vacancies at the interface play the key role in enabling the tunability of CBO. We predict that Na further improves the CBO through electrostatically elevating the valence levels to decrease the CBO, explaining the observed essential role of Na for high performance. Moreover we find that K leads to a dramatic decrease in the CBO to 0.05 eV, much better than Na. We suggest that the efficiency of CIGS devices might be improved substantially by tuning the ratio of Na to K, with the improved phase stability of Na balancing phase instability from K. All these defects reduce interfacial stability slightly, but not significantly.

A number of exotic structures have been formed through high pressure chemistry, but applications have been hindered by difficulties in recovering the high pressure phase to ambient conditions (i.e., one atmosphere and room temperature). Here we use dispersion-corrected DFT (PBE-*ulg* flavor) to predict that above 60 GPa the most stable form of N₂O (the laughing gas in its molecular form) is a 1D polymer with an all-nitrogen backbone analogous to *cis*-polyacetylene in which alternate N are bonded (ionic covalent) to O. The analogous *trans*-polymer is only 0.03–0.10 eV/molecular unit less stable. Upon relaxation to ambient conditions both polymers relax below 14 GPa to the same stable non-planar *trans*-polymer, accompanied by possible electronic structure transitions. The predicted phonon spectrum and dissociation kinetics validate the stability of this *trans*-poly-NNO at ambient conditions, which has potential applications as a new type of conducting polymer with all-nitrogen chains and as a high-energy oxidizer for rocket propulsion. This work illustrates *in silico* materials discovery particularly in the realm of extreme conditions.

Modeling non-adiabatic electron dynamics has been a long-standing challenge for computational chemistry and materials science, and the eFF method presents a cost-efficient alternative. However, due to the deficiency of FSG representation, eFF is limited to low- Z elements with electrons of predominant s -character. To overcome this, we introduce a formal set of ECP extensions that enable accurate description of p -block elements. The extensions consist of a model representing the core electrons with the nucleus as a single pseudo particle represented by FSG, interacting with valence electrons through ECPs. We demonstrate and validate the ECP extensions for complex bonding structures, geometries, and energetics of systems with p -block character (C, O, Al, Si) and apply them to study materials under extreme mechanical loading conditions.

Despite its success, the eFF framework has some limitations, originated from both the design of Pauli potentials and the FSG representation. To overcome these, we develop a new framework of two-level hierarchy that is a more rigorous and accurate successor to the eFF method. The fundamental level, GHA-QM, is based on a new set of Pauli potentials that renders exact QM level of accuracy for any FSG represented electron systems. To achieve this, we start with using exactly derived energy expressions for the same spin electron pair, and fitting a simple functional form, inspired by DFT, against open singlet electron pair curves (H₂ systems). Symmetric and asymmetric scaling factors are then introduced at this level to recover the QM total energies of multiple electron pair systems from the sum of local interactions. To complement the imperfect FSG representation, the AMPERE extension is implemented, and aims at embedding the interactions associated with both the cusp condition and explicit nodal structures. The whole GHA-QM+AMPERE framework is tested on H element, and the preliminary results are promising.

Contents

Acknowledgments	iv
List of Abbreviations	v
Abstract	vii
List of Figures	xi
List of Tables	xiii
1 Introduction	1
References	2
2 Accurate description of electronic structures for semiconductors from DFT	3
2.1 Fundamental band gap from KS/GKS scheme in DFT	4
2.2 Choice of basis sets and ECPs for periodic calculations	6
2.3 Key ingredients in XC functionals for performance	8
2.4 Benchmark on a set of 27 binary and ternary semiconductors	11
2.5 Concluding remarks	15
Appendix	15
References	21
3 Predicted roles of defects in band offsets and energetics at CIGS Solar Cell interfaces and implications for improving performance	27
3.1 Methodology for calculating band offsets from interface modeling	28
3.2 Band offsets at pristine CIGS/CdS interfaces	31
3.3 Bulk structures of defect CIGS	33
3.4 Roles of defects in band offsets and energetics at CIGS/CdS interfaces	36
3.5 Concluding remarks	38
Appendix	39
References	43

4	Formation of the $-\text{N}(\text{NO})\text{N}(\text{NO})-$ polymer at high pressure and stabilization at ambient conditions	49
4.1	Search for extended solid phases of N_2O under high pressures	50
4.2	Transitions between molecular, ionic, and polymer phases of N_2O	51
4.3	Relaxation of polymer phases to ambient conditions	54
4.4	Kinetic stability of the non-planar N_2O polymer at ambient conditions	59
4.5	Concluding remarks	60
	Appendix	61
	References	63
5	Development of ECP for eFF to extend application to high-Z elements	67
5.1	Formulation of ECP models in eFF	69
5.2	Performance of optimized eFF-ECP parameters	72
5.2.1	Al and Si with s - s ECP	73
5.2.2	C with s - p ECP	75
5.2.3	Oxygen with s - p ECP	78
5.2.4	Silicon carbide with combined s - s and s - p eFF-ECP	80
5.3	Conclusions	81
	References	82
6	Gaussian Hartree approximated QM with angular momentum projected effective core pseudopotential	85
6.1	Exact QM energies of same spin FSG electron pair	86
6.2	Symmetric and asymmetric scaling factors for same spin Pauli potential	90
6.3	Design of opposite spin Pauli potential	93
6.4	The AMPERE extension	97
6.5	Concluding remarks and future work	101
	Appendix	101
	A. Series expansions of ΔT , ΔC_{ee} , and ΔC_{ne}	101
	B. A hybrid scheme to construct opposite spin Pauli potential	102
	C. Integrals involved in energy evaluation with AMPERE	105
	D. Numerical implementation of AMPERE (<code>pair_eff_ecp.h</code>) in LAMMPS	108
	References	114

List of Figures

2.1	The band structure and DOS of CuInSe ₂ calculated with B3PW91.	9
2.2	The band structure and DOS of CuGaSe ₂ calculated with B3PW91.	10
3.1	Illustration of the computation of band offsets for the CuInSe ₂ /CdS (110) interface.	30
3.2	The CuInSe ₂ /CdS (112) polar interface model and the calculated band alignment. .	32
3.3	The interface models and calculated band alignments of CuIn _{0.75} Ga _{0.25} Se ₂ /CdS. . .	33
3.4	DOS of Cu-rich CuInSe ₂ shows the dominance of Cu 3 <i>d</i> in the valence region. . . .	34
3.5	The lowest energy model crystal structures for Cu ₅ In ₉ Se ₁₆ and CuIn ₅ Se ₈	35
3.6	The interface models and calculated band alignments of Cu ₅ In ₉ Se ₁₆ /CdS and CuIn ₅ Se ₈ /CdS.	36
3.7	DOS of Cu-poor CuIn ₅ Se ₈ shows the dominance of Se 4 <i>p</i> in the valence region. . . .	37
3.8	The interface models and calculated band alignments of Na ₂ Cu ₃ In ₉ Se ₁₆ /CdS, K ₂ Cu ₃ In ₉ Se ₁₆ /CdS and CdCu ₃ In ₉ Se ₁₆ /CdS.	38
4.1	Illustration of crystal structures and chemical formulations of a single chain for planar <i>cis</i> -polymer and planar <i>trans</i> -polymer.	51
4.2	Ground state enthalpy as a function of pressure predicted for various phases of N ₂ O.	52
4.3	Comparison between PBE- <i>ulg</i> calculated and experimental EOSs for molecular phases of N ₂ O.	53
4.4	Illustration of the orthorhombic crystal structure of ionic NO ⁺ NO ₃ ⁻ with space group <i>Pna2</i> ₁	54
4.5	The effect of quantum ZPE and temperature (entropy) on the transition pressure to polymer phase <i>P_c</i>	55
4.6	Phonon spectra for polymer phases of N ₂ O predicted at 80 and 0 GPa.	56
4.7	Illustration of crystal structure and chemical formulation of a single chain for non- planar <i>trans</i> -polymer.	57
4.8	Band gap and neighboring N–N bond length difference predicted as functions of pres- sure for all three polymer phases of N ₂ O at ground states.	58

4.9	Total and partial electronic DOSs calculated with B3PW91 for planar <i>cis</i> - and <i>trans</i> -polymers at 80 GPa.	58
4.10	Reaction path calculated for dissociation of the model oligomer.	59
4.A1	EOSs for various phases of N ₂ O at ground states.	61
4.A2	TS calculated for dissociation of an isolated periodic infinite chain of the non-planar polymer.	61
5.1	eFF aims at long term and large scale non-adiabatic MD simulations.	68
5.2	Illustration of distances used in the two functional types of ECP.	70
5.3	Comparison of cluster bond energies for different Al _n H _{3n} clusters.	74
5.4	Crack tip velocity versus reduced load for {111} fracture from eFF-ECP, compared to experimental, ReaxFF+Tersoff simulations, and DCET and EDIP data.	75
5.5	Mechanism of local field-induced ionization.	76
5.6	Gallery of molecules with conjugate double bonds.	77
5.7	Comparison of various methods on the binding curve along the dispersion <i>c</i> axis of graphite.	78
5.8	Illustration of electronic excitation-induced desorption of hydrogen from a passivated diamond slab.	79
5.9	Open shell like representation of lone pairs in eFF-ECP.	79
6.1	Comparison of different energy contributions upon antisymmetrization for total energies of triplet H ₂ system.	88
6.2	Comparison of different energy contributions upon antisymmetrization for optimizing electron wavefunctions of triplet H ₂ system.	89
6.3	Benchmark of eFF, GHA-QM with and without scaling.	90
6.4	Performance of symmetric scaling factor functions.	92
6.5	Performance of asymmetric scaling factor functions.	92
6.6	Fitting of opposite spin Pauli potential against open singlet H ₂ at B3LYP level.	94
6.7	Performance of GHA-QM on the open singlet and triplet H ₂ systems.	95
6.8	Performance of GHA-QM on symmetric stretching in <i>D</i> _{∞h} H ₃ and <i>D</i> _{4h} H ₄	96
6.9	Performance of GHA-QM on asymmetric stretching in <i>D</i> _{∞h} H ₃ and <i>D</i> _{4h} H ₄	96
6.10	Decomposition of valence FSG wavefunction into core-centered orbitals with various angular momenta.	98
6.11	Performance of GHA-QM+AMPERE on the dissociation curve of H ₂ molecule.	100
6.B1	Performance of fitting of prefactors on open singlet H ₂ at UHF level.	103
6.B2	Performance of the hybrid scheme on open singlet H ₂ at UHF and B3LYP levels.	104

List of Tables

2.1	Comparison of the performance of pruned and optimized basis sets on structures and band gaps of CuInSe ₂ , CuGaSe ₂ , and CdS.	7
2.2	Predicted band gap and lattice parameters for CuInSe ₂ chalcopyrite crystal from various levels of XC functionals.	9
2.3	Predicted band gap and lattice parameters for CuGaSe ₂ chalcopyrite crystal from various levels of XC functionals.	10
2.4	Predicted band gaps (eV) for 27 semiconductors with B3PW91 (MAD = 0.09 eV). . .	12
2.5	Predicted lattice parameters ($a/\text{\AA}$) for 9 binary semiconductors with B3PW91 (MRD = 1.9%).	12
2.6	Predicted lattice parameters for 18 ternary semiconductors with B3PW91 (MRD = 2.2%).	12
2.7	Predicted band gaps (eV) for 27 semiconductors with B3LYP (MAD = 0.19 eV). . .	13
2.8	Predicted lattice parameters ($a/\text{\AA}$) for 9 binary semiconductors with B3LYP (MRD = 3.1%).	13
2.9	Predicted lattice parameters for 18 ternary semiconductors with B3LYP (MRD = 3.6%).	13
2.10	Predicted band gaps (eV) for 27 semiconductors with HSE06 (MAD = 0.18 eV). . .	14
2.11	Predicted lattice parameters ($a/\text{\AA}$) for 9 binary semiconductors with HSE06 (MRD = 1.6%).	14
2.12	Predicted lattice parameters for 18 ternary semiconductors with HSE06 (MRD = 2.0%).	14
3.1	Convergence of interface thickness (d), interfacial energy (σ), VBO (ΔE_v), and CBO (ΔE_c) with respect to number of layers of each side (L) and the interface-interface distance (D) for CuInSe ₂ /CdS interfaces parallel to (110) and (112).	31
3.2	Fluctuations in calculated CBO values from using core levels of different elements. . .	32
3.3	Relative energies (ΔE) in meV/atom of all possible configurations within a $\sqrt{2} \times \sqrt{2} \times 1$ supercell for Cu ₅ In ₉ Se ₁₆ phase calculated with B3PW91.	35
3.4	Relative energies (ΔE) in meV/atom of low energy configurations for CuIn ₅ Se ₈ phase calculated with B3PW91 and PBE.	35

5.1	eFF-ECP parameters optimized for a few 2 nd and 3 rd row <i>p</i> -block elements.	72
5.2	Comparison of eFF-ECP, all electron eFF and DFT calculations on aluminum hydrides.	73
5.3	Comparison of eFF-ECP and eFF on geometries of carbon-containing molecular and bulk systems.	76
5.4	Performance of eFF-ECP on geometries of various molecules with oxygen atom(s). . .	80
5.5	Carbon <i>s-p</i> functional form parameters in the SiC-ECP force field and Silicon <i>s-s</i> parameters from Ref. [8].	80
5.6	Silicon Carbide training set and optimization results using the <i>s-p</i> form ECP for Carbon.	81
6.1	Fitted parameters for asymmetric scaling factor functions.	91
6.2	Fitted parameters for $E_{\text{Pauli}}^{\text{base}}(\uparrow\downarrow)$	94
6.B1	Fitted parameters for the prefactors at UHF level.	104

Chapter 1

Introduction

There is no doubt that MO and VB theory play a pivotal role in shaping chemists' understanding of chemistry, and elegant models and concepts have been derived, such as resonance, hybridization, VSEPR theory, Walsh diagram, ligand field theory, and frontier MO theory, to name but a few. Electronic structure, as a more generalized term, naturally covers the concepts ranging from orbital and bonding of finite molecules to bands and DOS of extended phases, and thus provides a bridging concept between chemistry and material science. Such crossing has led to insightful perspective and delicate understanding (see, e.g., [1] and [2]). Modern computational modeling techniques have enabled accurate quantitative description of electronic structures, which is the key to unveiling the relationship between chemical composition and material functionality. The first half of this thesis (Ch. 2–Ch. 4) is devoted to such research, in which predictions were made for the dependence of device performance on underlying material composition and the formation of novel functional material, through understanding the electronic structures by using DFT methods. As a preliminary, Ch. 2 discusses the physical significance of HOMO (VBM) and LUMO (CBM) from approximate DFT, and then elaborates on our choices of methodology based on benchmark calculations. Subsequently, Ch. 3 presents our appreciation of CIGS solar cell performance via modeling of band offsets across the CIGS/CdS interfaces, and Ch. 4 proposes a novel N₂O polymer, with alternating single and double bonds along the all-nitrogen backbone, which is formed under high pressures and stabilized by conformational relaxation at ambient conditions, and its electronic structure transition associated with structural change is discussed in details.

Accurate first principles methods such as DFT are currently capable of handling up to thousands of atoms, but for practical consideration, very large scale and long term simulations, inevitable under many scenarios such as amorphous and liquid phases, biomolecules, and phase transitions etc., are mostly employing empirical force field methods. Among these methods, ReaxFF[3] in particular is termed as first principles based, in the sense that its underlying functional forms are inspired by QM ideas and its parameters are fitted against database constructed with first principles methods. However, electronic structures are just implicitly and partly accounted for by parameterization

in terms like bond order and coordination, and the absence of explicit electron densities leads to problems (though solvable with extra effort) in phenomena like lone pairs, polarization, and charge variation. Besides, under certain circumstances such as high velocity shock and extreme conditions (high temperatures in particular), the electronic dynamics (propagation) is significantly involved and should be taken into account. The eFF method[4], originally developed in our group, provides the suitable first principles based framework to address the above issues, and the second half of this thesis (Ch. 5–Ch. 6) is then devoted to our effort to improve it. Ch. 5 describes our very early work in extending the application of eFF method to high- Z elements by developing an ECP extension for it, while more importantly, Ch. 6 presents our very recent development of the new GHA-QM+AMPERE framework that is a more rigorous and accurate successor of the eFF method.

The above-mentioned two parts on modeling of electronic structures and dynamics complete this thesis, and the variation in levels of theory involved, from hybrid XC functionals and dispersion correction of DFT to eFF and GHA-QM+AMPERE methods, endows it with a multiparadigm character. Therefore, this thesis is ultimately titled as “First principles based multiparadigm modeling of electronic structures and dynamics”.

References

- [1] Hoffmann, R. (1988) *Solids and Surfaces: A Chemist’s View on Bonding in Extended Structures*. (VCH Publishers, Inc., New York).
- [2] Burdett, J. K. (1995) *Chemical Bonding in Solids*. (Oxford University Press, Inc., New York).
- [3] van Duin, A. C. T, Dasgupta, S, Lorant, F, & Goddard, W. A. (2001) ReaxFF: A reactive force field for hydrocarbons. *J. Phys. Chem. A* **105**, 9396–9409.
- [4] Su, J. T. (2007) Ph.D. thesis (California Institute of Technology).

Chapter 2

Accurate description of electronic structures for semiconductors from DFT

The contents presented in this chapter are based on [H. Xiao](#), J. Tahir-Kheli and W. A. Goddard, III, “Accurate Band Gaps for Semiconductors from Density Functional Theory”, *J. Phys. Chem. Lett.* **2011**, *2*, 212-217.

An essential issue in developing semiconductor devices for photovoltaics is to design materials with desirable characters of electronic structures, ranging from such simple properties as appropriate band gaps and proper positioning of band levels relative to other participating members (dopants and interfacing materials, etc.), to convoluted aspects like good-natured band curvatures and wave-functions for efficient transport of photo-excited species (excitons and charge carriers). Accurate theoretical modeling of electronic structures for semiconductors stands as a powerful tool for unveiling the correlation of relevant features and functionalities to the underlying material compositions and structures, and thus plays an indispensable role in both improving the performance of current devices and conceiving novel photovoltaic materials.

DFT[1–3] proves an extremely valuable theoretical framework as elegant compromise between computational efficiency and accuracy, and various levels of approximate XC functionals have demonstrated extensively predictive power for energetics, structures, and dynamics of systems, ranging from 0D finite molecules to 3D periodic solids. However, the XC functionals at LDA and GGA levels, traditionally and exclusively used in the solid state physics community, suffer from serious underestimation of band gaps for semiconductors and insulators, and even qualitatively wrong prediction of metallic states for some small band gap ($< \sim 1$ eV) systems, while the hybrid functionals, being the superior standard choice in the quantum chemistry community from early on, have recently gained popularity in modeling of periodic systems, largely owing to growing evidence that shows their ability to predict band gaps accurately for semiconductors.

This chapter describes our work[4] on benchmarking the performance of DFT methods on band gaps of semiconductors relevant to photovoltaic applications. The theoretical background for using the KS/GKS orbital energy gap as a prediction of fundamental band gap is outlined in Sec. 2.1. Sec. 2.2 discusses the choice of basis sets and ECP and describes the computational details for our periodic calculations. Sec. 2.3 determines the best XC functionals by comparing performance of various levels of XC functionals on CuInSe₂ and CuGaSe₂, and Sec. 2.4 benchmarks B3PW91, B3LYP, and HSE06 over a set of 27 binary and ternary semiconductors.

2.1 Fundamental band gap from KS/GKS scheme in DFT

Although orbitals and associated eigenvalues (orbital energies) in the KS/GKS scheme have been widely discussed for their interpretative power within qualitative MO theories and approximation to such physical observables as IP[5–10], strictly speaking, KS/GKS orbitals are by construct solutions to the one-electron equations for artificial non-interacting system used to approximate the exact ground state, and thus have no rigorous physical significance in general[11]. However, similar to Koopmans’ theorem[12] in HF theory, which relates the eigenvalue of HOMO $\epsilon_{\text{HOMO}}^{\text{HF}}$ as an approximation to the first IP I , i.e., $\epsilon_{\text{HOMO}}^{\text{HF}} \approx -I$, it has been proven[13, 14] that in DFT, the HOMO eigenvalue from *exact* KS theory (*exact* XC functional) is precisely the negative of IP, i.e., $\epsilon_{\text{HOMO}}^{\text{KS}} = -I$, provided that the KS effective local potential vanishes at infinity. Furthermore, it was shown recently[15, 16] that the LUMO with its eigenvalue in KS/GKS scheme carries as much information on electron addition (associated energy as EA) as the HOMO does on electron removal.

Such relations set up the theoretical background of DFT’s ability to predict an important figure, the difference between IP and EA, which defines the chemical hardness η with a prefactor of 1/2 for finite species[17], or the fundamental band gap E_g for periodic systems, as

$$E_g = I - A = [E(N-1) - E(N)] - [E(N) - E(N+1)] = \left. \frac{\partial E}{\partial N} \right|_{N+\delta} - \left. \frac{\partial E}{\partial N} \right|_{N-\delta} \quad (2.1)$$

where E and N are the total energy and number of electrons, respectively. The last step in (2.1) is valid, provided that E is a series of straight lines interpolating values at integer N ’s, and such character is shown to be possessed by the exact energy functional[13, 18], and also ostensibly by the approximate XC functionals (including the nonlocal HF exchange functional in GKS scheme) for periodic systems imposed by the translational symmetry[19]. According to the conventional density functional analysis[20, 21], (2.1) can be further evaluated as

$$E_g = \epsilon_{\text{LUMO}}^{\text{KS}} - \epsilon_{\text{HOMO}}^{\text{KS}} + \Delta_{\text{XC}} \quad (2.2)$$

where $\Delta_{\text{XC}} = v_{\text{XC}}^{(+)} - v_{\text{XC}}^{(-)} \equiv \left. \frac{\delta E_{\text{XC}}[\rho]}{\delta \rho} \right|_{N+\delta} - \left. \frac{\delta E_{\text{XC}}[\rho]}{\delta \rho} \right|_{N-\delta}$ is the functional derivative discontinuity of XC energy with respect to the density (this term is non-vanishing for the *exact* case), which apparently prevents direct prediction of E_g using the KS orbital energy gap in DFT. While a more recent perspective, analyzing E as a functional of one-electron potential v_s and N (the so-called potential functional formalism)[22, 23], elaborates (2.1) in various types of approximate XC functionals[15, 16], and for the two cases we are interested in,

Case A KS scheme where E_{XC} is an explicit and differentiable functional of ρ only (e.g., LDA and GGA)

Case C GKS scheme where E_{XC} is an explicit and differentiable functional of the first order non-interacting density matrix, and the noninteracting reference system has a nonlocal GKS potential (e.g., HF calculations)

both simplify (2.1) into, with the orbitals $\{\phi_i\}$ as the only minimizer,

$$E_g = \varepsilon_{\text{LUMO}}^{\text{KS/GKS}} - \varepsilon_{\text{HOMO}}^{\text{KS/GKS}} \quad (2.3)$$

which is still consistent with (2.2) from the conventional density functional analysis, because for Case A, the approximate XC functionals render a vanishing Δ_{XC} (in contrast to the unknown *exact* XC functional), and for Case C, the discontinuity of $\frac{\partial \rho}{\partial N}$ distributes contribution of Δ_{XC} to eigenvalues of the minimizer $\{\phi_i\}$. (2.3) justifies rigorously the use of KS/GKS orbital energy gap as a direct prediction of the fundamental band gap for commonly used XC functionals (LDA, GGA, and hybrid functionals), with the accuracy dictated by the levels of approximations employed, although it must be borne in mind that (2.3) does not hold for the *exact* XC functional, if ever known.

Now the question is what level of approximation should be chosen for practical use in prediction of fundamental band gaps with sufficient accuracy for certain materials, and recent analysis of total energy for fractional charges[15, 19, 24] offers some theoretical insights: conventional DFT XC functionals such as LDA and GGA result in convex curves (lower energies) for fractional charges in-between integer numbers of electrons, in contrast to the straight lines given by the *exact* case, while the HF theory renders concave curves (higher energies); such incorrect features originate from the tendency of underlying approximations to delocalize/localize electrons, which is thus termed as delocalization/localization error; the convex/concave curves are forced into straight lines in periodic systems by the imposed translational symmetry, which follow the initial slopes of the original curves, leading to underestimated/overestimated fundamental band gaps. This analysis constitutes the theoretical foundation for the superiority of hybrid functionals, which include both GGA and HF components, and thus the delocalization and localization errors cancel out, to a certain extent, but the mixed percentage of HF exchange is in principle dependent on the system under study.

Indeed, it has been demonstrated by benchmark calculations on quite a range of materials[4, 25–29] that including some exact HF exchange in the global and screened hybrid functional schemes leads to dramatically improved prediction of band gaps, and among these efforts our work[4] was originally motivated by the study of properties of the CIGS class of solar cells, pioneered by the National Renewable Energy Laboratory (NREL), with efficiencies as high as 20.3%[30]. The heterojunction in these devices is between *n*-type CdSe and a *p*-type alloy of CuGaSe₂ and CuInSe₂ (with atomic ratios, Cu/(In+Ga) = 0.80-0.92 and Ga/(In+Ga) = 0.30-0.35). The important issues here are the magnitude of the direct band gap and the offsets in the band states at the interfaces as a function of composition. We were disappointed to find that the PBE and PW91 of GGA level lead to a band gap for CuInSe₂ of $E_g = 0.01$ eV (LDA leads to zero band gap) compared to the experimental value of $E_g = 1.04$ eV. Moreover, the popular B3LYP hybrid functional (which obtains the correct band gap of 2.0 eV for La₂CuO₄[27]) leads to $E_g = 0.95$ eV, which is too small by 9%. This led us to explore the performance of other DFT methods, and further show that the historically first hybrid density functional, B3PW91, leads to substantially better prediction of band gaps for the binary and ternary semiconductor compounds that are of interest in photovoltaics.

2.2 Choice of basis sets and ECPs for periodic calculations

Conceptually, plane wave basis sets are the best choice for periodic calculations, in a few respects: orthogonality (free of linear dependency), completeness (straightforward to improve the quality), no dependence of nuclear positions (no associated Pulay forces[31]), and infinite periodicity (PBC in nature and no BSSE), among others. In practice, however, plane wave basis sets demand extra efforts: one is the necessity of pseudopotentials for the atomic core region (even for light elements like H), due to the formidable number of plane waves required to sufficiently approximate the sharp electron density in the vicinity of nuclei; another is the complexity for evaluating HF exchange due to its nonlocal nature, and the computation is 10^2 - 10^3 times slower than with the localized atom-centered Gaussian type basis sets, making the modeling of even medium-sized systems ($\sim 10^2$ atoms) extremely expensive. Therefore, for hunting the best among XC functionals, including hybrid ones, for practical use (see Ref. [32] and Ch. 3), all calculations were performed using the CRYSTAL package[33], which employs atomic Gaussian type basis sets for periodic systems.

For heavy elements, angular-momentum-projected nonlocal ECPs[34–37] were used to replace the core electrons, for both reducing the computational cost and, more importantly, incorporating implicitly scalar relativistic effects. SOC was not explicitly treated, which can be important in determining band gaps for certain heavy systems[38, 39], and thus here band gaps are averaged over the spin-orbit levels through ECPs. The specific choice of ECPs and basis sets are summarized below:

- for Cu, Ag, Zn, Cd, Ga, and In we used the shape-consistent[40, 41] fully relativistic SBKJC small core ECPs with double zeta basis sets[42]
- for As and Sb we used the energy-consistent[43] fully relativistic Stuttgart small core ECPs[44] with cc-pVDZ basis sets[45]
- for Se and Te we used the SBKJC large core ECPs with double zeta basis sets[42] augmented by one d polarization function[46]
- for Al, P, and S we used the all-electron 6-31G(*d*) basis sets[47]

The difference between small and large core ECPs is whether electrons in the second outmost main shell are explicitly treated, e.g., for Ga, 21 electrons ($3s^23p^63d^{10}4s^24p^1$) are explicitly included in the calculations, with the small core ECP representing the Ne($1s^22s^22p^6$) core, while Se is described with only 6 electrons ($4s^24p^4$), with the large core ECP representing the $1s^22s^22p^63s^23p^63d^{10}$ core. All basis sets were modified slightly by setting any exponents more diffuse than 0.10 to this value (see Appendix for detailed modification in basis sets). This pruning procedure is necessary in order to minimize linear dependency and improve numerical instability for crystalline calculations using molecular basis sets[29]. Ideally, exponents and coefficients in these molecular basis sets should be re-optimized in crystalline calculations. Table 2.1 lists the comparison of performance with pruned basis sets as described above, to with basis sets optimized for crystalline calculations (see Ch. 3 Appendix and Ref. [32]), and both structures, including lattice parameters and internal degree of freedom $u(\text{Se})$, and band gaps improve only marginally. The main advantage for using crystal-optimized basis sets is to speed up the calculations, due to more contracted exponents, and this becomes more appreciable for larger systems, while the pruned basis sets provide a quick and reliable choice for extensive benchmark purpose.

Table 2.1. Comparison of the performance of pruned and optimized basis sets on structures and band gaps of CuInSe_2 , CuGaSe_2 , and CdS .

basis sets	CuInSe_2				CuGaSe_2				CdS	
	$a/\text{\AA}$	$c/\text{\AA}$	$u(\text{Se})$	E_g/eV	$a/\text{\AA}$	$c/\text{\AA}$	$u(\text{Se})$	E_g/eV	$a/\text{\AA}$	E_g/eV
pruned	5.909	11.899	0.229	1.07	5.729	11.234	0.255	1.58	5.933	2.55
optimized	5.879	11.809	0.226	1.04	5.693	11.192	0.252	1.54	5.930	2.56
<i>Exptl.</i>	5.781	11.642	0.226	1.04 ^a	5.614	11.022	0.259	1.67 ^b	5.811	2.58 ^c

^a Ref. [48]. ^b Ref. [49]. ^c Ref. [50].

For optimizing bulk structures, the reciprocal space was sampled by Γ -centered Monkhorst-Pack scheme[51], with an $8 \times 8 \times 8$ grid. To compute the band structure and DOS a finer $16 \times 16 \times 16$ grid was used on the optimized structure.

2.3 Key ingredients in XC functionals for performance

In order to determine whether any of the common methods for DFT could provide sufficient accuracy, we considered a series of XC functionals for band calculations on the CuInSe₂ and CuGaSe₂ chalcopyrite crystals. This included, at various levels of approximations climbing “Jacob’s ladder” [52]:

- LDA: SVWN[53, 54]
- GGA: BLYP[55, 56], PW91[57], PBE[58]
- meta-GGA: M06-L[59]
- global hybrid GGA: B3PW91[60], B3LYP[61], PBE0[62], BHLYP[63], and screened hybrid GGA: HSE06[64–66]
- global hybrid meta-GGA: M06[67]

Tables 2.2 and 2.3 show that the original hybrid scheme of Becke, B3PW91[60], leads to the lowest errors in the band gaps, with values that are 0.03 eV larger for CuInSe₂ and 0.09 eV smaller for CuGaSe₂. The B3PW91 calculated band structures and DOS are shown in Fig. 2.1 and 2.2, predicting correctly the direct band gap type for both CuInSe₂ and CuGaSe₂. In contrast, LDA(SVWN) leads to a zero band gap for CuInSe₂, while the GGA methods (PW91, PBE, and BLYP) lead to a gap of only 0.01 eV (99 to 100% error!), though the non-hybrid meta-GGA (M06-L) improves slightly with a value of 0.13 eV. Both the global hybrid B3LYP and screened hybrid HSE06 lead to too low a gap by 0.09 and 0.10 eV for CuInSe₂ and 0.27 and 0.20 eV for CuGaSe₂, while PBE0 leads to gaps that are too large (by 0.42 eV for CuInSe₂ and 0.35 eV for CuGaSe₂).

From Tables 2.2 and 2.3 we see that:

- (1) The calculated band gaps increase with the percentage of HF exchange, as pointed out by Yang *et al*[19]. Including exact exchange brings in increased localization of the electronic states, which neutralizes the delocalization error of accompanying conventional XC functionals, and is clearly the key ingredient in obtaining accurate band gaps. The higher tier of “Jacob’s ladder”, meta-GGA, indeed improves over GGA on band gaps, yet slightly, and the derived hybrid meta-GGA, M06, does not perform better than hybrid GGAs, most likely because the percentage of HF exchange is not optimal here.
- (2) B3PW91 is better than the most popular hybrid functional B3LYP for both lattice parameters and band gaps. Kresse *et al.* observed this also on metals[69]. The explanation may be that B3LYP underestimates the correlation energy of the uniform electron gas by about 30%, while B3PW91 was designed to be exact for this limit. This suggests that the periodic valence-electron density in a bulk solid is similar to a uniform electron gas.

Table 2.2. Predicted band gap and lattice parameters for CuInSe₂ chalcopyrite crystal from various levels of XC functionals. Here $\eta = c/2a$ is the tetragonal distortion, and $u(\text{Se})$ is the internal degree of freedom. HF% is the percentage of mixed HF exchange. ΔE_g and $\Delta V\%$ are the absolute and relative errors in band gap and volume, respectively, compared to experiment.

XC	HF%	E_g/eV	$\Delta E_g/\text{eV}$	$a/\text{\AA}$	$c/\text{\AA}$	$\eta = c/2a$	$u(\text{Se})$	$\Delta V\%$
<i>Exptl.</i>	–	1.04 ^a	–	5.781	11.642	1.007	0.226	–
SVWN	0%	0.00	1.04	5.787	11.676	1.009	0.216	0.50%
BLYP	0%	0.01	1.03	6.057	12.196	1.007	0.224	15.00%
PW91	0%	0.01	1.03	5.929	11.953	1.008	0.221	8.00%
PW91 ^b	0%	0.04	1.00	5.836	11.657	0.999	0.221	2.04%
PBE	0%	0.01	1.03	5.935	11.965	1.008	0.222	8.32%
M06-L	0%	0.13	0.91	5.941	12.029	1.012	0.226	9.12%
B3PW91	20%	1.07	0.03	5.911	11.895	1.006	0.229	6.82%
B3LYP	20%	0.95	0.09	5.998	12.046	1.004	0.232	11.38%
PBE0	25%	1.46	0.42	5.892	11.857	1.006	0.230	5.80%
BHLYP	50%	3.37	2.33	5.982	11.945	0.998	0.240	9.86%
HSE06	25%*	0.94	0.10	5.895	11.878	1.007	0.229	6.10%
M06	27%	1.39	0.35	5.887	11.909	1.011	0.226	6.08%

^a Ref. [48]. ^b results from Ref. [68], using plane wave basis sets with USPP.
* screened HF exchange.

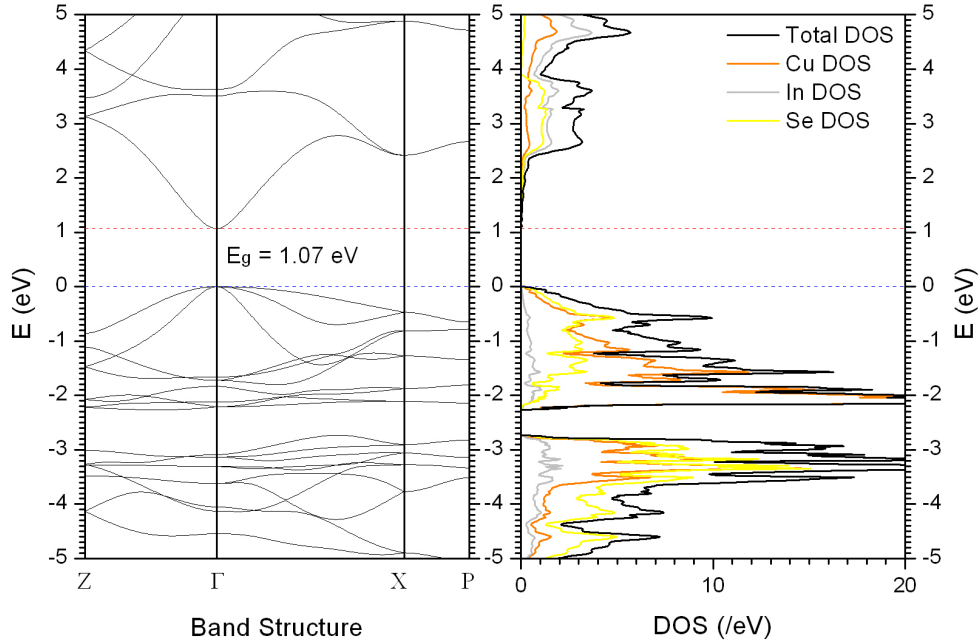


Figure 2.1. The band structure and DOS of CuInSe₂ calculated with B3PW91.

Table 2.3. Predicted band gap and lattice parameters for CuGaSe₂ chalcopyrite crystal from various levels of XC functionals. Here $\eta = c/2a$ is the tetragonal distortion, and $u(\text{Se})$ is the internal degree of freedom. HF% is the percentage of mixed HF exchange. ΔE_g and $\Delta V\%$ are the absolute and relative errors in band gap and volume, respectively, compared to experiment.

XC	HF%	E_g/eV	$\Delta E_g/\text{eV}$	$a/\text{\AA}$	$c/\text{\AA}$	$\eta = c/2a$	$u(\text{Se})$	$\Delta V\%$
<i>Exptl.</i>	–	1.67 ^a	–	5.614	11.022	0.982	0.259	–
SVWN	0%	0.24	1.43	5.589	11.135	0.996	0.243	0.13%
BLYP	0%	0.02	1.65	5.852	11.589	0.990	0.250	14.25%
PW91	0%	0.10	1.57	5.729	11.358	0.991	0.248	7.31%
PW91 ^b	0%	0.14	1.53	5.609	11.147	0.994	0.244	0.95%
PBE	0%	0.10	1.57	5.735	11.366	0.991	0.248	7.61%
M06-L	0%	0.62	1.05	5.769	11.277	0.977	0.254	8.04%
B3PW91	20%	1.58	0.09	5.729	11.234	0.981	0.255	6.14%
B3LYP	20%	1.40	0.27	5.812	11.371	0.978	0.257	10.57%
PBE0	25%	2.02	0.35	5.714	11.184	0.979	0.255	5.12%
BHLYP	50%	3.96	2.29	5.810	11.206	0.964	0.265	8.89%
HSE06	25%*	1.47	0.20	5.718	11.192	0.979	0.255	5.33%
M06	27%	1.91	0.24	5.728	11.204	0.978	0.255	5.81%

^a Ref. [49]. ^b results from Ref. [68], using plane wave basis sets with USPP.

* screened HF exchange.

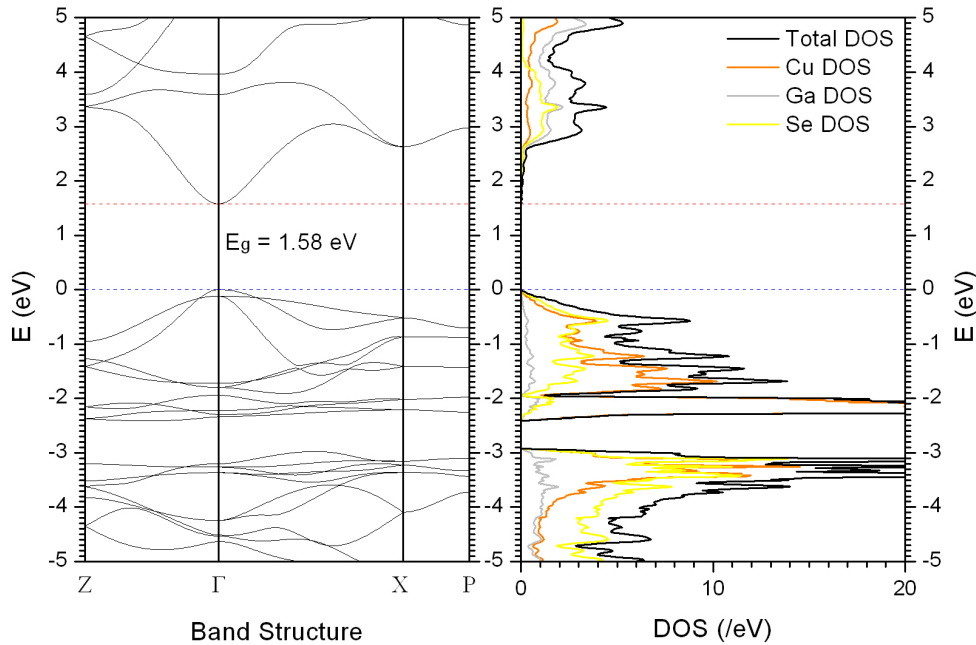


Figure 2.2. The band structure and DOS of CuGaSe₂ calculated with B3PW91.

- (3) The correlation plays a role in predicting structures. LYP renders the worst results, and PW91 is the best among GGA correlation.
- (4) Our PW91 results are comparable to those using plane wave basis sets with USPP, validating the accuracy of the Gaussian basis sets used here.

2.4 Benchmark on a set of 27 binary and ternary semiconductors

To further evaluate the accuracy of B3PW91 for band gaps of semiconductors, we considered a test set of 27 semiconductors comprising ternary compounds with chalcopyrite structure (currently of great interest for photovoltaic applications) and binary semiconductors with the zinc-blende structure (such as CdS) that are also important solar cell materials. Note our test set considers only direct band gap semiconductors. The results are shown in Table 2.4. We see that B3PW91 yields a $\text{MAD} = 0.09$ eV for band gaps. Moreover, Tables 2.5 and 2.6 show that B3PW91 leads to accurate lattice parameters, with $\text{MRD} = 2.2\%$. Generally, B3PW91 is better than B3LYP, which gives $\text{MAD} = 0.19$ eV for band gaps, and $\text{MRD} = 3.4\%$ for lattice parameters (Tables 2.7, 2.8, and 2.9).

Prior calculations[25–29] have shown that the incorporation of (global or screened) HF exchange can improve the accuracy of DFT band gaps, and the most prominent success is from the screened hybrid functional family of Heyd-Scuseria-Ernzerhof (HSE)[64–66] that is derived from the global hybrid functional PBE0 (which includes 25% HF exchange). To validate HSE, Scuseria *et al.*[29] proposed the SC/40 test set of unary and binary compounds. They showed that the older HSE03 functional gives $\text{MAD} = 0.26$ eV over the SC/40 set. They rationalized this increased accuracy by comparison with results from TDDFT calculations[70]. Among the SC/40 set are 9 binary semiconductors that are also in our test set. Comparing HSE03 (Table 2.10) and B3PW91 (Table 2.4) for this common set, we find that B3PW91 leads to $\text{MAD} = 0.08$ eV, which is significantly better than $\text{MAD} = 0.27$ eV from HSE03. Furthermore, we performed the benchmark calculations over our 27-semiconductor set with the newer HSE06, which leads to $\text{MAD} = 0.18$ eV (Table 2.10), twice that of B3PW91, although the lattice parameters are slightly better with $\text{MRD} = 2.0\%$ (Tables 2.11 and 2.12). It appears that the HSE screening of long-range HF exchange reduces the 25% HF in PBE0 to something approaching the hybrid level of 20% HF in B3PW91, which probably provides a better mixing ratio for semiconductors of $\sim 1\text{--}4$ eV band gaps. A complication with HSE is that the screening parameter is generally system dependent[70]. Thus in HSE, additional effort must be made to hunt for the optimum choice for each specific system. With B3PW91, no such system dependent parameters are used.

Table 2.4. Predicted band gaps (eV) for 27 semiconductors with B3PW91 (MAD = 0.09 eV).

Species	<i>Exptl.</i>	B3PW91	Species	<i>Exptl.</i>	B3PW91	Species	<i>Exptl.</i>	B3PW91
InP	1.42 ^a	1.68	CuAlS ₂	3.46 ^b	3.47	AgAlSe ₂	2.55 ^c	2.60
InAs	0.41 ^a	0.41	CuGaS ₂	2.50 ^d	2.47	AgGaSe ₂	1.82 ^b	1.65
InSb	0.23 ^a	0.30	CuInS ₂	1.55 ^b	1.60	AgInSe ₂	1.24 ^e	1.24
ZnS	3.84 ^a	3.75	CuAlSe ₂	2.65 ^f	2.55	CuAlTe ₂	2.06 ^g	2.25
ZnSe	2.83 ^a	2.73	CuGaSe ₂	1.67 ^f	1.58	CuGaTe ₂	1.25 ^g	1.34
ZnTe	2.39 ^a	2.28	CuInSe ₂	1.04 ^e	1.07	CuInTe ₂	1.00 ^h	1.14
CdS	2.58 ^a	2.55	AgAlS ₂	3.60 ⁱ	3.50	AgAlTe ₂	2.35 ^j	2.12
CdSe	1.85 ^a	1.84	AgGaS ₂	2.70 ^k	2.60	AgGaTe ₂	1.36 ^j	1.21
CdTe	1.61 ^a	1.67	AgInS ₂	1.87 ^b	1.87	AgInTe ₂	1.04 ^j	1.09

^a Ref. [50]. ^b Ref. [71]. ^c Ref. [72]. ^d Ref. [73]. ^e Ref. [48]. ^f Ref. [49]. ^g Ref. [74].
^h Ref. [75]. ⁱ Ref. [76]. ^j Ref. [77]. ^k Ref. [78].

Table 2.5. Predicted lattice parameters ($a/\text{\AA}$) for 9 binary semiconductors with B3PW91 (MRD = 1.9%).

Species	<i>Exptl.</i>	B3PW91	Species	<i>Exptl.</i>	B3PW91	Species	<i>Exptl.</i>	B3PW91
InP	5.869	5.944	ZnS	5.345	5.458	CdS	5.811	5.933
InAs	6.058	6.159	ZnSe	5.669	5.754	CdSe	6.077	6.217
InSb	6.479	6.584	ZnTe	6.103	6.212	CdTe	6.483	6.643

Table 2.6. Predicted lattice parameters for 18 ternary semiconductors with B3PW91 (MRD = 2.2%). X = S, Se, Te in $u(X)$.

Species	<i>Exptl.</i>				B3PW91				
	$a/\text{\AA}$	$c/\text{\AA}$	$\eta = c/2a$	$u(X)$	$a/\text{\AA}$	$c/\text{\AA}$	$\eta = c/2a$	$u(X)$	$\Delta V\%$
CuAlS ₂	5.334	10.444	0.979	0.268	5.388	10.545	0.979	0.264	3.02%
CuGaS ₂	5.347	10.474	0.979	0.254	5.412	10.602	0.979	0.258	3.70%
CuInS ₂	5.523	11.133	1.008	0.229	5.600	11.304	1.009	0.230	4.39%
CuAlSe ₂	5.606	10.901	0.972	0.257	5.711	11.162	0.977	0.260	6.27%
CuGaSe ₂	5.614	11.022	0.982	0.259	5.729	11.234	0.981	0.255	6.14%
CuInSe ₂	5.781	11.642	1.007	0.226	5.909	11.899	1.007	0.229	6.78%
AgAlS ₂	5.695	10.260	0.901	0.300	5.819	10.400	0.894	0.299	5.83%
AgGaS ₂	5.757	10.304	0.895	0.291	5.839	10.511	0.900	0.294	4.94%
AgInS ₂	5.876	11.201	0.953	0.264	5.983	11.452	0.957	0.267	6.00%
AgAlSe ₂	5.956	10.750	0.902	0.270	6.105	11.059	0.906	0.291	8.09%
AgGaSe ₂	5.992	10.883	0.908	0.288	6.121	11.141	0.910	0.286	6.83%
AgInSe ₂	6.104	11.712	0.959	0.258	6.263	12.036	0.961	0.262	8.19%
CuAlTe ₂	5.976	11.804	0.988	0.250	6.158	12.172	0.988	0.247	9.49%
CuGaTe ₂	6.023	11.940	0.991	0.256	6.150	12.197	0.992	0.245	6.51%
CuInTe ₂	6.194	12.416	1.002	0.222	6.340	12.714	1.003	0.223	7.28%
AgAlTe ₂	6.296	11.830	0.939	0.260	6.475	12.257	0.947	0.273	9.58%
AgGaTe ₂	6.288	11.940	0.949	0.260	6.469	12.284	0.950	0.271	8.89%
AgInTe ₂	6.467	12.633	0.977	0.262	6.623	12.988	0.981	0.250	7.83%

Table 2.7. Predicted band gaps (eV) for 27 semiconductors with B3LYP (MAD = 0.19 eV).

Species	<i>Exptl.</i>	B3LYP	Species	<i>Exptl.</i>	B3LYP	Species	<i>Exptl.</i>	B3LYP
InP	1.42 ^a	1.32	CuAlS ₂	3.46 ^b	3.37	AgAlSe ₂	2.55 ^c	2.52
InAs	0.41 ^a	0.00	CuGaS ₂	2.50 ^d	2.26	AgGaSe ₂	1.82 ^b	1.50
InSb	0.23 ^a	0.00	CuInS ₂	1.55 ^b	1.47	AgInSe ₂	1.24 ^e	1.15
ZnS	3.84 ^a	3.53	CuAlSe ₂	2.65 ^f	2.47	CuAlTe ₂	2.06 ^g	2.09
ZnSe	2.83 ^a	2.52	CuGaSe ₂	1.67 ^f	1.40	CuGaTe ₂	1.25 ^g	1.12
ZnTe	2.39 ^a	2.01	CuInSe ₂	1.04 ^e	0.95	CuInTe ₂	1.00 ^h	0.99
CdS	2.58 ^a	2.36	AgAlS ₂	3.60 ⁱ	3.40	AgAlTe ₂	2.35 ^j	1.98
CdSe	1.85 ^a	1.68	AgGaS ₂	2.70 ^k	2.43	AgGaTe ₂	1.36 ^j	1.02
CdTe	1.61 ^a	1.47	AgInS ₂	1.87 ^b	1.76	AgInTe ₂	1.04 ^j	0.94

^a Ref. [50]. ^b Ref. [71]. ^c Ref. [72]. ^d Ref. [73]. ^e Ref. [48]. ^f Ref. [49]. ^g Ref. [74].
^h Ref. [75]. ⁱ Ref. [76]. ^j Ref. [77]. ^k Ref. [78].

Table 2.8. Predicted lattice parameters ($a/\text{\AA}$) for 9 binary semiconductors with B3LYP (MRD = 3.1%).

Species	<i>Exptl.</i>	B3LYP	Species	<i>Exptl.</i>	B3LYP	Species	<i>Exptl.</i>	B3LYP
InP	5.869	6.015	ZnS	5.345	5.520	CdS	5.811	6.004
InAs	6.058	6.245	ZnSe	5.669	5.820	CdSe	6.077	6.289
InSb	6.479	6.681	ZnTe	6.103	6.290	CdTe	6.483	6.726

Table 2.9. Predicted lattice parameters for 18 ternary semiconductors with B3LYP (MRD = 3.6%). X = S, Se, Te in $u(X)$.

Species	<i>Exptl.</i>				B3LYP				
	$a/\text{\AA}$	$c/\text{\AA}$	$\eta = c/2a$	$u(X)$	$a/\text{\AA}$	$c/\text{\AA}$	$\eta = c/2a$	$u(X)$	$\Delta V\%$
CuAlS ₂	5.334	10.444	0.979	0.268	5.462	10.628	0.973	0.268	6.74%
CuGaS ₂	5.347	10.474	0.979	0.254	5.494	10.731	0.977	0.260	8.13%
CuInS ₂	5.523	11.133	1.008	0.229	5.686	11.453	1.007	0.234	9.03%
CuAlSe ₂	5.606	10.901	0.972	0.257	5.785	11.258	0.973	0.264	9.99%
CuGaSe ₂	5.614	11.022	0.982	0.259	5.812	11.371	0.978	0.257	10.56%
CuInSe ₂	5.781	11.642	1.007	0.226	5.998	12.046	1.004	0.232	11.40%
AgAlS ₂	5.695	10.260	0.901	0.300	5.893	10.499	0.891	0.304	9.58%
AgGaS ₂	5.757	10.304	0.895	0.291	5.922	10.648	0.899	0.296	9.35%
AgInS ₂	5.876	11.201	0.953	0.264	6.077	11.590	0.954	0.270	10.67%
AgAlSe ₂	5.956	10.750	0.902	0.270	6.182	11.166	0.903	0.295	11.90%
AgGaSe ₂	5.992	10.883	0.908	0.288	6.206	11.299	0.910	0.288	11.36%
AgInSe ₂	6.104	11.712	0.959	0.258	6.357	12.181	0.958	0.264	12.81%
CuAlTe ₂	5.976	11.804	0.988	0.250	6.239	12.299	0.986	0.251	13.57%
CuGaTe ₂	6.023	11.940	0.991	0.256	6.241	12.359	0.990	0.247	11.13%
CuInTe ₂	6.194	12.416	1.002	0.222	6.433	12.897	1.002	0.226	12.02%
AgAlTe ₂	6.296	11.830	0.939	0.260	6.568	12.367	0.942	0.277	13.75%
AgGaTe ₂	6.288	11.940	0.949	0.260	6.570	12.442	0.947	0.274	13.75%
AgInTe ₂	6.467	12.633	0.977	0.262	6.726	13.155	0.978	0.253	12.64%

Table 2.10. Predicted band gaps (eV) for 27 semiconductors with HSE06 (MAD = 0.18 eV). Previous results using HSE03[29] are also shown where available which leads to MAD = 0.27 eV.

Species	<i>Exptl.</i>	HSE06	HSE03*	Species	<i>Exptl.</i>	HSE06	Species	<i>Exptl.</i>	HSE06
InP	1.42 ^a	1.59	1.64	CuAlS ₂	3.46 ^b	3.29	AgAlSe ₂	2.55 ^c	2.41
InAs	0.41 ^a	0.41	0.39	CuGaS ₂	2.50 ^d	2.32	AgGaSe ₂	1.82 ^b	1.50
InSb	0.23 ^a	0.34	0.29	CuInS ₂	1.55 ^b	1.45	AgInSe ₂	1.24 ^e	1.08
ZnS	3.84 ^a	3.55	3.42	CuAlSe ₂	2.65 ^f	2.38	CuAlTe ₂	2.06 ^g	2.07
ZnSe	2.83 ^a	2.56	2.32	CuGaSe ₂	1.67 ^f	1.47	CuGaTe ₂	1.25 ^g	1.23
ZnTe	2.39 ^a	2.12	2.19	CuInSe ₂	1.04 ^e	0.94	CuInTe ₂	1.00 ^h	1.01
CdS	2.58 ^a	2.32	2.14	AgAlS ₂	3.60 ⁱ	3.31	AgAlTe ₂	2.35 ^j	1.93
CdSe	1.85 ^a	1.66	1.39	AgGaS ₂	2.70 ^k	2.42	AgGaTe ₂	1.36 ^j	1.08
CdTe	1.61 ^a	1.51	1.52	AgInS ₂	1.87 ^b	1.68	AgInTe ₂	1.04 ^j	0.94

* results from Ref. [29]. ^a Ref. [50]. ^b Ref. [71]. ^c Ref. [72]. ^d Ref. [73]. ^e Ref. [48].
^f Ref. [49]. ^g Ref. [74]. ^h Ref. [75]. ⁱ Ref. [76]. ^j Ref. [77]. ^k Ref. [78].

Table 2.11. Predicted lattice parameters ($a/\text{\AA}$) for 9 binary semiconductors with HSE06 (MRD = 1.6%). Previous results using HSE03[29] lead to MRD = 1.1%.

Species	<i>Exptl.</i>	HSE06	HSE03*	Species	<i>Exptl.</i>	HSE06	HSE03*	Species	<i>Exptl.</i>	HSE06	HSE03*
InP	5.869	5.928	5.909	ZnS	5.345	5.446	5.432	CdS	5.811	5.919	5.896
InAs	6.058	6.141	6.120	ZnSe	5.669	5.745	5.707	CdSe	6.077	6.204	6.152
InSb	6.479	6.566	6.535	ZnTe	6.103	6.205	6.150	CdTe	6.483	6.630	6.568

* results from Ref. [29].

Table 2.12. Predicted lattice parameters for 18 ternary semiconductors with HSE06 (MRD = 2.0%). X = S, Se, Te in $u(X)$.

Species	<i>Exptl.</i>				HSE06				
	$a/\text{\AA}$	$c/\text{\AA}$	$\eta = c/2a$	$u(X)$	$a/\text{\AA}$	$c/\text{\AA}$	$\eta = c/2a$	$u(X)$	$\Delta V\%$
CuAlS ₂	5.334	10.444	0.979	0.268	5.377	10.516	0.978	0.264	2.32%
CuGaS ₂	5.347	10.474	0.979	0.254	5.403	10.582	0.979	0.258	3.14%
CuInS ₂	5.523	11.133	1.008	0.229	5.585	11.292	1.011	0.231	3.70%
CuAlSe ₂	5.606	10.901	0.972	0.257	5.702	11.125	0.976	0.260	5.58%
CuGaSe ₂	5.614	11.022	0.982	0.259	5.717	11.197	0.979	0.255	5.35%
CuInSe ₂	5.781	11.642	1.007	0.226	5.896	11.878	1.007	0.230	6.11%
AgAlS ₂	5.695	10.260	0.901	0.300	5.798	10.362	0.893	0.299	4.70%
AgGaS ₂	5.757	10.304	0.895	0.291	5.821	10.457	0.898	0.293	3.77%
AgInS ₂	5.876	11.201	0.953	0.264	5.959	11.424	0.959	0.267	4.88%
AgAlSe ₂	5.956	10.750	0.902	0.270	6.098	10.981	0.900	0.291	7.08%
AgGaSe ₂	5.992	10.883	0.908	0.288	6.112	11.085	0.907	0.286	5.97%
AgInSe ₂	6.104	11.712	0.959	0.258	6.246	12.003	0.961	0.262	7.31%
CuAlTe ₂	5.976	11.804	0.988	0.250	6.149	12.139	0.987	0.248	8.86%
CuGaTe ₂	6.023	11.940	0.991	0.256	6.140	12.169	0.991	0.245	5.91%
CuInTe ₂	6.194	12.416	1.002	0.222	6.325	12.698	1.004	0.223	6.63%
AgAlTe ₂	6.296	11.830	0.939	0.260	6.466	12.182	0.942	0.274	8.59%
AgGaTe ₂	6.288	11.940	0.949	0.260	6.457	12.239	0.948	0.271	8.08%
AgInTe ₂	6.467	12.633	0.977	0.262	6.609	12.950	0.980	0.250	7.06%

2.5 Concluding remarks

In summary, we show that the B3PW91 hybrid functional provides accurate band gap predictions for semiconductors of $\sim 1\text{--}4$ eV band gaps (MAD = 0.09 eV) while also leading to accurate lattice parameters. Thus we recommend B3PW91 combined with standard molecular Gaussian type basis sets as a practical choice for investigating electronic structures in semiconductor devices. This should provide the basis for more accurate predictions of band offsets at semiconductor interfaces and more accurate positioning of impurity levels in the band gaps for the design of photovoltaic, thermoelectric, and other new semiconductor systems.

Appendix

This appendix lists, with the CRYSTAL14 input format, all ECP and pruned basis sets (see discussions in Sec. 2.2) used for periodic calculations in this chapter.

```

A1
13 5
0 0 6 2.0 1.0
  13983.1000000      0.00194267
  2098.7500000      0.0148599
  477.7050000       0.0728494
  134.3600000       0.2468300
  42.8709000        0.4872580
  14.5189000        0.3234960
0 1 6 8.0 1.0
  239.6680000      -0.00292619      0.00460285
  57.4419000       -0.0374080       0.0331990
  18.2859000       -0.1144870       0.1362820
  6.5991400        0.1156350       0.3304760
  2.4904900        0.6125950       0.4491460
  0.9445400        0.3937990       0.2657040
0 1 3 3.0 1.0
  1.2779000        -0.2276060      -0.0175130
  0.3975900        0.00144583      0.2445330
  0.1600950        1.0927900       0.8049340
0 1 1 0.0 1.0
  0.1000000        1.0000000       1.0000000
0 3 1 0.0 1.0
  0.3250000        1.0000000
P
15 5
0 0 6 2.0 1.0
  19413.3000000     0.0018516
  2909.4200000     0.0142062
  661.3640000      0.0699995
  185.7590000      0.2400790
  59.1943000       0.4847620
  20.0310000       0.3352000
0 1 6 8.0 1.0
  339.4780000      -0.00278217      0.00456462
  81.0101000       -0.0360499       0.03369360
  25.8780000       -0.1166310       0.13975500
  9.4522100        0.0968328        0.33936200
  3.6656600        0.6144180        0.45092100
  1.4674600        0.4037980        0.23858600
0 1 3 5.0 1.0
  2.1562300        -0.2529230      -0.01776530
  0.7489970        0.0328517       0.27405800
  0.2831450        1.0812500       0.78542100
0 1 1 0.0 1.0
  0.1000000        1.0000000       1.00000000
0 3 1 0.0 1.0
  0.5500000        1.0000000

```

S
16 5
0 0 6 2.0 1.0
21917.1000000 0.0018690
3301.4900000 0.0142300
754.1460000 0.0696960
212.7110000 0.2384870
67.9896000 0.4833070
23.0515000 0.3380740
0 1 6 8.0 1.0
423.7350000 -0.0023767 0.0040610
100.7100000 -0.0316930 0.0306810
32.1599000 -0.1133170 0.1304520
11.8079000 0.0560900 0.3272050
4.6311000 0.5922550 0.4528510
1.8702500 0.4550060 0.2560420
0 1 3 6.0 1.0
2.6158400 -0.2503740 -0.0145110
0.9221670 0.0669570 0.3102630
0.3412870 1.0545100 0.7544830
0 1 1 0.0 1.0
0.1171670 1.0000000 1.0000000
0 3 1 0.0 1.0
0.6500000 1.0000000

Cu
229 7
INPUT
19.0 1 3 2 0 0 0
23.2906000 -4.0027600 -1
2.6205900 3.3246500 -2
7.8108200 224.3233000 0
6.6332400 -180.3047000 0
51.1573400 3.4213000 -2
14.7340600 105.7012600 0
0 1 4 8.0 1.0
83.4200000 -0.0048290 -0.0082840
7.9700000 -0.6447990 -0.3218950
5.6000000 0.2652400 0.6181330
1.9320000 1.1897910 0.7221840
0 1 2 1.0 1.0
2.8660000 -0.0747740 -0.0005410
0.1319000 1.0170370 1.0000580
0 1 1 0.0 1.0
0.6874000 1.0000000 1.0000000
0 1 1 0.0 1.0
0.1000000 1.0000000 1.0000000
0 3 4 10.0 1.0
65.8000000 0.0255970
18.8200000 0.1486090
6.5380000 0.4117860
2.3480000 0.6055070
0 3 1 0.0 1.0
0.7691000 1.0000000
0 3 1 0.0 1.0
0.2065000 1.0000000

Zn
230 7
INPUT
20.0 1 3 2 0 0 0
24.8870500 -3.9164800 -1
2.7915900 3.4308200 -2
8.3267600 244.3163400 0
7.0965100 -199.4271100 0
75.7060300 4.1147300 -2
16.0762700 118.2993600 0
0 1 4 8.0 1.0
113.5000000 -0.0042800 -0.0074290
8.3080000 -0.8202320 -0.4326050
6.3320000 0.4250060 0.7234510
2.1460000 1.1980770 0.7272170
0 1 2 2.0 1.0
2.9060000 -0.0823560 -0.0230010
0.1623000 1.0215740 1.0028240
0 1 1 0.0 1.0
0.8116000 1.0000000 1.0000000

0 1 1 0.0 1.0			
0.1000000	1.0000000		1.0000000
0 3 4 10.0 1.0			
65.9900000	0.0276530		
19.8100000	0.1587940		
6.9450000	0.4209710		
2.5430000	0.5852770		
0 3 1 0.0 1.0			
0.9165000	1.0000000		
0 3 1 0.0 1.0			
0.3264000	1.0000000		
Ga			
231 7			
INPUT			
21.0 1 3 2 0 0 0			
26.7430200	-3.8736300		-1
3.4653000	4.1247200		-2
9.1113000	260.7326300		0
7.8932900	-223.9600300		0
79.9935300	4.2003300		-2
17.3911400	127.9913900		0
0 1 4 8.0 1.0			
113.9000000	-0.0017110		-0.0080460
9.1550000	-0.8230360		-0.3574320
6.6330000	0.4586180		0.6637940
2.2780000	1.1618170		0.7136190
0 1 2 3.0 1.0			
2.1230000	-0.1455060		-0.0962610
0.1939000	1.0511470		1.0175730
0 1 1 0.0 1.0			
0.8818000	1.0000000		1.0000000
0 1 1 0.0 1.0			
0.1000000	1.0000000		1.0000000
0 3 4 10.0 1.0			
70.4300000	0.0288770		
21.0500000	0.1662530		
7.4010000	0.4277760		
2.7520000	0.5704100		
0 3 1 0.0 1.0			
1.0260000	1.0000000		
0 3 1 0.0 1.0			
0.3907000	1.0000000		
As			
233 9			
INPUT			
23. 0 2 4 6 2 0			
28.725122 370.114025 0			
6.7676810	9.3492960		0
45.3310640	99.1421030		0
44.7674150	198.3078800		0
19.5390900	28.3830730		0
18.9734710	56.8714640		0
51.0571520	-18.4851450		0
50.1513400	-28.1135300		0
16.1089360	-1.2238950		0
14.6722230	-1.3457650		0
3.8519270	0.1017570		0
3.8135020	0.1703380		0
11.9405840	-0.7752300		0
17.7611600	-2.1572590		0
0 0 6 2.0 1.0			
2542.8100000	0.0011370		
381.1690000	0.0060550		
40.2342000	0.0841250		
16.1217000	-0.4052850		
3.2018900	0.7129260		
1.4209600	0.4733760		
0 0 6 2.0 1.0			
2542.8100000	-0.0003900		
381.1690000	-0.0021900		
40.2342000	-0.0268530		
16.1217000	0.1368780		
3.2018900	-0.3204570		
1.4209600	-0.3373910		
0 0 1 0.0 1.0			
0.3214430	1.0000000		

0 0 1 0.0 1.0		
0.1167350	1.0000000	
0 2 6 6.0 1.0		
99.5349000	0.0038570	
24.1195000	-0.0851010	
5.8419600	0.4047620	
2.5601000	0.5314780	
1.0930800	0.1840120	
0.3184240	0.0057640	
0 2 6 3.0 1.0		
99.5349000	-0.0007720	
24.1195000	0.0199410	
5.8419600	-0.1072100	
2.5601000	-0.1722590	
1.0930800	0.0087610	
0.3184240	0.5697440	
0 2 1 0.0 1.0		
0.1009720	1.0000000	
0 3 6 10.0 1.0		
113.5090000	0.0119800	
36.8872000	0.0795440	
13.6893000	0.2367550	
5.3896400	0.4015340	
2.0804600	0.4066860	
0.7375680	0.1731620	
0 3 1 0.0 1.0		
0.3078000	1.0000000	

Se

234 3

INPUT

6.0 1 2 2 2 0 0			
2.0935600	-5.5849800	-1	
20.5564400	13.2808100	-2	
3.1549000	51.0001100	0	
2.5849500	1.7964000	-2	
2.5852600	30.4378700	0	
1.3829000	2.4000100	-2	
1.4267100	6.5994800	0	
0 1 4 6.0 1.0			
3.711000000	0.05574400	-0.00601400	
1.586000000	-0.51052000	-0.12144700	
0.533900000	0.48075500	0.45260700	
0.208500000	0.81029200	0.66975100	
0 1 1 0.0 1.0			
0.100000000	1.00000000	1.00000000	
0 3 2 0.0 1.0			
1.709860600	0.99541800		
0.552825300	1.00000000		

Ag

247 7

INPUT

19.0 1 3 3 2 0 0			
9.0169600	-8.4466900	-1	
1.5174000	6.2063400	-2	
3.2308800	-56.8262400	0	
4.8274700	92.4017300	0	
1.2169900	3.7563700	-2	
3.1861500	-80.9533500	0	
4.0534900	118.8680100	0	
22.9402000	3.4089500	-2	
6.2662700	57.1051300	0	
0 1 4 8.0 1.0			
63.5600000	-0.0007310	-0.0042340	
6.3900000	1.3927360	0.0612760	
5.0220000	-2.8731020	-0.3387460	
1.7890000	2.0173610	1.1908320	
0 1 2 1.0 1.0			
2.4510000	-0.0725390	-0.0498300	
0.1561000	1.0213580	1.0065160	
0 1 1 0.0 1.0			
0.6871000	1.0000000	1.0000000	
0 1 1 0.0 1.0			
0.1000000	1.0000000	1.0000000	
0 3 3 10.0 1.0			
14.6400000	0.0136280		
2.6930000	0.3726950		

	1.2330000	0.6812940	
0 3 1	0.0 1.0		
	0.5057000	1.0000000	
0 3 1	0.0 1.0		
	0.1900000	1.0000000	
Cd			
248 7			
INPUT			
20.0	1 3 3 2 0 0		
	9.8132500	-8.6986400	-1
	1.6047600	6.5693400	-2
	3.3772700	-59.3639500	0
	5.0887600	93.5961000	0
	1.2517100	3.6786300	-2
	3.4259200	-104.5069400	0
	4.2141500	145.6731600	0
	22.3533700	3.3309400	-2
	6.7540800	62.0661600	0
0 1 4	8.0 1.0		
	63.3800000	-0.0004640	-0.0048740
	6.7140000	2.2928770	0.1896300
	5.6020000	-3.9028840	-0.4918720
	1.9710000	2.0846040	1.2135010
0 1 2	2.0 1.0		
	2.6960000	-0.0648660	-0.0533380
	0.1758000	1.0196610	1.0071020
0 1 1	0.0 1.0		
	0.7689000	1.0000000	1.0000000
0 1 1	0.0 1.0		
	0.1000000	1.0000000	1.0000000
0 3 3	10.0 1.0		
	15.5100000	0.0120650	
	2.9410000	0.3701680	
	1.3790000	0.6807600	
0 3 1	0.0 1.0		
	0.5782000	1.0000000	
0 3 1	0.0 1.0		
	0.2300000	1.0000000	
In			
249 7			
INPUT			
21.0	1 3 3 2 0 0		
	10.5898700	-8.8403100	-1
	1.7388300	6.9012400	-2
	3.6280600	-68.4831900	0
	5.3027000	101.7727200	0
	1.4304500	3.9855400	-2
	3.7444700	-129.7859400	0
	4.4767900	171.9048700	0
	29.1607200	3.4924400	-2
	7.2656600	68.2781600	0
0 1 4	8.0 1.0		
	71.7600000	0.0007330	-0.0045130
	7.6540000	1.0897810	0.0316150
	5.6160000	-2.7310890	-0.3380060
	2.1040000	2.1128440	1.2134640
0 1 2	3.0 1.0		
	2.6100000	-0.0996900	-0.1103170
	0.1901000	1.0312300	1.0139000
0 1 1	0.0 1.0		
	0.8410000	1.0000000	1.0000000
0 1 1	0.0 1.0		
	0.1000000	1.0000000	1.0000000
0 3 3	10.0 1.0		
	17.1600000	0.0148930	
	3.1270000	0.3881350	
	1.4750000	0.6626390	
0 3 1	0.0 1.0		
	0.6452000	1.0000000	
0 3 1	0.0 1.0		
	0.2754000	1.0000000	
Sb			
251 9			
INPUT			
23.0	0 2 4 4 2 0		

16.3308650	281.0715810	0
8.5565420	61.7166040	0
14.4703370	67.4573800	0
13.8161940	134.9335030	0
8.4249240	14.7163440	0
8.0927280	29.5185120	0
14.8863310	35.4478150	0
15.1463190	53.1434660	0
5.9082670	9.1792230	0
5.5943220	13.2402530	0
14.4449780	-15.3668010	0
14.4492950	-20.2961380	0
0 0 6 2.0 1.0		
371.5840000	0.0015910	
26.5392000	-0.0416840	
16.6213000	0.2733430	
7.7355100	-0.7676850	
1.8923400	0.8994960	
0.9104310	0.4313870	
0 0 6 2.0 1.0		
371.5840000	0.0006540	
26.5392000	-0.0109620	
16.6213000	0.0938330	
7.7355100	-0.3040090	
1.8923400	0.5084090	
0.9104310	0.3392390	
0 0 1 0.0 1.0		
0.2442310	1.0000000	
0 0 1 0.0 1.0		
0.1000000	1.0000000	
0 2 5 6.0 1.0		
16.0509000	0.0921570	
10.2621000	-0.2755590	
2.4283200	0.6586400	
1.0336000	0.4668920	
0.2594400	0.0285110	
0 2 5 3.0 1.0		
16.0509000	-0.0253130	
10.2621000	0.0797960	
2.4283200	-0.2420940	
1.0336000	-0.1486050	
0.2594400	0.5489440	
0 2 1 0.0 1.0		
0.1000000	1.0000000	
0 3 5 10.0 1.0		
45.4785000	0.0032590	
18.5114000	-0.0054970	
3.9160000	0.2799530	
1.7148200	0.5127510	
0.6973190	0.3328720	
0 3 1 0.0 1.0		
0.2304000	1.0000000	
Te		
252 3		
INPUT		
6.0 2 3 3 2 0 0		
0.9484700	-3.9598400	-1
3.9468200	-13.4287100	-1
3.4940000	12.9566500	-2
1.2147700	-47.4588200	0
1.3353000	72.7751400	0
1.3739400	8.4792100	-2
1.2776100	-39.4068400	0
1.2842500	51.9367300	0
3.6661800	11.5466300	-2
0.9318900	11.2377600	0
0 1 4 6.0 1.0		
2.364000000	0.08717900	-0.00398200
0.976900000	-0.77682600	-0.23690000
0.464700000	0.56325000	0.40146700
0.177100000	0.92605300	0.79317900
0 1 1 0.0 1.0		
0.100000000	1.00000000	1.00000000
0 3 2 0.0 1.0		
0.497790100	0.95590600	
0.200978300	1.00000000	

References

- [1] Hohenberg, P & Kohn, W. (1964) Inhomogeneous electron gas. *Phys. Rev.* **136**, B864–B871.
- [2] Kohn, W & Sham, L. J. (1965) Self-consistent equations including exchange and correlation effects. *Phys. Rev.* **140**, A1133–A1138.
- [3] Kohn, W. (1999) Nobel lecture: Electronic structure of matter-wave functions and density functionals. *Rev. Mod. Phys.* **71**, 1253–1266.
- [4] Xiao, H, Tahir-Kheli, J, & Goddard, W. A. (2011) Accurate band gaps for semiconductors from density functional theory. *J. Phys. Chem. Lett.* **2**, 212–217.
- [5] Kohn, W, Becke, A. D, & Parr, R. G. (1996) Density functional theory of electronic structure. *J. Phys. Chem.* **100**, 12974–12980.
- [6] Baerends, E. J & Gritsenko, O. V. (1997) A quantum chemical view of density functional theory. *J. Phys. Chem. A* **101**, 5383–5403.
- [7] Savin, A, Umrigar, C, & Gonze, X. (1998) Relationship of Kohn-Sham eigenvalues to excitation energies. *Chem. Phys. Lett.* **288**, 391–395.
- [8] Stowasser, R & Hoffmann, R. (1999) What do the Kohn-Sham orbitals and eigenvalues mean? *J. Am. Chem. Soc.* **121**, 3414–3420.
- [9] Baerends, E. J. (2000) Perspective on “Self-consistent equations including exchange and correlation effects”. *Theor. Chem. Acc.* **103**, 265–269.
- [10] Chong, D. P, Gritsenko, O. V, & Baerends, E. J. (2002) Interpretation of the Kohn-Sham orbital energies as approximate vertical ionization potentials. *J. Chem. Phys.* **116**, 1760–1772.
- [11] Koch, W & Holthausen, M. C. (2001) *A Chemist’s Guide to Density Functional Theory, Second Edition*. (Wiley-VCH, Weinheim).
- [12] Koopmans, T. (1934) Über die zuordnung von wellenfunktionen und eigenwerten zu den einzelnen elektronen eines atoms. *Physica* **1**, 104–113.
- [13] Perdew, J, Parr, R, Levy, M, & Balduz, J. (1982) Density-functional theory for fractional particle number: Derivative discontinuities of the energy. *Phys. Rev. Lett.* **49**, 1691–1694.
- [14] Levy, M, Perdew, J, & Sahni, V. (1984) Exact differential equation for the density and ionization energy of a many-particle system. *Phys. Rev. A* **30**, 2745–2748.
- [15] Cohen, A. J, Mori-Sánchez, P, & Yang, W. (2008) Fractional charge perspective on the band gap in density-functional theory. *Phys. Rev. B* **77**, 115123.

- [16] Yang, W, Cohen, A. J, & Mori-Sánchez, P. (2012) Derivative discontinuity, bandgap and lowest unoccupied molecular orbital in density functional theory. *J. Chem. Phys.* **136**, 204111.
- [17] Parr, R. G & Pearson, R. G. (1983) Absolute hardness: Companion parameter to absolute electronegativity. *J. Am. Chem. Soc.* **105**, 7512–7516.
- [18] Yang, W, Zhang, Y, & Ayers, P. (2000) Degenerate ground states and a fractional number of electrons in density and reduced density matrix functional theory. *Phys. Rev. Lett.* **84**, 5172–5175.
- [19] Mori-Sánchez, P, Cohen, A. J, & Yang, W. (2008) Localization and delocalization errors in density functional theory and implications for band-gap prediction. *Phys. Rev. Lett.* **100**, 146401.
- [20] Perdew, J & Levy, M. (1983) Physical content of the exact Kohn-Sham orbital energies: Band gaps and derivative discontinuities. *Phys. Rev. Lett.* **51**, 1884–1887.
- [21] Sham, L & Schlüter, M. (1983) Density-functional theory of the energy gap. *Phys. Rev. Lett.* **51**, 1888–1891.
- [22] Yang, W, Ayers, P, & Wu, Q. (2004) Potential functionals: Dual to density functionals and solution to the v -representability problem. *Phys. Rev. Lett.* **92**, 146404.
- [23] Heaton-Burgess, T, Ayers, P, & Yang, W. (2007) Spin-potential functional formalism for current-carrying noncollinear magnetic systems. *Phys. Rev. Lett.* **98**, 036403.
- [24] Cohen, A. J, Mori-Sánchez, P, & Yang, W. (2008) Insights into current limitations of density functional theory. *Science* **321**, 792–794.
- [25] Seidl, A, Görling, A, Vogl, P, Majewski, J, & Levy, M. (1996) Generalized Kohn-Sham schemes and the band-gap problem. *Phys. Rev. B* **53**, 3764–3774.
- [26] Muscat, J, Wander, A, & Harrison, N. M. (2001) On the prediction of band gaps from hybrid functional theory. *Chem. Phys. Lett.* **342**, 397–401.
- [27] Perry, J, Tahir-Kheli, J, & Goddard, W. A. (2001) Antiferromagnetic band structure of La_2CuO_4 : Becke-3-Lee-Yang-Parr calculations. *Phys. Rev. B* **63**, 144510.
- [28] Perry, J, Tahir-Kheli, J, & Goddard, W. A. (2002) Ab initio evidence for the formation of impurity $d_{3z^2-r^2}$ holes in doped $\text{La}_{2-x}\text{Sr}_x\text{CuO}_4$. *Phys. Rev. B* **65**, 144501.
- [29] Heyd, J, Peralta, J. E, Scuseria, G. E, & Martin, R. L. (2005) Energy band gaps and lattice parameters evaluated with the Heyd-Scuseria-Ernzerhof screened hybrid functional. *J. Chem. Phys.* **123**, 174101.

- [30] Jackson, P, Hariskos, D, Lotter, E, Paetel, S, Wuerz, R, Menner, R, Wischmann, W, & Powalla, M. (2011) New world record efficiency for Cu(In,Ga)Se₂ thin-film solar cells beyond 20%. *Prog. Photovoltaics* **19**, 894–897.
- [31] Pulay, P. (1969) Ab initio calculation of force constants and equilibrium geometries in polyatomic molecules. *Mol. Phys.* **17**, 197–204.
- [32] Xiao, H & Goddard, W. A. (2014) Predicted roles of defects on band offsets and energetics at CIGS (Cu(In,Ga)Se₂/CdS) solar cell interfaces and implications for improving performance. *J. Chem. Phys.* **141**, 094701.
- [33] Dovesi, R, Saunders, V. R, Roetti, C, Orlando, R, Zicovich-Wilson, C. M, Pascale, F, Civalleri, B, Doll, K, Harrison, N. M, Bush, I. J, D’Arco, P, Llunell, M, Causà, M, & Noël, Y. (2014) *CRYSTAL14 User’s Manual*. (University of Torino, Torino).
- [34] Goddard, W. A. (1968) New foundation for the use of pseudopotentials in metals. *Phys. Rev.* **174**, 659–662.
- [35] Kahn, L. R & Goddard, W. A. (1972) Ab initio effective potentials for use in molecular calculations. *J. Chem. Phys.* **56**, 2685–2701.
- [36] Melius, C. F & Goddard, W. A. (1974) Ab initio effective potentials for use in molecular quantum mechanics. *Phys. Rev. A* **10**, 1528–1540.
- [37] Kahn, L. R, Baybutt, P, & Truhlar, D. G. (1976) Ab initio effective core potentials: Reduction of all-electron molecular structure calculations to calculations involving only valence electrons. *J. Chem. Phys.* **65**, 3826–3853.
- [38] Peralta, J. E, Heyd, J, Scuseria, G. E, & Martin, R. L. (2006) Spin-orbit splittings and energy band gaps calculated with the Heyd-Scuseria-Ernzerhof screened hybrid functional. *Phys. Rev. B* **74**, 073101.
- [39] Kim, Y.-S, Hummer, K, & Kresse, G. (2009) Accurate band structures and effective masses for *inp*, *inas*, and *insb* using hybrid functionals. *Phys. Rev. B* **80**, 035203.
- [40] Durand, P & Barthelat, J.-C. (1975) A theoretical method to determine atomic pseudopotentials for electronic structure calculations of molecules and solids. *Theor. Chim. Acta* **38**, 283–302.
- [41] Christiansen, P. A, Lee, Y. S, & Pitzer, K. S. (1979) Improved ab initio effective core potentials for molecular calculations. *J. Chem. Phys.* **71**, 4445–4450.
- [42] Stevens, W. J, Krauss, M, Basch, H, & Jasien, P. G. (1992) Relativistic compact effective potentials and efficient, shared-exponent basis sets for the third-, fourth-, and fifth-row atoms. *Can. J. Chem.* **70**, 612–630.

- [43] Dolg, M, Wedig, U, Stoll, H, & Preuss, H. (1987) Energyadjusted ab initio pseudopotentials for the first row transition elements. *J. Chem. Phys.* **86**, 866–872.
- [44] Metz, B, Stoll, H, & Dolg, M. (2000) Small-core multiconfiguration-Dirac-Hartree-Fock-adjusted pseudopotentials for post-*d* main group elements: Application to PbH and PbO. *J. Chem. Phys.* **113**, 2563–2569.
- [45] Peterson, K. A. (2003) Systematically convergent basis sets with relativistic pseudopotentials. I. Correlation consistent basis sets for the post-*d* group 1315 elements. *J. Chem. Phys.* **119**, 11099–11112.
- [46] Labello, N. P, Ferreira, A. M, & Kurtz, H. A. (2005) An augmented effective core potential basis set for the calculation of molecular polarizabilities. *J. Comput. Chem.* **26**, 1464–1471.
- [47] Francl, M. M, Pietro, W. J, Hehre, W. J, Binkley, J. S, Gordon, M. S, DeFrees, D. J, & Pople, J. A. (1982) Selfconsistent molecular orbital methods. XXIII. A polarization-type basis set for second-row elements. *J. Chem. Phys.* **77**, 3654–3665.
- [48] Shay, J. L, Tell, B, Kasper, H. M, & Schiavone, L. M. (1973) Electronic structure of AgInSe₂ and CuInSe₂. *Phys. Rev. B* **7**, 4485–4490.
- [49] ShoShirakata, ShigefusaChichibu, & ShigehiroIsomura. (1997) Room-temperature photorefectance of CuAl_xGa_{1-x}Se₂ alloys. *Jpn. J. Appl. Phys.* **36**, 7160–7161.
- [50] Pässler, R. (1999) Parameter sets due to fittings of the temperature dependencies of fundamental bandgaps in semiconductors. *Phys. Stat. Sol. B* **216**, 975–1007.
- [51] Monkhorst, H. J & Pack, J. D. (1976) Special points for Brillouin-zone integrations. *Phys. Rev. B* **13**, 5188–5192.
- [52] Perdew, J. P & Schmidt, K. (2001) Jacob’s ladder of density functional approximations for the exchange-correlation energy. *AIP Conf. Proc.* **577**, 1–20.
- [53] Slater, C. J. (1974) *Quantum Theory of Molecules and Solids, Vol. 4.* (McGraw-Hill, New York).
- [54] Vosko, S. H, Wilk, L, & Nusair, M. (1980) Accurate spin-dependent electron liquid correlation energies for local spin density calculations: a critical analysis. *Can. J. Phys.* **58**, 1200–1211.
- [55] Becke, A. D. (1988) Density-functional exchange-energy approximation with correct asymptotic behavior. *Phys. Rev. A* **38**, 3098–3100.
- [56] Lee, C, Yang, W, & Parr, R. G. (1988) Development of the Colle-Salvetti correlation-energy formula into a functional of the electron density. *Phys. Rev. B* **37**, 785–789.

- [57] Perdew, J. P., Chevary, J. A., Vosko, S. H., Jackson, K. A., Pederson, M. R., Singh, D. J., & Fiolhais, C. (1992) Atoms, molecules, solids, and surfaces: Applications of the generalized gradient approximation for exchange and correlation. *Phys. Rev. B* **46**, 6671–6687. erratum. (1993) **48**, 4978.
- [58] Perdew, J. P., Burke, K., & Ernzerhof, M. (1996) Generalized gradient approximation made simple. *Phys. Rev. Lett.* **77**, 3865–3868. erratum. (1997) **78**, 1396.
- [59] Zhao, Y & Truhlar, D. G. (2006) A new local density functional for main-group thermochemistry, transition metal bonding, thermochemical kinetics, and noncovalent interactions. *J. Chem. Phys.* **125**, 194101.
- [60] Becke, A. D. (1993) Densityfunctional thermochemistry. III. The role of exact exchange. *J. Chem. Phys.* **98**, 5648–5652.
- [61] Stephens, P. J, Devlin, F. J, Chabalowski, C. F, & Frisch, M. J. (1994) Ab initio calculation of vibrational absorption and circular dichroism spectra using density functional force fields. *J. Phys. Chem.* **98**, 11623–11627.
- [62] Adamo, C & Barone, V. (1999) Toward reliable density functional methods without adjustable parameters: The PBE0 model. *J. Chem. Phys.* **110**, 6158–6170.
- [63] Becke, A. D. (1993) A new mixing of Hartree-Fock and local densityfunctional theories. *J. Chem. Phys.* **98**, 1372–1377.
- [64] Heyd, J, Scuseria, G. E, & Ernzerhof, M. (2003) Hybrid functionals based on a screened Coulomb potential. *J. Chem. Phys.* **118**, 8207–8215. erratum. (2006) **124**, 219906.
- [65] Heyd, J & Scuseria, G. E. (2004) Efficient hybrid density functional calculations in solids: Assessment of the Heyd-Scuseria-Ernzerhof screened coulomb hybrid functional. *J. Chem. Phys.* **121**, 1187–1192.
- [66] Krukau, A. V, Vydrov, O. A, Izmaylov, A. F, & Scuseria, G. E. (2006) Influence of the exchange screening parameter on the performance of screened hybrid functionals. *J. Chem. Phys.* **125**, 224106.
- [67] Zhao, Y & Truhlar, D. G. (2008) The M06 suite of density functionals for main group thermochemistry, thermochemical kinetics, noncovalent interactions, excited states, and transition elements: two new functionals and systematic testing of four M06-class functionals and 12 other functionals. *Theor. Chem. Acc.* **120**, 215–241.

- [68] Maeda, T, Takeichi, T, & Wada, T. (2006) Systematic studies on electronic structures of CuInSe_2 and the other chalcopyrite related compounds by first principles calculations. *Phys. Stat. Sol. A* **203**, 2634–2638.
- [69] Paier, J, Marsman, M, & Kresse, G. (2007) Why does the B3LYP hybrid functional fail for metals? *J. Chem. Phys.* **127**, 024103.
- [70] Brothers, E. N, Izmaylov, A. F, Normand, J. O, Barone, V, & Scuseria, G. E. (2008) Accurate solid-state band gaps via screened hybrid electronic structure calculations. *J. Chem. Phys.* **129**, 011102.
- [71] Shay, J. L, Tell, B, Kasper, H. M, & Schiavone, L. M. (1972) p - d hybridization of the valence bands of I-III-VI₂ compounds. *Phys. Rev. B* **5**, 5003–5005.
- [72] Honeyman, W. N & Wilkinson, K. H. (1971) Growth and properties of single crystals of group I-III-VI₂ ternary semiconductors. *J. Phys. D: Appl. Phys.* **4**, 1182–1185.
- [73] Horinaka, H, Yamamoto, N, & Miyautchi, T. (1978) Application of modulated phase-shift-difference method with rotating quarter-wave plate to CuGaS_2 . *Jpn. J. Appl. Phys.* **17**, 521–526.
- [74] Bodnar', I. V. (2003) CuGaTe_2 - CuAlTe_2 system. *Inorganic Materials* **39**, 10–14.
- [75] Quintero, M, Gonzalez, J, & Woolley, J. C. (1991) Optical energy-gap variation and deformation potentials in CuInTe_2 . *J. Appl. Phys.* **70**, 1451–1454.
- [76] Tsuboi, N, Hashimoto, Y, Kurasawa, M, Kobayashi, S, & Kaneko, F. (1999) Preparation and properties of $\text{Ag}(\text{Al}_x\text{Ga}_{1-x})\text{S}_2$ crystals by iodine transport method. *Jpn. J. Appl. Phys.* **38**, 6445–6449.
- [77] Tell, B, Shay, J. L, & Kasper, H. M. (1974) Some properties of AgAlTe_2 , AgGaTe_2 , and AgInTe_2 . *Phys. Rev. B* **9**, 5203–5208.
- [78] Kobayashi, S, Ohno, T, Tsuboi, N, Kaneko, F, & Maruyama, T. (1989) Optical properties near the fundamental edge of an AgGaS_2 single crystal. *Jpn. J. Appl. Phys.* **28**, 189–194.

Chapter 3

Predicted roles of defects in band offsets and energetics at CIGS Solar Cell interfaces and implications for improving performance

The contents presented in this chapter are based on [H. Xiao](#) and W. A. Goddard, III, “Predicted roles of defects on band offsets and energetics at CIGS (Cu(In,Ga)Se₂/CdS) solar cell interfaces and implications for improving performance”, *J. Chem. Phys.* **2014**, *141*, 094701.

Harvesting solar energy through direct transformation into electrical power by photovoltaic devices is a most promising approach to renewable energy alternatives, and indeed the global operating capacity for solar photovoltaics is increasing steadily[1]. Currently, crystalline silicon technology dominates industrial solar cell production[2], but thin film technology for solar cells would provide flexibility in both production and implementation[3]. Among all thin film absorber materials, CIGS has reached the highest conversion efficiency, exceeding 20% on rigid substrates in laboratory-scale[4], with efficiency on flexible substrates increasing rapidly[5, 6], but that the efficiency of manufactured modules and panels lags behind considerably, raising the quest for identifying key factors in quality control of composition and structure. A significant characteristic of CIGS absorbers is the universal presence of such structural defects as Cu vacancies and Na impurities, which correlate strongly with device performance. We expect that understanding these correlations would help improve CIGS solar cell manufacturing processes to achieve high performance and might point the way toward designing novel absorber materials.

Experimentally, it is well established that Cu deficiencies near the CIGS/CdS interface is an essential characteristic of highest efficiency CIGS solar cells[7–9]. It has been suggested that this may

be because of reduced recombination[10], but others consider that is not likely the major responsible for the effect of Cu vacancies on performance[11]. Additionally, incorporation of Na[9, 10, 12] is widely accepted as a key ingredient in building the best performance devices, but the origin of this effect remains debated, with suggestions that it may affect film growth (grain sizes and crystal orientation)[13–17] and *p*-type conductivity[16, 18, 19]. None of these speculations has yet been confirmed as crucial for the boost in performance. Indeed, K has recently been proposed[6] to provide a beneficial alternative. In addition, it is generally observed that Cd dopants are introduced by diffusion into CIGS absorbers close to the interface with CdS buffer layers[20–22], resulting in the formation of a buried homojunction[23], but this is suggested to have limited influence on cell efficiency[24].

Despite numerous experimental studies, an atomistic understanding of the roles of such defects on device performance is hindered by difficulties in decoupling and probing directly the effects from various factors. Consequently, we carried out QM studies to provide an understanding of these phenomena. DFT methods of QM are widely used to investigate the relationship between chemistry and functionality of materials (see Ch. 2 and references therein), and some DFT efforts have previously been applied toward such aspects of CIGS solar cells as defect formation[19, 25–30] and levels[31–33]. The most important aspect of CIGS solar cells is the CIGS/CdS interface, where the essential physics of photovoltaics takes place. It is here that the defects mentioned above have their highest concentrations and their greatest impact. Therefore, the aim of our studies is to provide a theoretical basis for understanding of roles of defects in the CIGS/CdS interface.

This chapter describes our recent work[34], in which we first establish the accuracy of the B3PW91 flavor of DFT methodology for predicting band offsets through benchmarks studies on (110) and (112) CuInSe₂/CdS interfaces. Then we determine the effects of Cu vacancies, and doping with Ga, Na, K, and Cd on both band offsets and interfacial energies. To do this we constructed interfaces between CdS and CIGS with various defects. These results are used to recommend changes to optimize solar cell performance.

3.1 Methodology for calculating band offsets from interface modeling

It is generally understood that the LDA or GGA (PW91 or PBE) flavors of DFT lead to band gaps that are 1 to 2 eV too small (see Ch. 2 and references therein). For these methods it is popular to add in a Hubbard self-interaction correction (U) to improve the band gap[35] or to include perturbative many-body approximation (G0W0)[36]. Our approach is instead to use hybrid DFT functionals that we have shown provide accurate band gaps for semiconductors and insulators (see Ch. 2 and references therein). In particular we showed that the hybrid functional B3PW91 gives accurate band

gaps (within 0.1 eV) for the semiconductors considered in this study.

All calculations were performed with the CRYSTAL09 package[37], which uses local atomic Gaussian-type basis sets rather than plane waves. This enables fast evaluation of the HF exchange terms required for hybrid DFT method (the evaluation of exact exchange for plane wave basis sets is very expensive). We used all-electron basis sets of triple- ζ quality for Na, S, and K[38, 39], but for Cu, Ga, Se, Cd, and In we used the SBKJC Relativistic effective core potentials (based on angular momentum projection operators[40–43]) and the associated basis sets[44]. Thus we treat explicitly just the outer 19 electrons for Cu, 21 for Ga, 6 for Se, 20 for Cd, and 21 for In. We optimized the valence and polarization Gaussian exponents of all basis sets for ideal crystal structures (see Appendix for details) to reduce linear dependency. Note that we neglected SOC, because all the systems considered here are closed-shell and the lowest conduction bands are dominant by s -type atomic orbitals, there is only second-order SOC, which is small. For example, the contribution of SOC to band gaps in CdS and InP are calculated to be only 0.03 and 0.08 eV[45]. An extra-large grid, consisting of 75 radial points and 974 angular points, was used for accurate integration, and the reciprocal space was sampled by Γ -centered Monkhorst-Pack scheme[46] with a fine resolution of around $2\pi \times 1/40 \text{ \AA}^{-1}$.

We employed the AEP method[47], rather than the core level method as discussed later, to provide reference levels necessary for connecting the macroscopic band energy levels for the bulk systems and the interfaces[48]. The electrostatic potential was evaluated at each point by the range separation and multipolar expansion scheme[49, 50] implemented in CRYSTAL09, setting ITOL = 15 and IDIPO = 6 for accuracy. In order to converge the integrals of electrostatic potentials to within 0.01 eV, we adopted grids with resolution of 0.01 \AA .

Figure 3.1 illustrates the procedure of aligning band energies of our interface calculations with those of the bulk system.

- First, we constructed the interface based on the bulk structures.
- Then we optimized fully both the atomic positions and the supercell lattice parameters, while applying symmetry constraints to maintain a perfect matching at the interface (all coordinates and symmetry constraints are provided in the supplemental material of our paper[34]).
- Then we averaged the electrostatic potential within the xy plane as a function of the interface direction, z to obtain $V(z)$. Here the middle layer of each material, uniquely defined between minima of $V(z)$, was further averaged and compared to the $V(z)$ from bulk calculations to deduce the shift in the reference levels.
- Finally, the VBM and CBM in each bulk system were aligned to obtain the VBO and CBO.

Note that, for theoretical consistency, all values, including band gaps and lattice parameters of

bulks, are from calculations of the same B3PW91 level, without use of any experimental results. In constructing interface models, lattice matching of two sides is an inevitable issue, but all cases throughout this study have lattice mismatch within 0.7%, which we found to give at most 0.06 eV error in relative electronic levels.

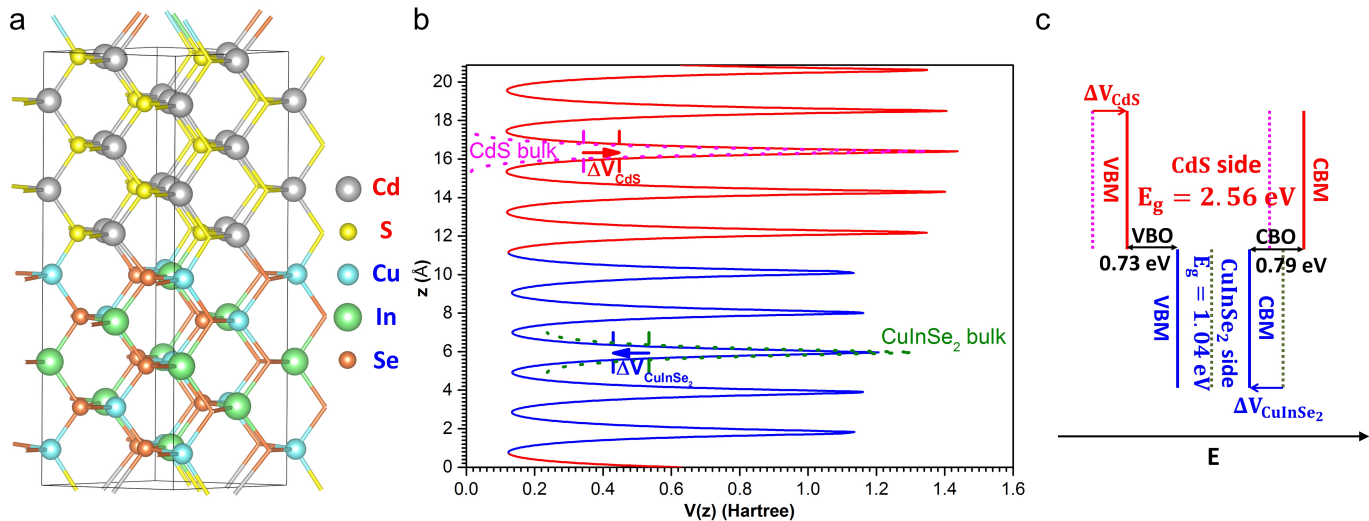


Figure 3.1. Illustration of the computation of band offsets for the CuInSe₂/CdS (110) interface: (a) supercell structure with 5 layers for each material where the vertical axis is the [001] or z axis, (b) electrostatic potential averaged over the xy plane plotted along the z direction. At the middle layer of each side, we compare to results from bulk calculations (dotted lines). This is used to obtain the potential shift ΔV for each material and (c) the final band alignment. Note that all potential shifts are exaggerated for clarity.

A critical problem in modeling interfaces with 3D PBC is the artificial interaction introduced between the interface and its image. However, if local charge neutrality holds at the interface, such dipole-dipole interactions decay as r^{-3} , so that it is of negligible influence for modest distances between the interfaces. Consequently we first performed benchmark calculations to find an optimal interface spacing that is large enough to exclude significant interface-interface interaction but reasonably small for affordable computation cost. Table 3.1 summarizes this validation, which shows clearly that convergence is achieved with ~ 10 Å distance between interfaces for the AEP method. This leads to convergence of interfacial energies within 0.004 J/m^2 and band offsets within 0.01 eV. Most importantly the predicted VBO = 0.73 eV agrees with the experimental results of VBO = 0.8 ± 0.1 eV[51]. This error of only 0.07 eV is within the MAD of 0.09 eV for predicting band gaps from B3PW91 (see Ch. 2 and references therein). This demonstrates both the stability and reliability of our methodology.

A popular alternative to AEP is to determine band offsets by using core levels as a reference[52]. As shown in Table 3.2, we find that use of the core levels from different elements leads to some fluctuations, with changes in the predicted CBO of up to 0.07 eV (as observed previously[52]). We

found that the combination with the most stable convergence is: In (4s) for CuInSe₂ side and Cd (4s) for CdS side. (Due to the use of ECP, the deepest available core levels are S (1s), In (4s), Cu (3s), and Cd (4s), in ascending energy order.) The results are shown in Table 3.1. At a large distance of ~ 19 Å between interfaces, an oscillation of 0.03 eV still remains in the calculated VBO, leading to a result 0.3 eV larger than the experimental value. In principle, with semi-local XC functionals, core levels and AEP have equivalent convergence and shift. However, the global hybrid functional B3PW91 used here includes non-local HF exchange, which makes XC potential orbital-dependent, so the KS orbitals and eigenvalues are more coupled and thus tricky to converge with respect to the interface-interface distance, i.e., they are sensitive to the presence of interface. In contrast, AEP is directly derived from electron density, which is subject to variational principle and thus steady convergence.

Table 3.1. Convergence of interface thickness (d), interfacial energy (σ), VBO (ΔE_v), and CBO (ΔE_c) with respect to number of layers of each side (L) and the interface-interface distance (D) for CuInSe₂/CdS interfaces parallel to (110) and (112). Here the interfacial energy is defined as $\sigma = (E_{\text{interface}} - \sum_i E_{\text{bulk},i})/A$, where both $E_{\text{bulk},i}$ are scaled proportionally to match numbers of units in the supercell, and A is the interface area. The superscript CL indicates band offsets calculated with core level method.

nonpolar (110)					
L	3	5	7	9	<i>Exptl.</i>
D (Å)	6.27	10.47	14.68	18.89	
d (Å)	2.08	2.07	2.08	2.08	
σ (J/m^2)	0.051	0.048	0.052	0.052	0.8 ± 0.1^a
ΔE_v (eV)	0.67	0.73	0.72	0.72	
ΔE_c (eV)	0.85	0.79	0.80	0.80	
$(\Delta E_v)_{\text{CL}}$ (eV)	1.00	1.11	1.13	1.10	
polar (112)					
L	3			6	
D (Å)		10.30		20.61	
d (Å)		2.56		2.56	
σ (J/m^2)		0.042		0.040	
ΔE_v (eV)		0.69		0.67	
ΔE_c (eV)		0.83		0.85	

^a Ref. [51].

3.2 Band offsets at pristine CIGS/CdS interfaces

Table 3.1 includes results for both the (110) nonpolar interface and the polar (112) interface commonly observed in CIGS solar cells[53]. Although the polar nature of this orientation raises problems in surface calculations due to charge separation, local neutrality still holds in each layer of the perfect

Table 3.2. Fluctuations in calculated CBO values from using core levels of different elements, illustrated by the $\text{CuInSe}_2/\text{CdS}$ (110) case with 5 layers for each side.

CuInSe_2 side	CdS side	CBO (eV)
In (4s)	Cd (4s)	1.11
Cu (3s)	Cd (4s)	1.11
In (4s)	S (1s)	1.18
Cu (3s)	S (1s)	1.18

matching interface models, as shown in Figure 3.2. Thus the argument for convergence mentioned above is valid here. Indeed, Table 3.1 shows convergence at about 10 Å in polar cases, similar to the nonpolar ones.

The calculated VBO value of 0.69 eV in (112) is only 0.04 eV smaller than for (110), indicating weak dependence of band offsets on surface orientation, which is consistent with experimental observation[54]. This indicates that the potential shift of each semiconductor side in the interface is insensitive to the detailed local structure or dipole of the interface, whether it is nonpolar or polar. Rather it is determined by the intrinsic nature of the atoms at both sides. Indeed, the average electrostatic potential we use demonstrates such character, validating that it provides the proper theoretical reference linking microscopic interface modelling with macroscopic screening in semiconductor interfaces.

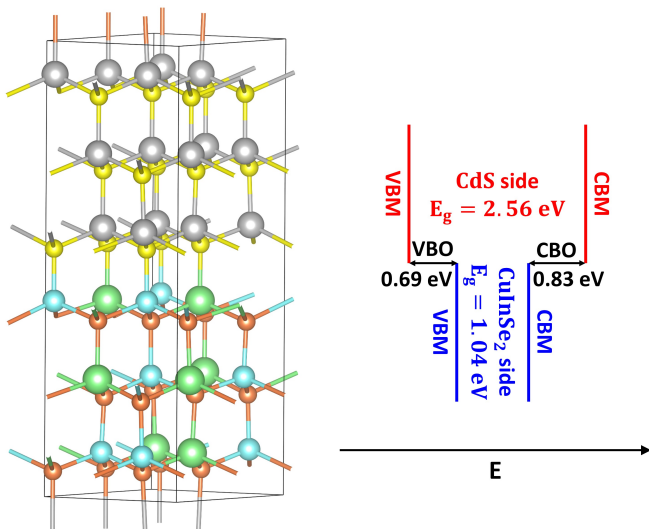


Figure 3.2. The $\text{CuInSe}_2/\text{CdS}$ (112) polar interface model and the calculated band alignment. This CBO and VBO are within 0.04 eV of the (110) case in Figure 3.1.

Strikingly, our calculations show that for the perfect interface the $\text{CBO} = 0.83$ eV, which is far from optimal, where 0 to 0.4 eV is thought to be best[55]. Such a high CBO would provide a barrier preventing transport of photo-generated electrons from absorber to buffer layer. This result would

appear to contradict the excellent performance of CIGS/CdS based solar cells. Consequently we carried out investigations to resolve the inconsistency.

We expected that the CBO is strongly affected by the distribution of vacancies and defects, so we replaced with Ga one out of the four symmetric In atoms in the conventional cell of CuInSe_2 , leading to $\text{CuIn}_{0.75}\text{Ga}_{0.25}\text{Se}_2$, which mimics the Ga concentration of ~ 0.3 in the best performance solar cells and which has a lattice mismatch within 0.7% (one additional Ga substitution in our cell would give $> 1\%$ mismatch, while the limiting case CuGaSe_2 has more than 5% lattice mismatch with CdS).

Figure 3.3 shows the supercell of the $\text{CuIn}_{0.75}\text{Ga}_{0.25}\text{Se}_2/\text{CdS}(110)$ interface. We were surprised to find that the increase of 0.13 eV in the absorber band gap goes entirely to decreasing VBO to 0.56 eV, while the CBO stays at 0.83 eV. This implies that the valence region of this absorber is more sensitive to such changes in the chemical environment addressed by band gap engineering, indicating that the CBO is not easily tuned. Indeed we find that for Cu-rich CIGS, the top of the valence band is dominated by the Cu $3d$ orbitals, as shown in Figure 3.4, suggesting that Cu vacancy could have a large effect.

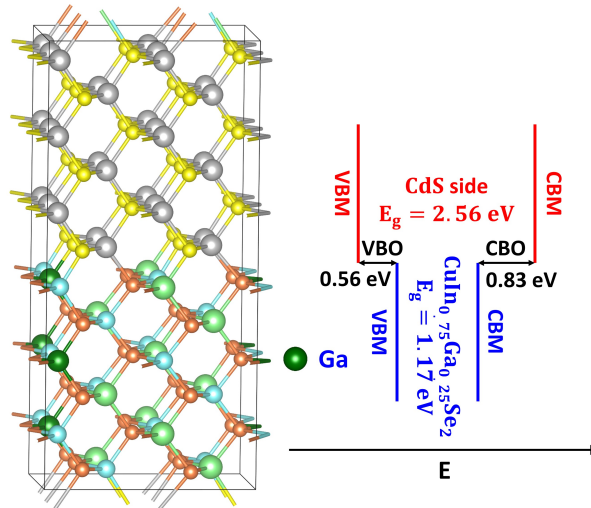


Figure 3.3. The interface models and calculated band alignments of $\text{CuIn}_{0.75}\text{Ga}_{0.25}\text{Se}_2/\text{CdS}$, where we see that the band gap increase of 0.10 eV goes entirely to decreasing the VBO.

3.3 Bulk structures of defect CIGS

Experimentally, the structure of the commonly observed Cu deficient phase CuIn_3Se_5 has been interpreted in terms of several quite different structural models, with no consensus[26]. However, some theoretical models have been proposed to investigate this phase[25–27]. Following previous

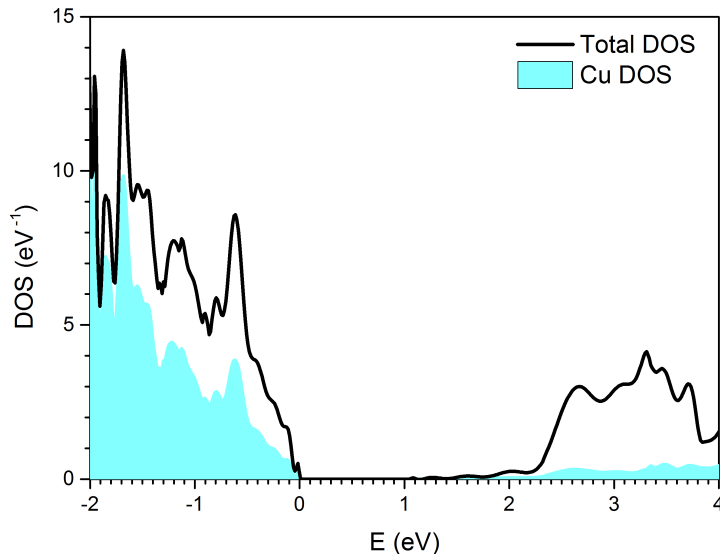


Figure 3.4. DOS of Cu-rich CuInSe_2 shows the dominance of Cu $3d$ in the valence region. The VBM is shifted to the origin.

work, we used a pristine $\sqrt{2} \times \sqrt{2} \times 1$ supercell containing $\text{Cu}_8\text{In}_8\text{Se}_{16}$ to derive two Cu-poor structures having distinctly different Cu vacancy concentrations, i.e.,

- $\text{Cu}_5\text{In}_9\text{Se}_{16}$ with 2 Cu vacancies or 12.5 at% and 1 In at a Cu site
- $\text{Cu}_2\text{In}_{10}\text{Se}_{16}$ (CuIn_5Se_8), with 4 Cu vacancies or 25 at% and 2 In at Cu sites

For $\text{Cu}_5\text{In}_9\text{Se}_{16}$ we examined all possible configurations and adopted the one with the lowest energy, while for CuIn_5Se_8 low energy configurations proposed by previous LDA and GGA studies[26, 27] were calculated with the hybrid functional B3PW91. Tables 3.3 and 3.4 list the relative energies of configurations for $\text{Cu}_5\text{In}_9\text{Se}_{16}$ and CuIn_5Se_8 , respectively. Table 3.4 also includes PBE results using both atomic Gaussian basis sets in this work and plane wave basis sets calculated with the VASP package[56–59], and the two sets of results agree very well on such subtle energy differences, which validates the use of atomic Gaussian basis sets here. Figure 3.5 illustrates the lowest energy structures for $\text{Cu}_5\text{In}_9\text{Se}_{16}$ and CuIn_5Se_8 (see Appendix for their coordinates and the rest configurations considered can be found in the supplemental material of our paper[34]). We find that just as for Ga alloying, the Cu vacancies increase the band gap. Here the B3PW91 predicted band gap of 1.30 eV for CuIn_5Se_8 phase is in excellent agreement with the experimental value of 1.27 eV[60].

Since a Cu deficient phase is universally present at the CIGS interface, the other dopants were modeled based on the $\text{Cu}_5\text{In}_9\text{Se}_{16}$ structure proposed above. Previous calculations showed the preferred sites to be substitutional Na_{Cu} and Cd_{Cu} [19, 29], so we formed the bulk structures based on replacing two Cu atoms by two Na, two K, or one Cd. That is, we considered $\text{Na}_2\text{Cu}_3\text{In}_9\text{Se}_{16}$,

Table 3.3. Relative energies (ΔE) in meV/atom of all possible configurations within a $\sqrt{2} \times \sqrt{2} \times 1$ supercell for $\text{Cu}_5\text{In}_9\text{Se}_{16}$ phase calculated with B3PW91. Note that CH and CA stand for configurations derived from chalcopyrite and CuAl-like structures, respectively.

Config.	Space group	ΔE	Config.	Space group	ΔE	Config.	Space group	ΔE
CH-1	$P\bar{4}$	23.6	CH-2	$P2$	11.2	CH-3	$P2$	11.6
CH-4	$P1$	10.5	CH-5	$P1$	18.1	CH-6	$P1$	6.6
CA-1	$P\bar{4}m2$	21.3	CA-2	$P\bar{4}m2$	21.4	CA-3	$P\bar{4}m2$	0.0
CA-4	$P\bar{4}m2$	15.5	CA-5	$Pmm2$	5.1	CA-6	$Pmm2$	12.3
CA-7	$Pmm2$	8.1	CA-8	$P\bar{4}m2$	8.8	CA-9	$Pmm2$	5.1

Table 3.4. Relative energies (ΔE) in meV/atom of low energy configurations for CuIn_5Se_8 phase calculated with B3PW91 and PBE. Note the configuration notations conform to Ref. [26, 27].

Config.	Space group	B3PW91	PBE	PBE*	Config.	Space group	B3PW91	PBE	PBE*
Type-A	$P\bar{4}m2$	4.0	3.7	4.0	Type-B	$P\bar{4}m2$	3.9	3.5	4.9
Type-C	$C222$	2.6	3.5	4.1	Type-D	$P2$	0.0	0.0	0.0
Type-E	$P\bar{4}$	10.5	8.3	8.4	Type-F	$P222$	10.1	8.7	10.0
New-1	$P\bar{4}$	1.4	1.5	1.1	New-2	$Pmm2$	1.8	2.6	2.2

* using plane wave basis sets with the PAW method.

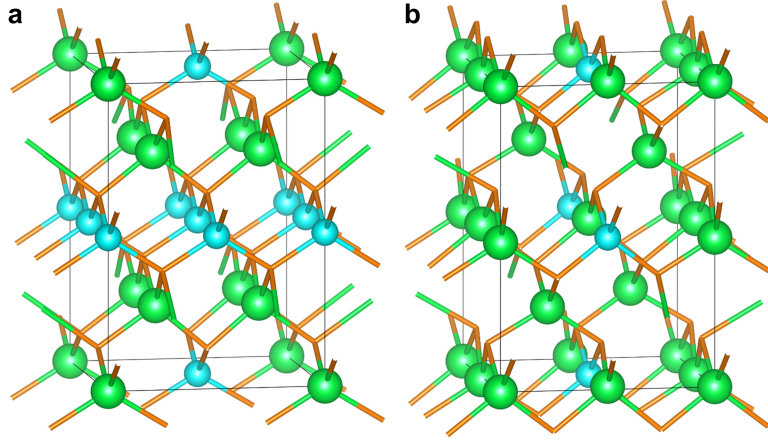


Figure 3.5. The lowest energy model crystal structures for $\text{Cu}_5\text{In}_9\text{Se}_{16}$ and CuIn_5Se_8 . (a) $\text{Cu}_5\text{In}_9\text{Se}_{16}$ with CA-3 configuration in Table 3.3; (b) CuIn_5Se_8 with Type-D configuration in Table 3.4. Se atoms are not shown for clarity.

$\text{K}_2\text{Cu}_3\text{In}_9\text{Se}_{16}$, and $\text{CdCu}_3\text{In}_9\text{Se}_{16}$. Again we calculated all possible configurations and chose the ones with the lowest total energy (details can be found in the supplemental material of our paper[34]). These configurations are consistent with each other and lead to a ratio of Cu:In:Se that is close to 1:3:5. We should point out that the optimal experimental atomic concentration of Na doping is $\sim 0.1\%$, but that Na accumulates on surfaces up to ~ 1 at%[61]. Our model bulk $\text{Na}_2\text{Cu}_3\text{In}_9\text{Se}_{16}$ has 6.7 at% Na. Nevertheless we consider that this model is reasonable to probe the physics.

3.4 Roles of defects in band offsets and energetics at CIGS/CdS interfaces

Figure 3.6 shows the interface models of $\text{Cu}_5\text{In}_9\text{Se}_{16}/\text{CdS}$ and $\text{CuIn}_5\text{Se}_8/\text{CdS}$. For the $\text{Cu}_5\text{In}_9\text{Se}_{16}$ case we find that the 12.5% concentration of Cu vacancy increases the band gap by 0.03 eV but does not change the CBO at all. However, the CuIn_5Se_8 case with 25% depletion of Cu constituents increases the band gap by 0.26 eV while raising the VBM due to the reduction in the number of chemical bonds. This tunes the CBO to 0.46 eV, very close to the optimal value. These results corroborate the speculation that Cu 3d electrons dominate the VBM region, so that the VBO depends on the electronic structure engineering, while sufficient concentration of Cu vacancies makes the VBM region dominated by the more rigid Se 4p, as shown in Figure 3.7, and VBO less variable, and thus enables tunability of the CBO. We suggest that this underlies the high efficiency of CIGS solar cells, which correlate with the presence of Cu deficient phases at the interface.

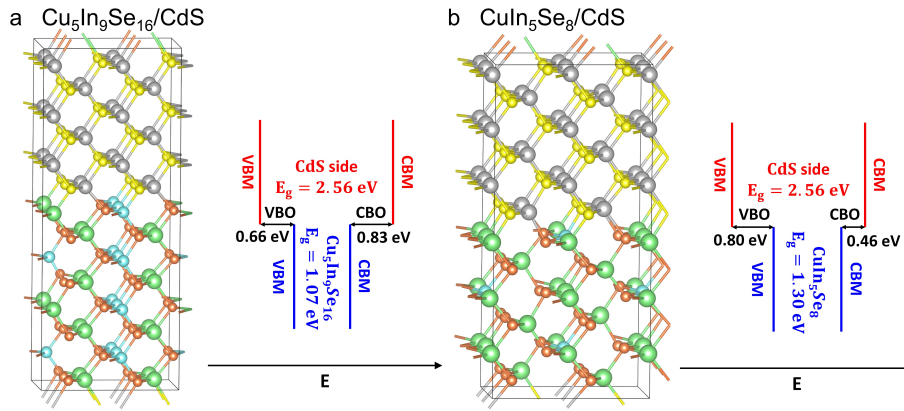


Figure 3.6. The interface models and calculated band alignments of (a) $\text{Cu}_5\text{In}_9\text{Se}_{16}/\text{CdS}$ and (b) $\text{CuIn}_5\text{Se}_8/\text{CdS}$, which increases the band gap by 0.26 eV while decreasing the CBO by 0.33 eV.

We also examined the interfacial energies, finding that Ga alloying slightly decreases the interface stability, increasing from 0.048 to 0.056 J/m^2 for the $\text{CuIn}_{0.75}\text{Ga}_{0.25}\text{Se}_2/\text{CdS}$ case while Cu vacancies dramatically decrease interfacial stability with $\sigma = 0.129 J/m^2$ for $\text{Cu}_5\text{In}_9\text{Se}_{16}/\text{CdS}$ and 0.107 J/m^2 for $\text{CuIn}_5\text{Se}_8/\text{CdS}$. This decrease in interfacial stability is the consequence of weaker bonding at the interface. Partly this results from stretching the Ga-S bonds from their preferred length of 2.32 (in CuGaS_2 bulk) to 2.36 Å at the interface and partly it is because of fewer chemical bonds due to Cu vacancies. However, these interfacial energies are all rather small, so that the interfacial stability effects are far less important than the band offsets.

Figure 3.8a,b show the interfacial models of $\text{Na}_2\text{Cu}_3\text{In}_9\text{Se}_{16}/\text{CdS}$ and $\text{K}_2\text{Cu}_3\text{In}_9\text{Se}_{16}/\text{CdS}$. Indeed, we find that Na tunes the CBO from 0.83 eV to 0.45 eV while K tunes it to 0.05 eV. Thus both alkalis move toward the optimal values while changing the overall band gap by 0.27 eV for

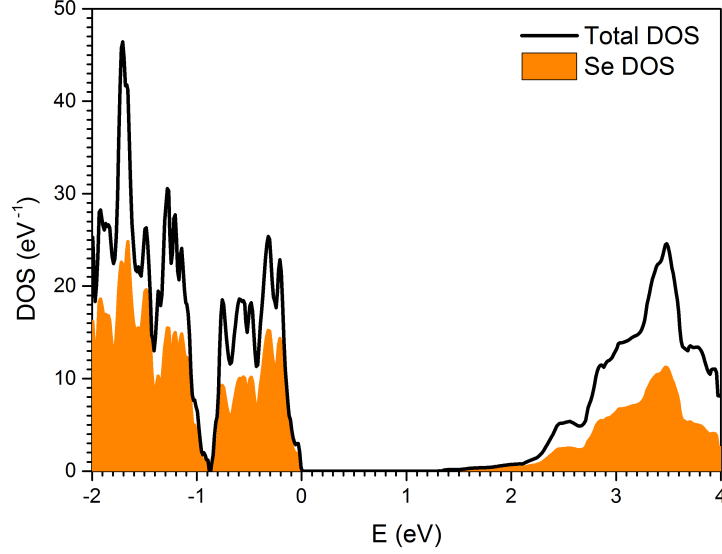


Figure 3.7. DOS of Cu-poor CuIn_5Se_8 shows the dominance of Se $4p$ in the valence region. The VBM is shifted to the origin.

Na and 0.20 eV for K. That a different mechanism is responsible is clearest for the K case, where the reduction of CBO by 0.78 eV to 0.05 eV is mostly due to raising the VBM by 0.58 eV. Thus the presence of these very positively charged alkali elements attracts electrons in the valence region (from either Cu $3d$ or Se $4p$), pushing up the energy. Therefore, it is the electrostatics that gives Na and K a better capability for optimizing the CBO. However, both Na and K possess larger ionic sizes than Cu, leading to increased interfacial energies to 0.138 J/m^2 for Na and 0.151 J/m^2 for K. Such small changes are far from detrimental, as discussed above.

Indeed, the dramatic benefit of K to CBO is consistent with recent experiment, in which sequential post-deposition treatment with NaF and KF results in better performance[6]. However, K possesses much larger ionic size, and might introduce structural instability. This can be estimated by considering a simple decomposition energy ΔE_d , defined as

$$\Delta E_d \equiv E(\text{A}_2\text{Se}) + \frac{3}{2} [E(\text{CuInSe}_2) + E(\text{CuIn}_5\text{Se}_8)] - E(\text{A}_2\text{Cu}_3\text{In}_9\text{Se}_2) \quad (3.1)$$

where A is an alkali element. For Na, $\Delta E_d = 4.7 \text{ kcal/mol}$, implies spontaneous formation of doped structure. For K, on the other hand, $\Delta E_d = -16.7 \text{ kcal/mol}$, shows a relatively strong tendency of the doped structure to decompose. Therefore, we suggest that the performance can be optimized by tuning the ratio of Na to K to be optimal, with K improving the CBO and Na stabilizing the doping.

The remaining interface model, $\text{CdCu}_3\text{In}_9\text{Se}_{16}/\text{CdS}$, shown in Figure 3.8c, uncovers the effects

of intermixing at the interface. The CBO is compliantly tuned by the increase in the band gap, very likely due to the Cu vacancy, while the Cd impurity does not seem to play a significant role. Similarly, the interfacial energy increases further to 0.225 J/m^2 , which again is not a substantial effect.

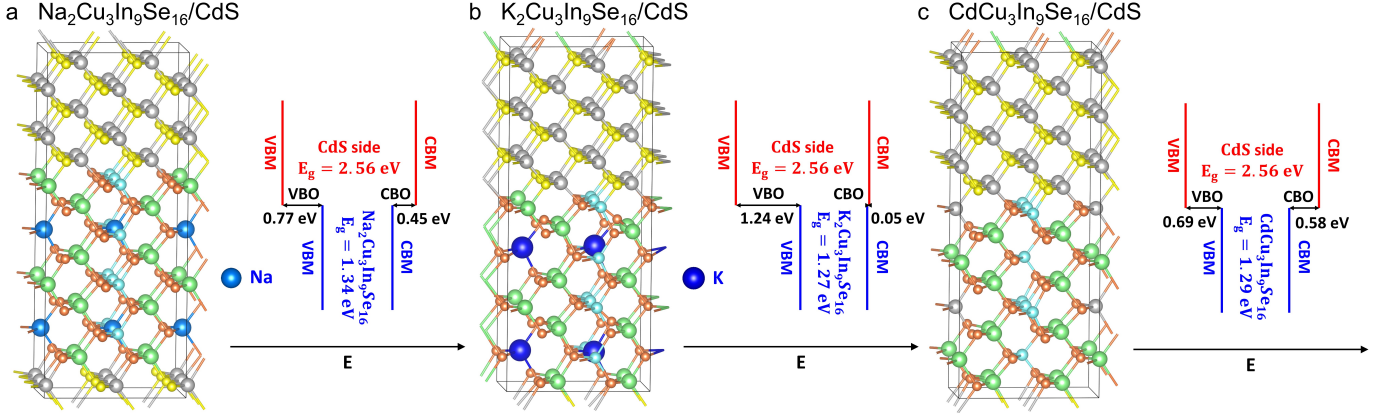


Figure 3.8. The interface models and calculated band alignments of (a) $\text{Na}_2\text{Cu}_3\text{In}_9\text{Se}_{16}/\text{CdS}$, which increases the band gap by 0.27 eV while decreasing the CBO by 0.38 eV, (b) $\text{K}_2\text{Cu}_3\text{In}_9\text{Se}_{16}/\text{CdS}$, which increases the band gap by 0.20 eV while decreasing the CBO by 0.78 eV and (c) $\text{CdCu}_3\text{In}_9\text{Se}_{16}/\text{CdS}$, which increases the band gap by 0.22 eV while decreasing the CBO by 0.35 eV.

3.5 Concluding remarks

To elucidate the effects of defects on band offsets at CIGS/CdS interfaces, we applied the B3PW91 hybrid functional and used average electrostatic potentials for reference levels to obtain the offsets. We first validated our methodology with benchmark calculations on pristine $\text{CuInSe}_2/\text{CdS}$ interfaces for both nonpolar (110) and polar (112) cases. We found that an interface-interface distance of around 10 \AA is sufficient for good convergence of interface geometry, interfacial energy, and band offsets. We validated that these results ($\text{VBO} = 0.73 \text{ eV}$) lead to excellent agreement with experiment, $\text{VBO} = 0.8 \pm 0.1 \text{ eV}$. We also evaluated the core level method for predicting band offsets, but we found both poor convergence and accuracy, suggesting that core levels provide poor reference levels for predicting band offsets with hybrid functionals.

Our studies show that band offsets depend only weakly on the surface orientation (increasing by 0.04 eV for the polar (112) vs nonpolar (220)), which is consistent with experimental observations. We then built optimized models of bulk CIGS structures having various defect or dopant compositions and carried out calculations for the interface to CdS. Here we investigate the effects on both band offsets and interfacial energies. We find that band gap widening (by 0.13 eV) by Ga alloying (with Cu-rich phases) results only in modifying the VBO, with the CBO staying near 0.83 eV, which is far too large for an efficient solar cell. However, we find that introducing at the

interface Cu vacancy concentrations close to experiment leads to a dramatic decrease in the CBO to 0.46 eV, a nearly satisfactory value (best performance is expected for < 0.4 eV). We find that the Cu vacancies eliminate the dominance of the Cu 3d levels on the VBM. This removes the sensitivity of the VBM to band gap engineering, enabling tunability of the CBO. This shows that Cu vacancies play a critical importance on performance.

Furthermore, we show that addition of alkali elements Na and K improves the CBO, but via a different mechanism. Here they elevate the VBM and thus CBM (band gap region) through electrostatics. The effect of Na is to decrease CBO slightly to 0.45 eV, which may explain the improved performance with Na. We predict that K has a much stronger effect on CBO than Na, reducing CBO to 0.05 eV. However, we find that K tends to destabilize the defect phase, whereas Na stabilizes it. Thus we propose that the performance of CIGS devices may be further optimized through tuning the ratio of Na to K. On the other hand, Cd dopants lead to a slight increase in CBO to 0.58 eV, indicating possible deleterious effects. Finally, all defects and dopants tend to decrease the interfacial stability, but the magnitude seems small enough (0.01 to 0.18 J/m^2) to be only a minor issue.

Appendix

All ECP and **optimized** basis sets used in this chapter, with the CRYSTAL09 input format.

Na basis set optimized in fictitious chalcopyrite NaInSe₂ crystal structure,
with CuInSe₂ experimental crystal structure

```

11 6
0 0 8 2.0 1.0
 56700.0000000      0.0002250
  8060.0000000      0.0019100
 1704.0000000      0.0105000
  443.6000000      0.0500600
 133.1000000      0.1691000
  45.8000000      0.3658000
  17.7500000      0.3998000
   7.3800000      0.1494000
0 1 5 8.0 1.0
 119.0000000      -0.0067300      0.0080300
  25.3300000      -0.0798000      0.0639000
   7.8000000      -0.0793000      0.2074000
   3.0000000      0.3056000      0.3398000
   1.2890000      0.5639000      0.3726000
0 1 1 1.0 1.0
  1.5294700      1.0000000      1.0000000
0 1 1 0.0 1.0
  0.5028040      1.0000000      1.0000000
0 1 1 0.0 1.0
  0.0901240      1.0000000      1.0000000
0 3 1 0.0 1.0
  0.3199450      1.0000000

```

S basis set optimized in experimental CdS crystal structure

```

16 6
0 0 8 2.0 1.0
109211.0000000      0.0002520
16235.2060000      0.0019934
 3573.0286000      0.0111177
  943.2381100      0.0498945
  287.2617900      0.1661455
   99.9142260      0.3627018
   38.6021370      0.4108787

```

	15.5312240	0.1457875	
0 1 6	8.0 1.0		
	281.2217100	-0.0057780	0.0081427
	67.1065750	-0.0665855	0.0565570
	21.7941350	-0.1203552	0.2039582
	8.2097646	0.2741310	0.3973328
	3.4178289	0.6463829	0.3946313
	1.5452225	0.2925792	0.1544345
0 1 3	6.0 1.0		
	7.3626800	-0.0856710	-0.0368270
	2.3028000	-0.8614760	0.0363180
	0.8397090	0.5051340	0.9986630
0 1 1	0.0 1.0		
	0.3125210	1.0000000	1.0000000
0 1 1	0.0 1.0		
	0.1176550	1.0000000	1.0000000
0 3 1	0.0 1.0		
	0.4603150	1.0000000	

K basis set optimized in fictitious chalcopyrite KInSe_2 crystal structure,
with CuInSe_2 experimental crystal structure

19 7

0 0 8	2.0 1.0		
	172500.0000000	0.0002200	
	24320.0000000	0.0019200	
	5140.0000000	0.0110900	
	1343.9000000	0.0499200	
	404.5000000	0.1702000	
	139.4000000	0.3679000	
	54.3900000	0.4036000	
	22.7100000	0.1459000	
0 1 6	8.0 1.0		
	402.0000000	-0.0060300	0.0084100
	93.5000000	-0.0805000	0.0602000
	30.7500000	-0.1094000	0.2117000
	11.9100000	0.2580000	0.3726000
	5.1670000	0.6840000	0.4022000
	1.5820000	0.3990000	0.1860000
0 1 4	8.0 1.0		
	17.3500000	-0.0074000	-0.0321000
	7.5500000	-0.1290000	-0.0620000
	2.9390000	-0.6834000	0.1691000
	1.1900000	1.0800000	1.5000000
0 1 1	1.0 1.0		
	1.1296700	1.0000000	1.0000000
0 1 1	0.0 1.0		
	0.4514560	1.0000000	1.0000000
0 1 1	0.0 1.0		
	0.1579380	1.0000000	1.0000000
0 3 1	0.0 1.0		
	0.2961560	1.0000000	

Cu basis set optimized in CuInSe_2 experimental crystal structure

229 8
INPUT

19.0	1 3 2 0 0 0		
	23.2906000	-4.0027600	-1
	2.6205900	3.3246500	-2
	7.8108200	224.3233000	0
	6.6332400	-180.3047000	0
	51.1573400	3.4213000	-2
	14.7340600	105.7012600	0
0 1 4	8.0 1.0		
	83.4200000	-0.0048290	-0.0082840
	7.9700000	-0.6447990	-0.3218950
	5.6000000	0.2652400	0.6181330
	1.9320000	1.1897910	0.7221840
0 1 1	1.0 1.0		
	2.3598900	1.0000000	1.0000000
0 1 1	0.0 1.0		
	0.6953090	1.0000000	1.0000000
0 1 1	0.0 1.0		
	0.3178440	1.0000000	1.0000000
0 1 1	0.0 1.0		
	0.1072360	1.0000000	1.0000000
0 3 4	10.0 1.0		
	65.8000000	0.0255970	
	18.8200000	0.1486090	

	6.5380000	0.4117860	
	2.3480000	0.6055070	
0 3 1	0.0 1.0		
	0.7696750	1.0000000	
0 3 1	0.0 1.0		
	0.2329060	1.0000000	

Ga basis set optimized in CuGaSe₂ experimental crystal structure

231 8

INPUT

21.0	1 3 2 0 0 0		
	26.7430200	-3.8736300	-1
	3.4653000	4.1247200	-2
	9.1113000	260.7326300	0
	7.8932900	-223.9600300	0
	79.9935300	4.2003300	-2
	17.3911400	127.9913900	0
0 1 4	8.0 1.0		
	113.9000000	-0.0017110	-0.0080460
	9.1550000	-0.8230360	-0.3574320
	6.6330000	0.4586180	0.6637940
	2.2780000	1.1618170	0.7136190
0 1 1	3.0 1.0		
	3.8605400	1.0000000	1.0000000
0 1 1	0.0 1.0		
	0.8549090	1.0000000	1.0000000
0 1 1	0.0 1.0		
	0.3091850	1.0000000	1.0000000
0 1 1	0.0 1.0		
	0.1192010	1.0000000	1.0000000
0 3 4	10.0 1.0		
	70.4300000	0.0288770	
	21.0500000	0.1662530	
	7.4010000	0.4277760	
	2.7520000	0.5704100	
0 3 1	0.0 1.0		
	0.9741730	1.0000000	
0 3 1	0.0 1.0		
	0.3306270	1.0000000	

Se basis set optimized in CdSe experimental crystal structure

234 4

INPUT

6.0	1 2 2 2 0 0		
	2.0935600	-5.5849800	-1
	20.5564400	13.2808100	-2
	3.1549000	51.0001100	0
	2.5849500	1.7964000	-2
	2.5852600	30.4378700	0
	1.3829000	2.4000100	-2
	1.4267100	6.5994800	0
0 1 3	6.0 1.0		
	2.6357000	0.3984680	0.1574060
	1.9124800	-0.9303030	-0.6222610
	0.7563100	0.2078380	0.7633640
0 1 1	0.0 1.0		
	0.2865600	1.0000000	1.0000000
0 1 1	0.0 1.0		
	0.1136360	1.0000000	1.0000000
0 3 1	0.0 1.0		
	0.3166550	1.0000000	

Cd basis set optimized in CdS experimental crystal structure

248 8

INPUT

20.0	1 3 3 2 0 0		
	9.8132500	-8.6986400	-1
	1.6047600	6.5693400	-2
	3.3772700	-59.3639500	0
	5.0887600	93.5961000	0
	1.2517100	3.6786300	-2
	3.4259200	-104.5069400	0
	4.2141500	145.6731600	0
	22.3533700	3.3309400	-2
	6.7540800	62.0661600	0
0 1 4	8.0 1.0		
	63.3800000	-0.0004640	-0.0048740
	6.7140000	2.2928770	0.1896300

	5.6020000	-3.9028840	-0.4918720
	1.9710000	2.0846040	1.2135010
0 1 1	2.0 1.0		
	2.6058700	1.0000000	1.0000000
0 1 1	0.0 1.0		
	0.7850690	1.0000000	1.0000000
0 1 1	0.0 1.0		
	0.2887310	1.0000000	1.0000000
0 1 1	0.0 1.0		
	0.1133660	1.0000000	1.0000000
0 3 3	10.0 1.0		
	15.5100000	0.0120650	
	2.9410000	0.3701680	
	1.3790000	0.6807600	
0 3 1	0.0 1.0		
	0.5775670	1.0000000	
0 3 1	0.0 1.0		
	0.2227450	1.0000000	

In basis set optimized in CuInSe₂ experimental crystal structure

249 8

INPUT

21.0	1 3 3 2 0 0		
	10.5898700	-8.8403100	-1
	1.7388300	6.9012400	-2
	3.6280600	-68.4831900	0
	5.3027000	101.7727200	0
	1.4304500	3.9855400	-2
	3.7444700	-129.7859400	0
	4.4767900	171.9048700	0
	29.1607200	3.4924400	-2
	7.2656600	68.2781600	0
0 1 4	8.0 1.0		
	71.7600000	0.0007330	-0.0045130
	7.6540000	1.0897810	0.0316150
	5.6160000	-2.7310890	-0.3380060
	2.1040000	2.1128440	1.2134640
0 1 1	3.0 1.0		
	2.7577000	1.0000000	1.0000000
0 1 1	0.0 1.0		
	0.8351740	1.0000000	1.0000000
0 1 1	0.0 1.0		
	0.2459350	1.0000000	1.0000000
0 1 1	0.0 1.0		
	0.1093360	1.0000000	1.0000000
0 3 3	10.0 1.0		
	17.1600000	0.0148930	
	3.1270000	0.3881350	
	1.4750000	0.6626390	
0 3 1	0.0 1.0		
	0.6383770	1.0000000	
0 3 1	0.0 1.0		
	0.2564740	1.0000000	

The lowest energy model crystal structure for Cu₅In₉Se₁₆ predicted with B3PW91:

Space group: $P\bar{4}m2$

Lattice parameters: $a = 8.327435 \text{ \AA}$, $c = 11.743536 \text{ \AA}$

Fractional coordinates:

Cu	0.500000	0.500000	0.000000
Cu	0.500000	0.500000	0.500000
Cu	0.500000	0.000000	-0.498358
Cu	0.000000	0.500000	0.498358
Cu	0.000000	0.000000	0.500000
In	-0.250239	0.261367	0.249797
In	0.250239	-0.261367	0.249797
In	-0.261367	0.250239	-0.249797
In	0.261367	-0.250239	-0.249797
In	0.250239	0.261367	0.249797
In	-0.250239	-0.261367	0.249797
In	-0.261367	-0.250239	-0.249797
In	0.261367	0.250239	-0.249797
In	0.000000	0.000000	0.000000
Se	-0.269995	0.000000	0.116544
Se	0.269995	0.000000	0.116544
Se	0.000000	0.269995	-0.116544

```

Se  0.000000 -0.269995 -0.116544
Se -0.249364  0.000000 -0.386869
Se  0.249364  0.000000 -0.386869
Se  0.000000  0.249364  0.386869
Se  0.000000 -0.249364  0.386869
Se  0.242897  0.500000  0.108132
Se -0.242897  0.500000  0.108132
Se  0.500000 -0.242897 -0.108132
Se  0.500000  0.242897 -0.108132
Se  0.248753  0.500000 -0.387034
Se -0.248753  0.500000 -0.387034
Se  0.500000 -0.248753  0.387034
Se  0.500000  0.248753  0.387034

```

The lowest energy model crystal structure for CuIn_5Se_8 predicted with B3PW91:

Space group: $P2$

Lattice parameters: $a = 8.309972 \text{ \AA}$, $b = 11.776104 \text{ \AA}$, $c = 8.313099 \text{ \AA}$, $\beta = 90.104095^\circ$

Fractional coordinates:

```

Cu  0.500000 -0.001138  0.500000
Cu  0.500000  0.498865  0.000000
In  0.000000  0.000656  0.000000
In  0.000000 -0.009829  0.500000
In  0.000000  0.490173  0.000000
In  0.000000 -0.499344  0.500000
In  0.260693 -0.249401  0.262047
In -0.260693 -0.249401 -0.262047
In  0.500000  0.010273  0.000000
In  0.500000 -0.489729  0.500000
In -0.260687  0.250597  0.237937
In  0.260687  0.250597 -0.237937
Se  0.018385  0.135373  0.252103
Se -0.018385  0.135373 -0.252103
Se  0.018379 -0.364625 -0.247898
Se -0.018379 -0.364625  0.247898
Se  0.251618  0.364813  0.482787
Se -0.251618  0.364813 -0.482787
Se  0.262334 -0.127917 -0.478605
Se -0.262334 -0.127917  0.478605
Se  0.251621 -0.135186 -0.017228
Se -0.251621 -0.135186  0.017228
Se  0.482268  0.127150  0.263523
Se -0.482268  0.127150 -0.263523
Se -0.482263 -0.372851  0.236477
Se  0.482263 -0.372851 -0.236477
Se -0.262334  0.372084 -0.021406
Se  0.262334  0.372084  0.021406

```

References

- [1] REN21. (2013) *Renewables 2013 Global Status Report*. (REN21 Secretariat, Paris).
- [2] Jäger-Waldau, A. (2013) *PV Status Report 2013*. (Publications Office of the European Union, Luxembourg).
- [3] Chopra, K. L, Paulson, P. D, & Dutta, V. (2004) Thin-film solar cells: an overview. *Prog. Photovoltaics* **12**, 69–92.
- [4] Jackson, P, Hariskos, D, Lotter, E, Paetel, S, Wuerz, R, Menner, R, Wischmann, W, & Powalla, M. (2011) New world record efficiency for Cu(In,Ga)Se_2 thin-film solar cells beyond 20%. *Prog. Photovoltaics* **19**, 894–897.

- [5] Chirilă, A, Buecheler, S, Pianezzi, F, Bloesch, P, Gretener, C, Uhl, A. R, Fella, C, Kranz, L, Perrenoud, J, Seyrling, S, Verma, R, Nishiwaki, S, Romanyuk, Y. E, Bilger, G, & Tiwari, A. N. (2011) Highly efficient Cu(In,Ga)Se₂ solar cells grown on flexible polymer films. *Nature Mater.* **10**, 857–861.
- [6] Chirilă, A, Reinhard, P, Pianezzi, F, Bloesch, P, Uhl, A. R, Fella, C, Kranz, L, Keller, D, Gretener, C, Hagendorfer, H, Jaeger, D, Erni, R, Nishiwaki, S, Buecheler, S, & Tiwari, A. N. (2013) Potassium-induced surface modification of Cu(In,Ga)Se₂ thin films for high-efficiency solar cells. *Nature Mater.* **12**, 1107–1111.
- [7] Schmid, D, Ruckh, M, Grunwald, F, & Schock, H. W. (1993) Chalcopyrite/defect chalcopyrite heterojunctions on the basis of CuInSe₂. *J. Appl. Phys.* **73**, 2902–2909.
- [8] Schmid, D, Ruckh, M, & Schock, H. W. (1996) Photoemission studies on Cu(In,Ga)Se₂ thin films and related binary selenides. *Appl. Surf. Sci.* **103**, 409–429.
- [9] Rau, U & Schock, H. W. (1999) Electronic properties of Cu(In,Ga)Se₂ heterojunction solar cells—recent achievements, current understanding, and future challenges. *Appl. Phys. A* **69**, 131–147.
- [10] Kemell, M, Ritala, M, & Leskelä, M. (2005) Thin film deposition methods for CuInSe₂ solar cells. *Crit. Rev. Solid State Mater. Sci.* **30**, 1–31.
- [11] Klenk, R. (2001) Characterisation and modelling of chalcopyrite solar cells. *Thin Solid Films* **387**, 135–140.
- [12] Hedstrom, J, Ohlsen, H, Bodegard, M, Kylner, A, Stolt, L, Hariskos, D, Ruckh, M, & Schock, H. (1993) *Photovoltaic Specialists Conference, 1993., Conference Record of the Twenty Third IEEE*. (IEEE, Louisville, KY), pp. 364–371.
- [13] Granath, K, Bodegård, M, & Stolt, L. (2000) The effect of NaF on Cu(In,Ga)Se₂ thin film solar cells. *Sol. Energy Mater. Sol. Cells* **60**, 279–293.
- [14] Rudmann, D. (2004) Ph.D. thesis (Swiss Federal Institute of Technology (ETH) in Zürich).
- [15] Rockett, A. (2005) The effect of Na in polycrystalline and epitaxial single-crystal CuIn_{1-x}Ga_xSe₂. *Thin Solid Films* **480-481**, 2–7.
- [16] Ishizuka, S, Yamada, A, Islam, M. M, Shibata, H, Fons, P, Sakurai, T, Akimoto, K, & Niki, S. (2009) Na-induced variations in the structural, optical, and electrical properties of Cu(In,Ga)Se₂ thin films. *J. Appl. Phys.* **106**, 034908.

- [17] Couzinié-Devy, F, Barreau, N, & Kessler, J. (2011) Re-investigation of preferential orientation of Cu(In,Ga)Se₂ thin films grown by the three-stage process. *Prog. Photovoltaics* **19**, 527–536.
- [18] Schroeder, D. J & Rockett, A. A. (1997) Electronic effects of sodium in epitaxial CuIn_{1-x}Ga_xSe₂. *J. Appl. Phys.* **82**, 4982–4985.
- [19] Oikkonen, L. E, Ganchenkova, M. G, Seitsonen, A. P, & Nieminen, R. M. (2013) Effect of sodium incorporation into CuInSe₂ from first principles. *J. Appl. Phys.* **114**, 083503.
- [20] Nakada, T & Kunioka, A. (1999) Direct evidence of Cd diffusion into Cu(In,Ga)Se₂ thin films during chemical-bath deposition process of CdS films. *Appl. Phys. Lett.* **74**, 2444–2446.
- [21] Liao, D & Rockett, A. (2003) Cd doping at the CuInSe₂/CdS heterojunction. *J. Appl. Phys.* **93**, 9380–9382.
- [22] Cojocaru-Mirédin, O, Choi, P, Wuerz, R, & Raabe, D. (2011) Atomic-scale characterization of the CdS/CuInSe₂ interface in thin-film solar cells. *Appl. Phys. Lett.* **98**, 103504.
- [23] Jiang, C.-S, Hasoon, F. S, Moutinho, H. R, Al-Thani, H. A, Romero, M. J, & Al-Jassim, M. M. (2003) Direct evidence of a buried homojunction in Cu(In,Ga)Se₂ solar cells. *Appl. Phys. Lett.* **82**, 127–129.
- [24] Mungan, E. S, Wang, X, & Alam, M. A. (2013) Modeling the effects of Na incorporation on CIGS solar cells. *IEEE J. Photovolt.* **3**, 451–456.
- [25] Zhang, S. B, Wei, S. H, & Zunger, A. (1997) Stabilization of ternary compounds via ordered arrays of defect pairs. *Phys. Rev. Lett.* **78**, 4059–4062.
- [26] Chang, C. H, Wei, S.-H, Johnson, J. W, Zhang, S. B, Leyarovska, N, Bunker, G, & Anderson, T. J. (2003) Local structure of CuIn₃Se₅: X-ray absorption fine structure study and first-principles calculations. *Phys. Rev. B* **68**, 054108.
- [27] Ludwig, C. D. R, Gruhn, T, Felser, C, & Windeln, J. (2011) Defect structures in CuInSe₂: A combination of monte carlo simulations and density functional theory. *Phys. Rev. B* **83**, 174112.
- [28] Wei, S.-H, Zhang, S. B, & Zunger, A. (1999) Effects of Na on the electrical and structural properties of CuInSe₂. *J. Appl. Phys.* **85**, 7214–7218.
- [29] Kiss, J, Gruhn, T, Roma, G, & Felser, C. (2013) Theoretical study on the structure and energetics of Cd insertion and Cu depletion of CuIn₅Se₈. *J. Phys. Chem. C* **117**, 10892–10900.
- [30] Kiss, J, Gruhn, T, Roma, G, & Felser, C. (2013) Theoretical study on the diffusion mechanism of Cd in the Cu-poor phase of CuInSe₂ solar cell material. *J. Phys. Chem. C* **117**, 25933–25938.

- [31] Lany, S & Zunger, A. (2004) Metal-dimer atomic reconstruction leading to deep donor states of the anion vacancy in II-VI and chalcopyrite semiconductors. *Phys. Rev. Lett.* **93**, 156404.
- [32] Lany, S & Zunger, A. (2008) Intrinsic *DX* centers in ternary chalcopyrite semiconductors. *Phys. Rev. Lett.* **100**, 016401.
- [33] Oikkonen, L. E, Ganchenkova, M. G, Seitsonen, A. P, & Nieminen, R. M. (2011) Vacancies in CuInSe₂: new insights from hybrid-functional calculations. *J. Phys.: Condens. Matter* **23**, 422202.
- [34] Xiao, H & Goddard, W. A. (2014) Predicted roles of defects on band offsets and energetics at CIGS (Cu(In,Ga)Se₂/CdS) solar cell interfaces and implications for improving performance. *J. Chem. Phys.* **141**, 094701.
- [35] Vladimir, I. A, Aryasetiawan, F, & Lichtenstein, A. I. (1997) First-principles calculations of the electronic structure and spectra of strongly correlated systems: the LDA + U method. *J. Phys.: Condens. Matter* **9**, 767–808.
- [36] Aryasetiawan, F & Gunnarsson, O. (1998) The GW method. *Rep. Prog. Phys.* **61**, 237–312.
- [37] Dovesi, R, Saunders, V. R, Roetti, C, Orlando, R, Zicovich-Wilson, C. M, Pascale, F, Civalieri, B, Doll, K, Harrison, N. M, Bush, I. J, DArco, P, & Llunell, M. (2009) *CRYSTAL 2009 User's Manual*. (University of Torino, Torino).
- [38] Dovesi, R, Roetti, C, Freyria-Fava, C, Prencipe, M, & Saunders, V. R. (1991) On the elastic properties of lithium, sodium and potassium oxide. an ab initio study. *Chem. Phys.* **156**, 11–19.
- [39] Lichanot, A, Aprà, E, & Dovesi, R. (1993) Quantum mechanical Hartree-Fock study of the elastic properties of Li₂S and Na₂S. *Phys. Status Solidi B* **177**, 157–163.
- [40] Goddard, W. A. (1968) New foundation for the use of pseudopotentials in metals. *Phys. Rev.* **174**, 659–662.
- [41] Kahn, L. R & Goddard, W. A. (1972) Ab initio effective potentials for use in molecular calculations. *J. Chem. Phys.* **56**, 2685–2701.
- [42] Melius, C. F & Goddard, W. A. (1974) Ab initio effective potentials for use in molecular quantum mechanics. *Phys. Rev. A* **10**, 1528–1540.
- [43] Kahn, L. R, Baybutt, P, & Truhlar, D. G. (1976) Ab initio effective core potentials: Reduction of all-electron molecular structure calculations to calculations involving only valence electrons. *J. Chem. Phys.* **65**, 3826–3853.

- [44] Stevens, W. J, Krauss, M, Basch, H, & Jasien, P. G. (1992) Relativistic compact effective potentials and efficient, shared-exponent basis sets for the third-, fourth-, and fifth-row atoms. *Can. J. Chem.* **70**, 612–630.
- [45] Peralta, J. E, Heyd, J, Scuseria, G. E, & Martin, R. L. (2006) Spin-orbit splittings and energy band gaps calculated with the Heyd-Scuseria-Ernzerhof screened hybrid functional. *Phys. Rev. B* **74**, 073101.
- [46] Monkhorst, H. J & Pack, J. D. (1976) Special points for Brillouin-zone integrations. *Phys. Rev. B* **13**, 5188–5192.
- [47] Van de Walle, C. G & Martin, R. M. (1987) Theoretical study of band offsets at semiconductor interfaces. *Phys. Rev. B* **35**, 8154–8165.
- [48] Paasch, G & von Faber, E. (1990) Connections between work functions, Schottky barriers, and heterojunction band offsets. *Prog. Surf. Sci.* **35**, 19–33.
- [49] Saunders, V. R, Freyria-Fava, C, Dovesi, R, Salasco, L, & Roetti, C. (1992) On the electrostatic potential in crystalline systems where the charge density is expanded in Gaussian functions. *Mol. Phys.* **77**, 629–665.
- [50] Saunders, V. R, Freyria-Fava, C, Dovesi, R, & Roetti, C. (1994) On the electrostatic potential in linear periodic polymers. *Comput. Phys. Commun.* **84**, 156–172.
- [51] Löher, T, Jaegermann, W, & Pettenkofer, C. (1995) Formation and electronic properties of the CdS/CuInSe₂ (011) heterointerface studied by synchrotron-induced photoemission. *J. Appl. Phys.* **77**, 731–738.
- [52] Wei, S.-H & Zunger, A. (1993) Band offsets at the CdS/CuInSe₂ heterojunction. *Appl. Phys. Lett.* **63**, 2549–2551.
- [53] Schlenker, T, Laptev, V, Schock, H. W, & Werner, J. H. (2005) Substrate influence on Cu(In,Ga)Se₂ film texture. *Thin Solid Films* **480-481**, 29–32.
- [54] Schulmeyer, T, Hunger, R, Klein, A, Jaegermann, W, & Niki, S. (2004) Photoemission study and band alignment of the CuInSe₂(001)/CdS heterojunction. *Appl. Phys. Lett.* **84**, 3067–3069.
- [55] Minemoto, T, Matsui, T, Takakura, H, Hamakawa, Y, Negami, T, Hashimoto, Y, Uenoyama, T, & Kitagawa, M. (2001) Theoretical analysis of the effect of conduction band offset of window/CIS layers on performance of CIS solar cells using device simulation. *Sol. Energy Mater. Sol. Cells* **67**, 83–88.

- [56] Kresse, G & Hafner, J. (1993) Ab initio molecular dynamics for liquid metals. *Phys. Rev. B* **47**, 558–561.
- [57] Kresse, G & Furthmuller, J. (1996) Efficiency of ab-initio total energy calculations for metals and semiconductors using a plane-wave basis set. *Comput. Mater. Sci.* **6**, 15–50.
- [58] Kresse, G & Furthmuller, J. (1996) Efficient iterative schemes for ab initio total-energy calculations using a plane-wave basis set. *Phys. Rev. B* **54**, 11169–11186.
- [59] Kresse, G & Joubert, D. (1999) From ultrasoft pseudopotentials to the projector augmented-wave method. *Phys. Rev. B* **59**, 1758–1775.
- [60] Levchenko, S, Syrbu, N. N, Arushanov, E, Tezlevan, V, Fernández-Ruiz, R, Merino, J. M, & León, M. (2006) Optical properties of monocrystalline CuIn_5Se_8 . *J. Appl. Phys.* **99**, 073513.
- [61] Cadel, E, Barreau, N, Kessler, J, & Pareige, P. (2010) Atom probe study of sodium distribution in polycrystalline $\text{Cu}(\text{In,Ga})\text{Se}_2$ thin film. *Acta Mater.* **58**, 2634–2637.

Chapter 4

Formation of the $-\text{N}(\text{NO})\text{N}(\text{NO})-$ polymer at high pressure and stabilization at ambient conditions

The contents presented in this chapter are based on [H. Xiao](#), Q. An, W. A. Goddard, III, W.-G. Liu and S. V. Zybin, “Formation of the $-\text{N}(\text{NO})\text{N}(\text{NO})-$ polymer at high pressure and stabilization at ambient conditions”, *Proc. Natl. Acad. Sci. U.S.A.* **2013**, *110*, 5321-5325.

With strong interplay between experiment and theory, such molecular crystals as N_2 [1, 2], CO_2 [3, 4], CO [5, 6], NH_3 [7, 8], and benzene[9, 10], have been transformed into extended solids (covalent and ionic bonded networks) under high pressures. These studies have enhanced our understanding of chemical bonds under compression and provide opportunities to seek additional novel materials; however, it has been difficult to retain these remarkable structures at the ambient conditions needed for most applications[11]. For CO_2 , a 3D covalent network was synthesized[3] at high pressure (40 GPa) and temperature (1,800 K) that is isomorphic to the β -cristobalite phase of SiO_2 [12], with each carbon atom bonded tetrahedrally to four oxygen atoms. This phase of CO_2 was proposed to have potential applications as superhard (initial experiments estimated a bulk modulus of 365 GPa[13], but theory and experiment later found it to be 136 GPa[12, 14]), nonlinear optical, and high energy density material, so efforts were made to quench this phase down to 1 atm and 300 K[3]; however, it reverts back to the molecular phase at pressures lower than 1 GPa.

Since it is isoelectronic to CO_2 but polar, attempts were made to form an extended solid from N_2O using compression (above 20 GPa) and laser heating (above 1,000 K) in a diamond anvil[15]. However, instead it decomposed into a mixture of an ionic crystal NO^+NO_3^- and compressed N_2 molecules. No covalent extended framework similar to the polymeric CO_2 phase was found. Indeed, since the nitrogen atom forms one less covalent bond than carbon atom, it is not obvious that it would be possible to construct a dense extended solid phase of N_2O other than the ionic form. Even so, we decided to use first principle method to explore a large number of space groups and bonding

patterns at high pressures.

This chapter describes our work[16], in which we predict a one-dimensional all-nitrogen backbone polymer phase with two planar conformations for N₂O at high pressures, and determine the transition pressure of 60 GPa, above which the polymer phases are the most stable form. Furthermore, we find that upon relaxation to ambient conditions, both planar polymers relax to the same non-planar *trans*-polymer, and the predicted phonon spectrum and dissociation kinetics validate its stability.

4.1 Search for extended solid phases of N₂O under high pressures

Since we start with molecular crystals of NNO in which London dispersion attraction (van der Waals attraction) is dominant, we employed the PBE-*ulg* flavor of DFT (DFT-*ulg*) in which corrections accounting for London dispersion attractions are included[17]. PBE-*ulg* calculations were performed using VASP package[18–20], modified to describe PBE-*ulg* and using the PAW method[21] to account for core-valence interactions. The kinetic energy cutoff for plane wave expansions was set to 500 eV, and the reciprocal space was sampled by Γ -centered Monkhorst-Pack scheme[22] with a fine resolution of $2\pi \times 1/60 \text{ \AA}^{-1}$. The convergence criteria were set to 10^{-6} eV energy difference for solving for the electronic wavefunction, and 10^{-3} eV/ \AA force for geometry optimization.

We searched for high pressures structures with two independent strategies:

- (1) In the first, we started with 41 known AB₂-type crystal structures, replaced A with O and B with N, and used DFT to determine the optimum atom positions and packings using a fixed density of 3.915 g/cm³ (a relative compression of 0.384 and the same as polymeric CO₂ at 41 GPa[12]). Then we took the new configurations from the lowest energy structures, built appropriate extended cells, and refined further with DFT to obtain the optimum stacking.
- (2) In the second approach, we used the USPEX code[23–25] based on an evolutionary algorithm developed by Romanov, Glass, and Lyakhov[23] and featuring local optimization, real-space representation, and flexible physically motivated variation operators. Here we considered a 12-atom unit cell at 40, 60, and 80 GPa. Note that in the search of structures using USPEX, the kinetic energy cutoff was lowered to 400 eV, with reciprocal grids of $2\pi \times 0.06 \text{ \AA}^{-1}$. After locating the global minima, the above-mentioned finer computational settings were applied again to confirm the structures and energetics.

Both methods led to the same two final high pressure structures: both corresponding to a 1D N₂O polymer but with either *cis*- (Figure 4.1a) and *trans*- (Figure 4.1b) conformations (the *cis*-case is lower), predicted to be the most stable species above 60 GPa. The valence bond descriptions of these structures has an alternating N and N⁺ backbone polyacetylene-like zigzag chain with each N⁺

forming a covalent bond to O^- . The valence bond description would suggest alternating single and double bonds (1.448 Å and 1.309 Å), which we find for the *cis*-case; however, for the *trans*-case we find all NN bonds to have the same bonding distances (1.390 Å at 1 atm), indicating full resonance along the chain.

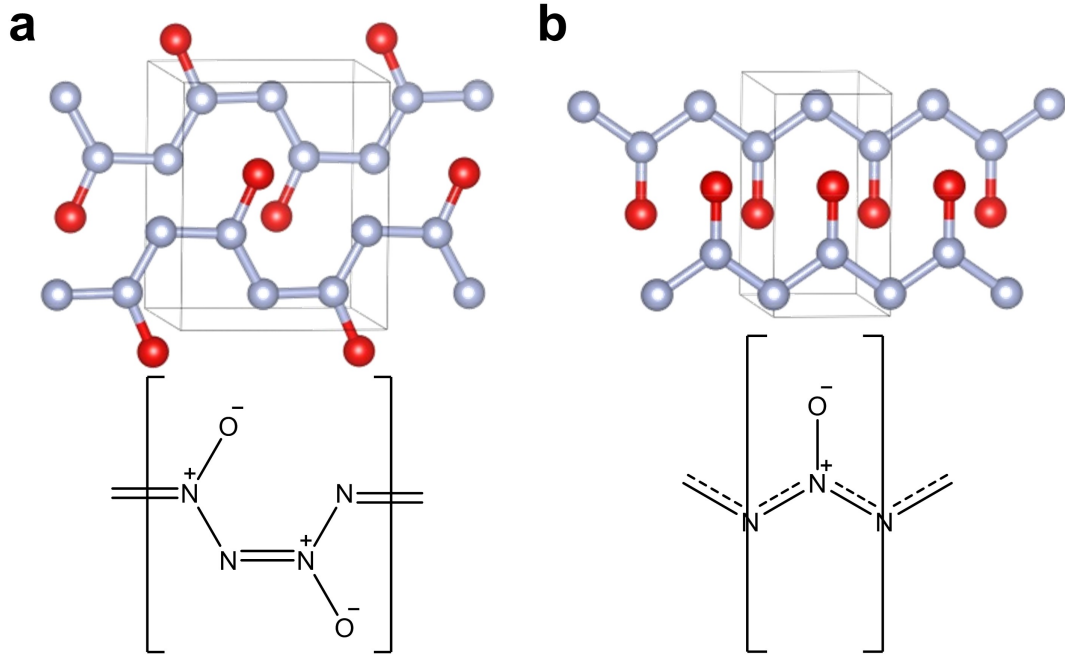


Figure 4.1. Illustration of crystal structures and chemical formulations of a single chain for (a) planar *cis*-polymer and (b) planar *trans*-polymer.

4.2 Transitions between molecular, ionic, and polymer phases of N_2O

Figure 4.2 shows the enthalpies of various relevant phases of N_2O as a function of pressure, taking the ground state molecular crystal with space group $Pa\bar{3}$ (α -nitrogen structure) as the reference. For the two molecular phases, $Pa\bar{3}$ and $Cmca$, experiments find head-to-tail orientation disorder[26], so we considered all possible conformations in the unit cell to determine the lowest energy. The calculated dependence of crystal volume on pressure is comparable with experiment (Figure 4.3), leading to a calculated transition pressure between the two molecular phases of 5.8 GPa at 0 K, compared to the experimental value of 4.8 GPa at room temperature[26]. Note that the deviation of 1 GPa is equivalent to an energy density of only 0.14 kcal/mol/Å³, and such small error is well within the accuracy limit of DFT methods.

In the range of 10 to 55 GPa and 1,000 to 3,400 K, the diamond anvil experiments on NNO

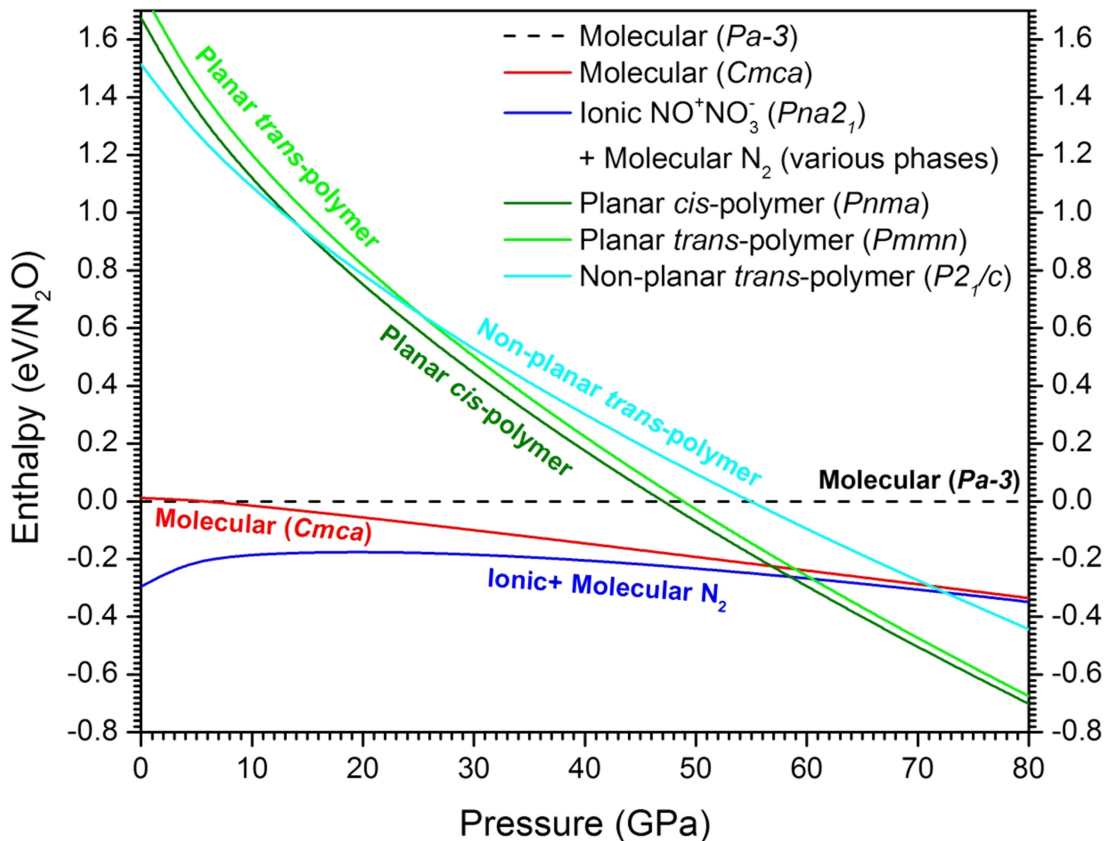


Figure 4.2. Ground state enthalpy as a function of pressure predicted for various phases of N_2O .

observed a mixture of the ionic NO^+NO_3^- phase in equilibrium with an N_2 molecule phase, formed from the dissociation of N_2O at high pressure and temperature[15, 29, 30]. We also calculated these phases at the pressures considered here. However, the structure of NO^+NO_3^- is not well-established experimentally: experiments reported the formation of monoclinic $P2_1/m$ phase ionic salt from the high-pressure (2 GPa) reaction of an N_2 and O_2 mixture[31], while the original experiments on dissociation of N_2O under laser heating in a diamond anvil found an orthorhombic phase related to the aragonite to form after cooling[15, 32]. Therefore, for the DFT study we constructed the NO^+NO_3^- crystal by cell relaxation starting with the aragonite structure. This led to a new orthorhombic $Pna2_1$ phase (see Figure 4.4), which we found to be 0.03 eV per formula more stable than the monoclinic phase. We carried out DFT calculations of N_2 molecular crystals, starting with the known phases (α , γ , ϵ , ζ) at low temperature[33], and at each pressure the energy calculated to be most stable was used in the enthalpy calculations. Surprisingly, this combination of NO^+NO_3^- and N_2 is more stable than the NNO molecular phases for all pressures down to 0 GPa. This is plausible, since the heat of formation of N_2O molecule is 82 kJ/mol above N_2 and O_2 , which were shown to

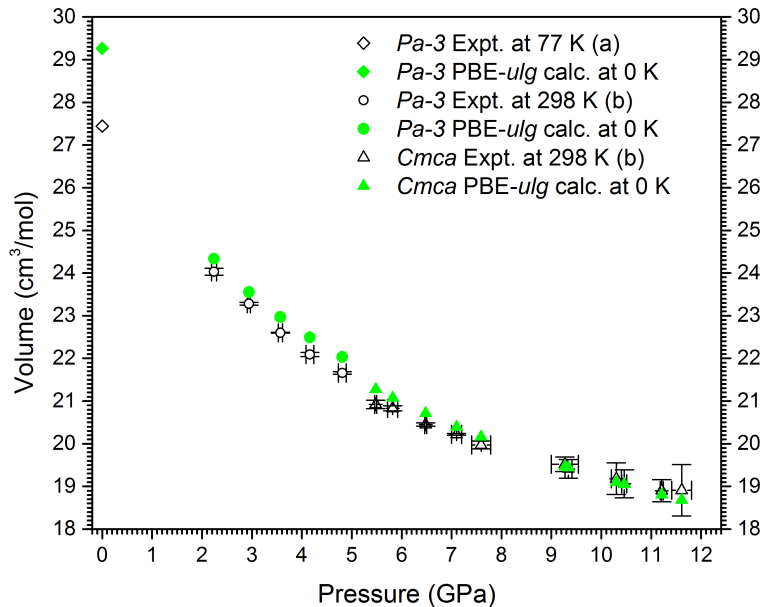


Figure 4.3. Comparison between PBE-*ulg* calculated (green filled symbols) and experimental ((a) Ref. [27]; (b) Ref. [26]) (black open symbols) EOSs for molecular phases of N_2O . Error bars are shown for all experimental data, and the agreement is excellent for high pressures (> 2 GPa), with the largest deviation of 1.8% for volume (0.6% for length dimension), which is most likely the limitation of parent PBE functional[28]. However, at low pressure of 1 atm (0.001 GPa), PBE-*ulg* gives overestimation of 6.6% for volume (2.2% for length dimension), which may be again originated from PBEs description of molecular bonding: for N_2O molecule, PBE gives N–N and N–O bond lengths of 1.143 Å and 1.198 Å, overestimated by 1.3% and 1.2% with respect to experimental data of 1.128 Å and 1.184 Å. This error gets amplified through dipole in evaluating volume of the molecular crystal. At high pressure, molecular crystals resemble more as extended solids, for which PBE is better from theoretical construction. Indeed, as shown in this figure, PBE-*ulg* calculated volume agrees better and better when pressure is increased.

form NO^+NO_3^- at 2 GPa using 10.2 keV synchrotron X-ray radiation[31].

Figure 4.2 shows that the *cis*- and *trans*- 1D polymeric phases remain energetically close (the *cis*-case more stable by 0.03 – 0.10 eV/molecular unit) and become more stable than both the molecular and the mixed ionic phases at pressures above 60 GPa. Including ZPE and entropy from phonons has marginal effect(see Figure 4.5):

- including ZPE to obtain the 0 K Gibbs free energies, we find that the critical pressure for the transition from the mixed ionic phase to the *cis*-polymer increases from 58.5 GPa to 61 GPa;
- while introducing both entropy and enthalpy corrections to 300 K leads to a further increase to 62 GPa at 300 K (64 GPa at 500 K).

Here, ZPE and thermal corrections were calculated with phonon DOS as implemented in the Phonopy code[34].

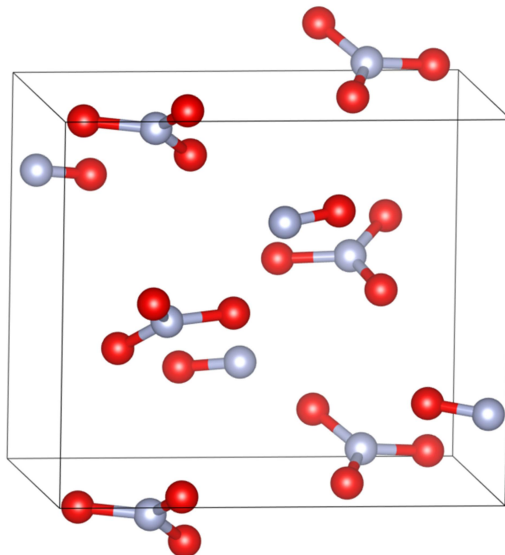


Figure 4.4. Illustration of the orthorhombic crystal structure of ionic NO^+NO_3^- with space group $Pna2_1$. The structure was derived from aragonite, with lower energy than the monoclinic $P2_1/m$ phase reported[31], and crystal structure coordinates can be found in the supplemental material of our paper[16].

The dominant factor in determining the enthalpy at high pressure is the compressibility. For the mixed phase the ionic NO^+NO_3^- component is a dense solid, but the global compressibility of the mixed phase is dominated by the molecular phase of N_2 (see Figure 4.A1), which polymerizes only above 110 GPa[2]. In contrast, the two new NNO polymeric phases each forms a pure extended solid with mixed covalent and ionic frameworks. Thus these phases dominate at high pressures (where the PV term in the enthalpy becomes dominant) over all the other phases of N_2O containing molecular forms.

The major difference between these *cis*- and *trans*- forms is that the planar *cis*-NNO polymer possesses alternating single and double bonds, as in polyenes (polyacetylene) with an even number of carbons, while the planar *trans*-conformation of NNO has equal NN bond lengths (strong resonance) along the chain, perhaps due to strong electrostatic repulsion between adjacent negatively-charged oxygen atoms.

4.3 Relaxation of polymer phases to ambient conditions

We further investigated the stability of the two NNO polymers by phonon analysis. Here, to obtain the phonon spectra, very tight convergence criteria were used, with 10^{-8} eV energy difference and 10^{-6} eV/Å force thresholds. To calculate force constants, we used the supercell approach with finite displacements, as implemented in the Phonopy code[34]. Indeed, for both crystals we find no

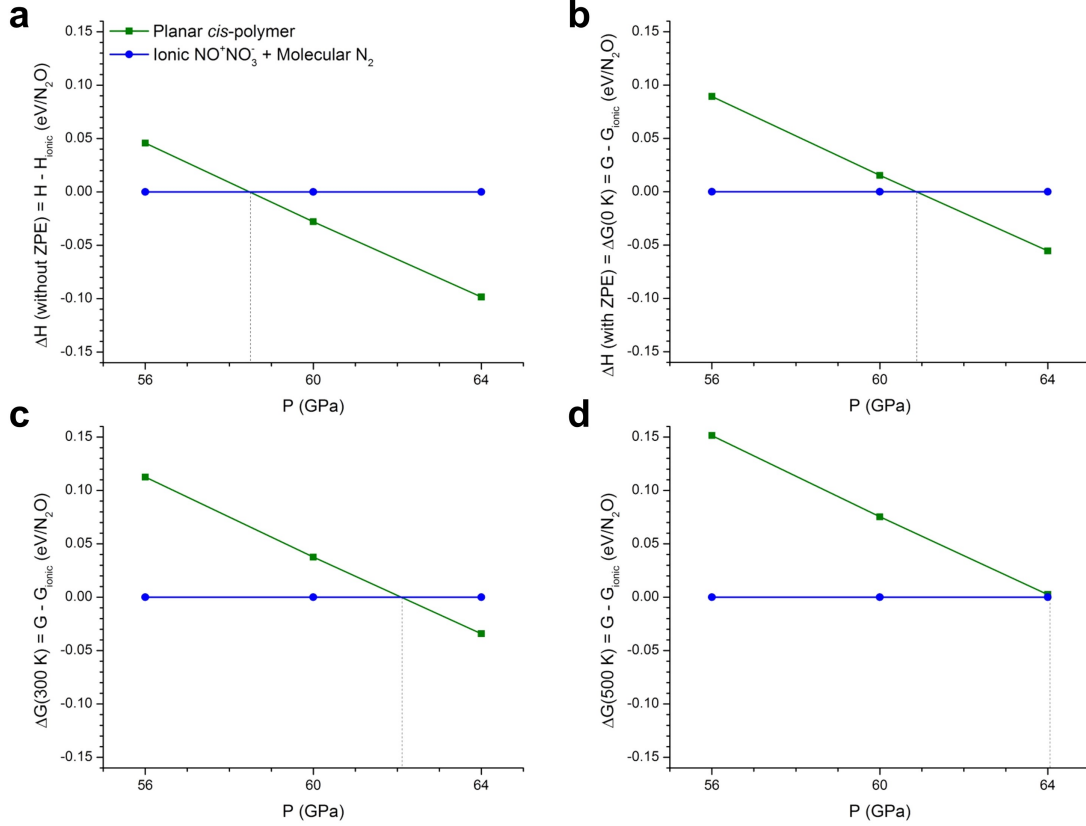


Figure 4.5. The effect of quantum ZPE and temperature (entropy) on the transition pressure to polymer phase P_c . (a) shows relative enthalpy ΔH (without ZPE) curves, which predict $P_c = 58.5$ GPa; (b) shows relative Gibbs free energy ΔG (at 0 K, i.e., no entropy contribution, but ZPE is included) curves, rendering $P_c = 61$ GPa; (c) shows relative Gibbs free energy ΔG (at 300 K) curves, increasing P_c to 62 GPa; (D) shows relative Gibbs free energy ΔG (at 500 K) curves, further boosting P_c to 64 GPa. Since including both ZPE and entropy at 300 K increases P_c by only 3.5 GPa, we consider that high temperature is not essential for these systems.

imaginary phonon modes under high pressures, as shown in the phonon spectra in Figure 4.6 (at 80 GPa), which confirms their existence as stable species (local minima). However, as the pressure is released, both crystals develop imaginary phonon modes at ~ 14 GPa, and both relax to one single non-planar *trans*-conformation (see Figure 4.7) at zero pressure, with a phonon spectrum that attests its stability. Under high pressures, the planar conformations with their higher compressibilities (see Figure 4.A1) are more stable but they lead to larger electrostatic repulsion between negatively-charged oxygen atom and lone-pair on nitrogen in the *cis*-case, and between adjacent negatively-charged oxygen atoms in the *trans*-case. It is the competition between compressibility and electrostatics which leads to the transition to the non-planar polymer at low pressure.

Besides accommodating electrostatics, the transition between planar and non-planar *trans*- conformations is also accompanied by an abrupt change from uniform bonding to alternating single and

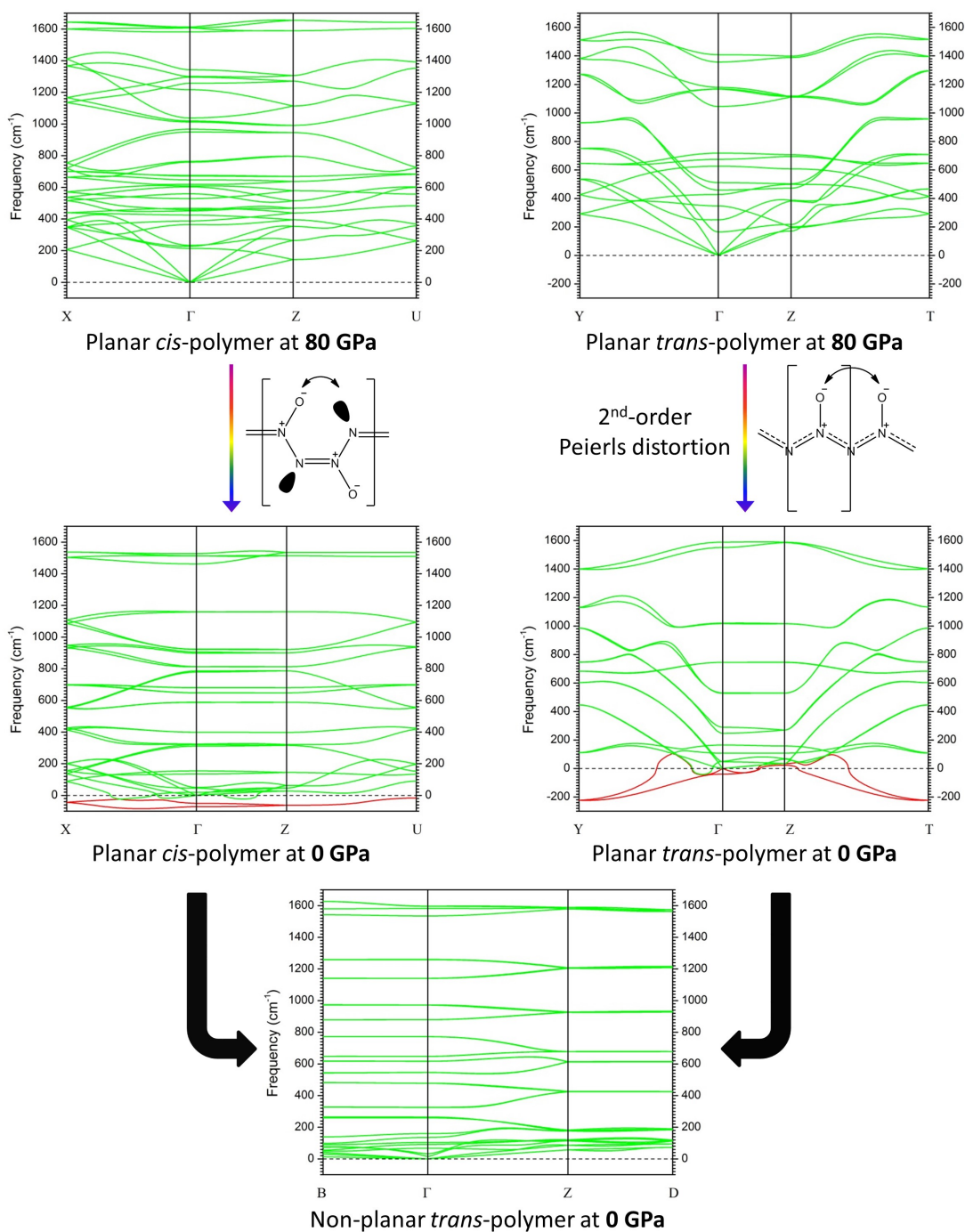


Figure 4.6. Phonon spectra for polymer phases of N_2O predicted at 80 and 0 GPa. Both planar *cis*- and *trans*-polymer phases develop imaginary phonon modes, due to electrostatic repulsions and/or second-order Peierls distortion, and transform into the same non-planar *trans*-polymer phase (see Figure 4.7), the phonon spectrum of which at 0 GPa shows no imaginary modes.

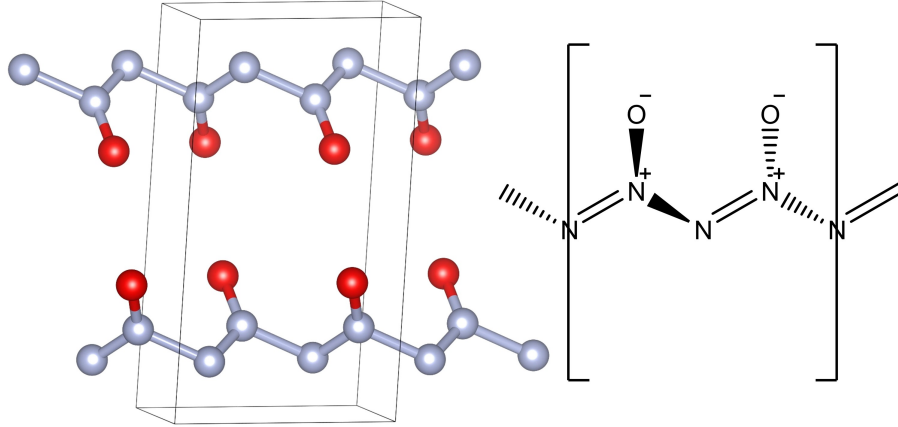


Figure 4.7. Illustration of crystal structure and chemical formulation of a single chain for non-planar *trans*-polymer.

double bonds, as shown in Figure 4.8, implying synergistic Peierls distortion, which is relevant to the electronic properties. Therefore, we calculated band gaps of all polymeric structures (optimized with PBE-*ulg* flavor of DFT) and plotted against pressures in Figure 4.8. Interestingly, PBE-*ulg* predicts that both planar NNO polymers are 1D metals, with transitions to insulators below 72 GPa for *cis*-polymer and 25 GPa for *trans*-polymer, the latter with simultaneous conformation transition from planar to non-planar. Figure 4.8 also shows the bond length differences between neighboring N–N bonds for the various phases. We find a trend from uniform bonding (exact for *trans*-polymer, quasi-uniform for *cis*-polymer with 0.03 Å difference) at high pressures to alternating single and double bonds when pressure is released. Combining this with the trend in band gaps indicates a first-order Peierls distortion, as in polyacetylene.

However, it is well documented (see Ch. 2 and references therein) that density functionals, such as PBE that are based only on LDA and GGA, significantly underestimate band gaps for insulators, due to intrinsic delocalization error from including the self-interaction in the Coulomb energy. To verify the metallic properties of these polymers under high pressures, we re-investigated all electronic structures with the hybrid functional B3PW91, which we showed to predict accurate band gaps for a wide range of semiconductors (see Ch. 2 and references therein). Here, B3PW91 calculations were conducted employing the CRYSTAL09 package[35], and 6-311G(*d*) triple-zeta quality basis sets for both nitrogen and oxygen[36]. Similar k-space grids and convergence criteria, as in fine calculations with VASP, were set for consistency. In contrast to PBE, B3PW91 predicts insulating states for all three polymers throughout the whole range of pressures considered, as shown in Figure 4.8. Here the DOS (Figure 4.9) shows that both planar *cis*- and *trans*-polymers at high pressures with (quasi-) uniform bonding are charge-transfer insulators, with the VBM dominated by $2p$ orbitals of the negatively charged oxygen and bridging nitrogen atoms, while the CBM dominated by $2p$

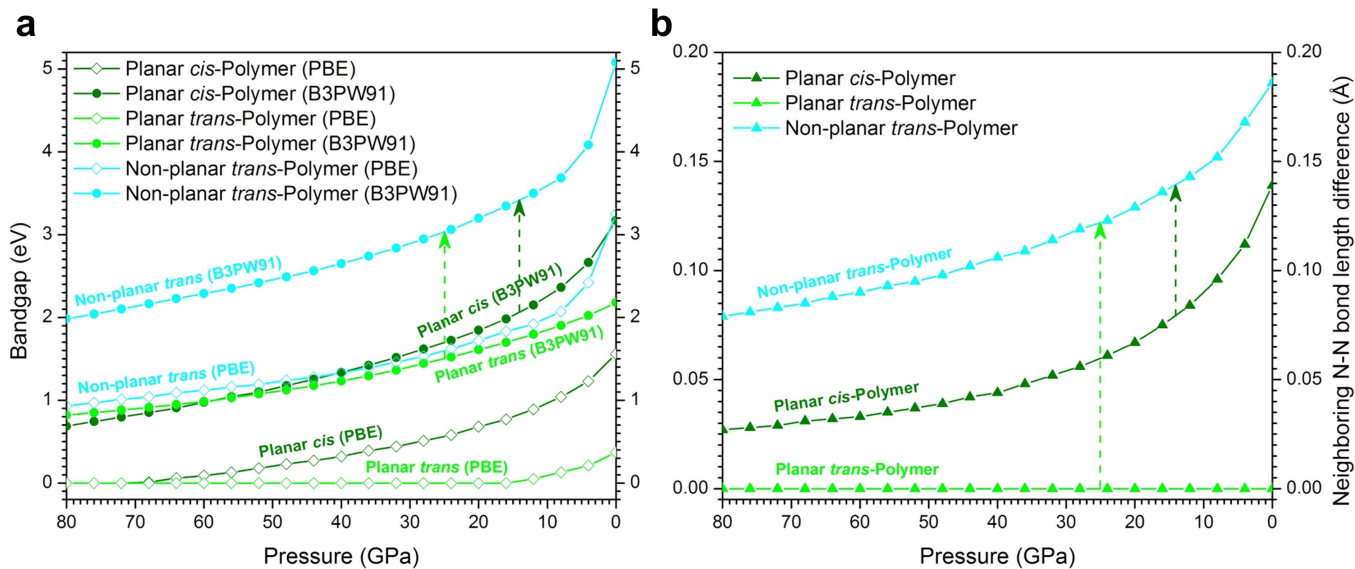


Figure 4.8. Band gap and neighboring N-N bond length difference predicted as functions of pressure for all three polymer phases of N_2O at ground states. The dashed lines with arrows indicate where the transition from planar to non-planar conformation happens.

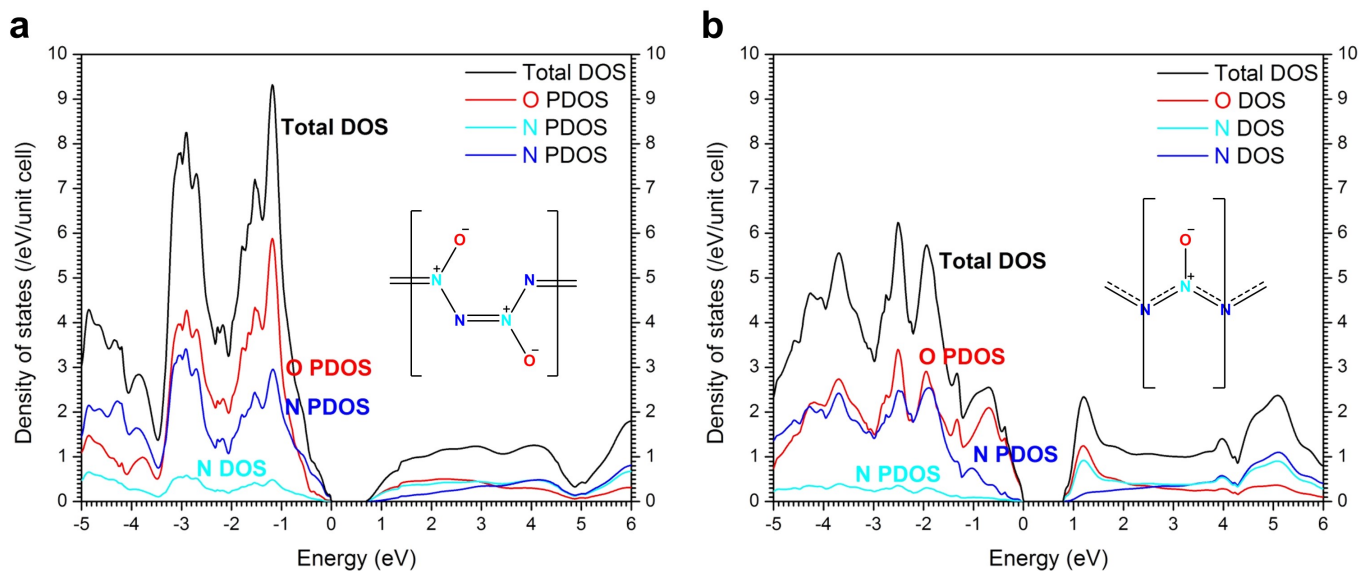


Figure 4.9. Total and partial electronic DOSs calculated with B3PW91 for planar *cis*-polymer (a) and planar *trans*-polymer (b) at 80 GPa. The different colors indicate atoms on which the total DOS is projected. The VBM is set as the zero energy reference.

orbitals of the positively charged nitrogen atom. Accordingly, B3PW91 results infer the transition to be second-order Peierls distortion, as in polyacene. At this point we cannot be sure whether to trust the B3PW91 or the PBE description, so it would be most valuable to carry out experiments

on the conductivity or electronic spectra of these new phases.

4.4 Kinetic stability of the non-planar N_2O polymer at ambient conditions

To further evaluate the stability of non-planar *trans*-polymer, we investigated the dissociation kinetics of the polymer, using DFT for a finite model oligomer containing 8 N_2O units and terminated with methyl groups at both ends. For finite model calculations, the geometry optimization, Hessian calculation, and TS search were carried out at UB3LYP/6-311G(*p,d*) level using Jaguar[37]. The Hessian was used to provide the vibrational frequencies for ZPE and thermo-corrections to enthalpy. The TS was shown to have exactly one imaginary vibrational mode by following the minimum energy path scan to connect reactant and product. Enthalpies are reported at 298.15 K and 1 atm.

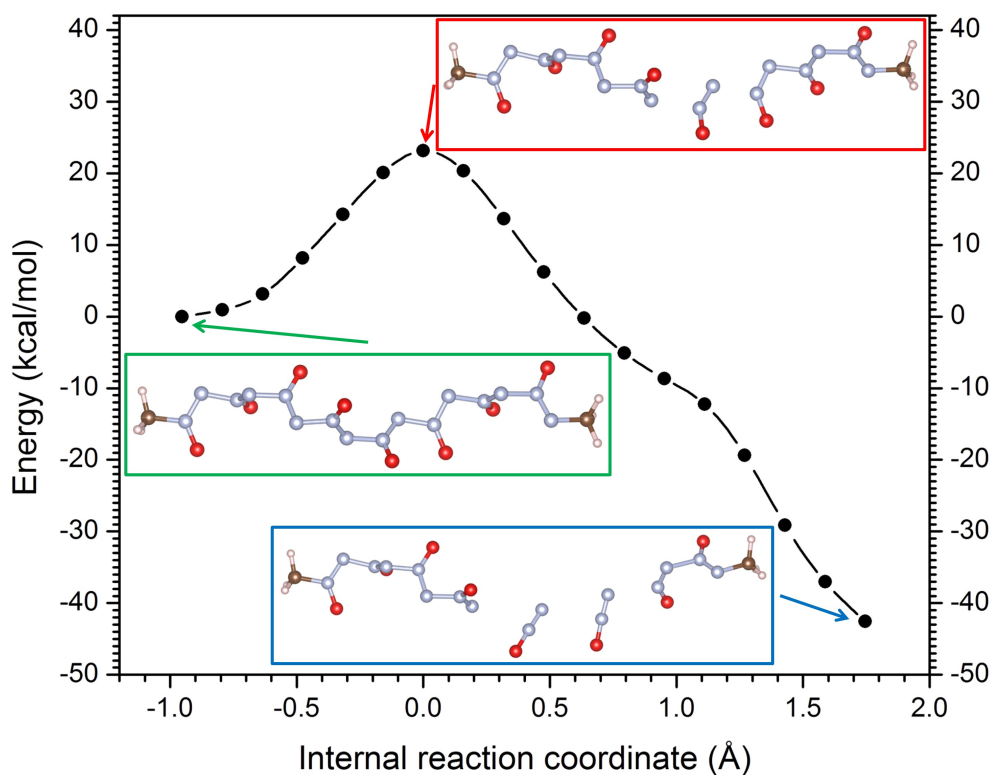


Figure 4.10. Reaction path calculated for dissociation of the model oligomer. The oligomer contains 8 N_2O units and is terminated with methyl groups at both ends.

We stretched this finite chain until it fractured, locating the TS shown in Figure 4.10. This leads to an activation energy of 20.6 kcal/mol. At the TS, the partially dissociated N_2O has N–N distances of 2.062 and 1.830 Å to its two neighbors, much longer than corresponding equilibrium

distances of 1.465 and 1.447 Å. This indicates that a large free space is required to activate the dissociation process, making the dissociation less favorable in the solid. This high activation barrier of 20.6 kcal/mol from the finite model corresponds to a surface energy of 1.56×10^3 erg/cm², considering the packing in the crystal. To rule out the effects of finite size and termination group, we also did a TS search with an isolated periodic infinite chain of the non-planar polymer using the CRYSTAL09 package (UB3LYP/6-311G(*d*)), and a barrier of 26.2 kcal/mol was found (see Figure 4.A2). Compared to the finite model, the slight overestimation might well reflect the constrained space and flexibility in conformation due to PBC. This thus confirms the validity of using a finite model previously, and we consider that it is likely that the non-planar *trans*-polymer of N₂O will be stable at 1 atm pressure and room temperature.

After passing the TS, the oligomer would start releasing N₂O one by one from each end, accompanied with significant heat release of 40.6 kcal/mol per N₂O molecule, which might lead to catastrophic decomposition. Thus the non-planar *trans*-NNO polymer is a high energy content structural material. Indeed, we calculated (PBE-*ulg*) the non-planar N₂O *trans*-polymer to provide an internal energy release of 3.5 kJ/g when dissociated into N₂ and O₂, which is comparable to the energy release of TNT (4.2 kJ/g). Thus non-planar *trans*-NNO is a potential high-energy oxidizer for new explosive composites and rocket propellants. Since the N₂O polymer chain is composed of alternating single and double bonds, similar to polyacetylene, albeit with an all nitrogen backbone, it might form the basis for a new type of conducting polymers, through appropriate doping or structure modification. Similarly we expect that it might have strong nonlinear polarizabilities for nonlinear optical applications.

4.5 Concluding remarks

Summarizing, we used DFT to predict that the NNO molecular crystal can be transformed into novel polymeric phases at high pressures (beyond decomposition into mixture phase of ionic compound NO⁺NO₃⁻ and N₂ gas previously observed in experiments). The two most stable 1D N₂O polymers with planar *cis*- and *trans*-conformations were identified to be energetically favorable at pressures above 60 GPa. More importantly, when the pressure is released, these polymers transform into the same non-planar *trans*-conformation, stable at ambient pressure and temperature. This was substantiated by analysis of the phonon spectrum and by calculating the dissociation kinetics. This new poly-NNO material might be an excellent high-energy oxidizer for a polymer composite in which nonpolar NNO forms the matrix.

The PBE calculations suggest metallic property in the high pressure polymer resulting from the strong resonance in these systems, which seems to disappear in the low pressure non-planar polymer due to changes in bonding, leading to Peierls distortion, together with electrostatic repulsions. Thus

with doping these NNO polymers, such as iodine, which works successfully in polyacetylene, may give rise to a new type of conducting polymer based on all-nitrogen chains. This whole work serves to illustrate the new *in silico* process of discovering new materials by theoretical modeling, particularly under extreme conditions.

Appendix

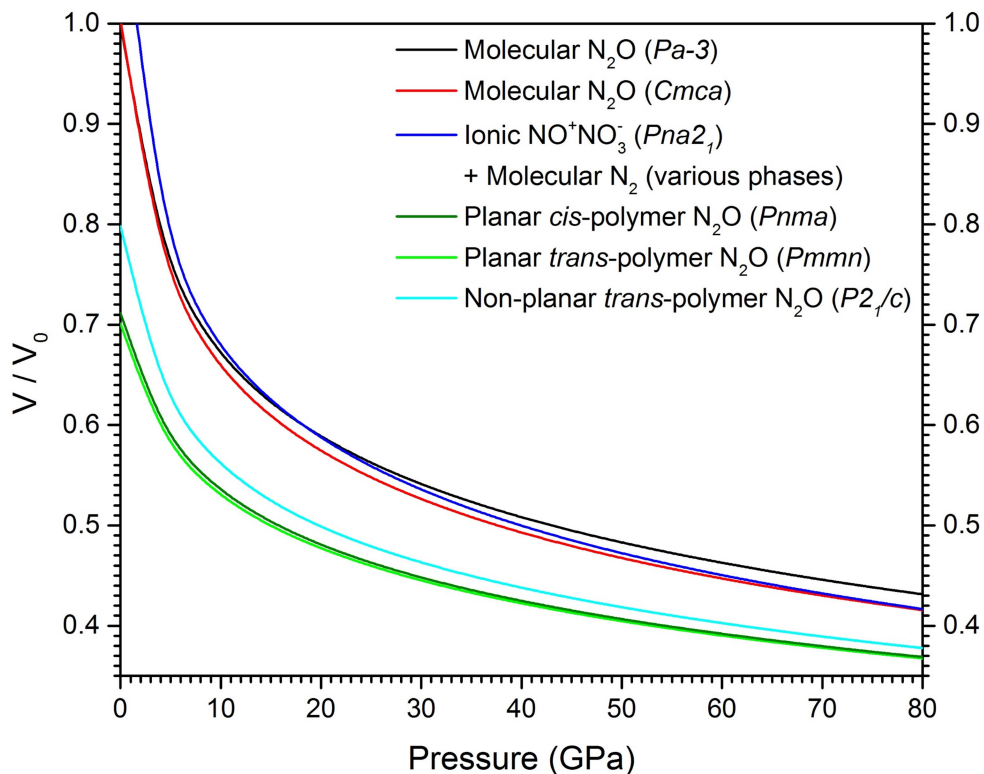


Figure 4.A1. EOSs for various phases of N_2O at ground states. The vertical axis is the compression ratio V/V_0 , where V is volume per N_2O formula, and V_0 is the molecular volume for the N_2O molecular crystal with space group $Pa\bar{3}$ at 0 GPa.

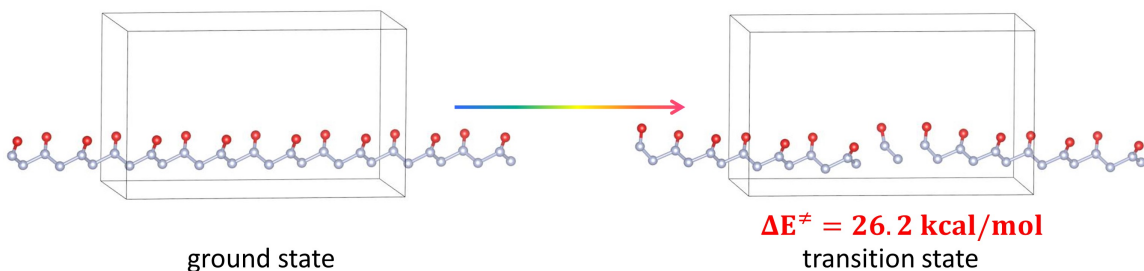


Figure 4.A2. TS calculated for dissociation of an isolated periodic infinite chain of the non-planar polymer. The unit cell contains 8 N_2O units.

The crystal structure for planar *cis*-NNO-polymer at 80 GPa predicted with PBE-*ulg*:

Space group: *Pnma*

Lattice parameters: $a = 3.864407 \text{ \AA}$, $b = 4.033027 \text{ \AA}$, $c = 4.600315 \text{ \AA}$

Fractional coordinates:

O	0.589619	0.750000	0.391888
O	0.410381	0.250000	0.608112
O	0.910381	0.250000	0.891888
O	0.089619	0.750000	0.108112
N	0.719392	0.750000	0.632071
N	0.280608	0.250000	0.367928
N	0.780608	0.250000	0.132072
N	0.219392	0.750000	0.867929
N	0.441423	0.250000	0.123597
N	0.558577	0.750000	0.876403
N	0.058577	0.750000	0.623597
N	0.941423	0.250000	0.376403

The crystal structure for planar *trans*-NNO-polymer at 80 GPa predicted with PBE-*ulg*:

Space group: *Pmmn*

Lattice parameters: $a = 4.094183 \text{ \AA}$, $b = 2.144710 \text{ \AA}$, $c = 4.067528 \text{ \AA}$

Fractional coordinates:

O	0.000000	0.500000	0.414855
O	0.500000	0.000000	0.585145
N	0.000000	0.000000	0.897919
N	0.500000	0.500000	0.102081
N	0.000000	0.500000	0.714772
N	0.500000	0.000000	0.285228

The crystal structure for non-planar *trans*-NNO-polymer at 0 GPa predicted with PBE-*ulg*:

Space group: $P2_1/c$

Lattice parameters: $a = 7.585837 \text{ \AA}$, $b = 4.914450 \text{ \AA}$, $c = 4.170160 \text{ \AA}$, $\beta = 93.748215^\circ$

Fractional coordinates:

O	0.655520	0.501835	0.264942
O	0.344479	0.498165	0.735058
O	0.344480	0.001835	0.235058
O	0.655520	0.998165	0.764942
N	0.772618	0.665839	0.336789
N	0.227382	0.334161	0.663211
N	0.227382	0.165839	0.163211
N	0.772618	0.834161	0.836789
N	0.146663	0.160657	0.832386
N	0.853337	0.839343	0.167614
N	0.853337	0.660657	0.667614
N	0.146663	0.339343	0.332386

The more stable orthorhombic crystal structure of ionic NO^+NO_3^- at 0 GPa predicted with PBE-*ulg*:

Space group: *Pna2₁*

Lattice parameters: $a = 6.360302 \text{ \AA}$, $b = 8.019972 \text{ \AA}$, $c = 6.956295 \text{ \AA}$

Fractional coordinates:

N	0.813720	0.518406	0.712900
N	0.813720	0.981594	0.212900
N	0.239097	0.765869	0.051196
N	0.239097	0.734131	0.551196
N	0.739097	0.234131	0.948804
N	0.739097	0.265869	0.448804

N	0.313720	0.481594	0.287100
N	0.313720	0.018406	0.787100
O	0.184014	0.578418	0.537912
O	0.184014	0.921582	0.037912
O	0.747319	0.852605	0.233251
O	0.747319	0.647395	0.733251
O	0.247319	0.147395	0.766749
O	0.247319	0.352605	0.266749
O	0.684014	0.421582	0.462088
O	0.684014	0.078418	0.962088
O	0.608756	0.171732	0.362572
O	0.608756	0.328268	0.862572
O	0.407093	0.784885	0.484298
O	0.407093	0.715115	0.984298
O	0.907094	0.215115	0.515702
O	0.907094	0.284885	0.015702
O	0.108757	0.828268	0.637428
O	0.108757	0.671732	0.137428

References

- [1] Mailhiot, C, Yang, L. H, & McMahan, A. K. (1992) Polymeric nitrogen. *Phys. Rev. B* **46**, 14419–14435.
- [2] Eremets, M. I, Gavriluk, A. G, Trojan, I. A, Dzivenko, D. A, & Boehler, R. (2004) Single-bonded cubic form of nitrogen. *Nature Mater.* **3**, 558–563.
- [3] Iota, V, Yoo, C. S, & Cynn, H. (1999) Quartzlike carbon dioxide: An optically nonlinear extended solid at high pressures and temperatures. *Science* **283**, 1510–1513.
- [4] Serra, S, Cavazzoni, C, Chiarotti, G. L, Scandolo, S, & Tosatti, E. (1999) Pressure-induced solid carbonates from molecular CO₂ by computer simulation. *Science* **284**, 788–790.
- [5] Bernard, S, Chiarotti, G. L, Scandolo, S, & Tosatti, E. (1998) Decomposition and polymerization of solid carbon monoxide under pressure. *Phys. Rev. Lett.* **81**, 2092–2095.
- [6] Lipp, M. J, Evans, W. J, Baer, B. J, & Yoo, C. S. (2005) High-energy-density extended CO solid. *Nature Mater.* **4**, 211–215.
- [7] Pickard, C. J & Needs, R. J. (2008) Highly compressed ammonia forms an ionic crystal. *Nature Mater.* **7**, 775–779.
- [8] Ninet, S, Datchi, F, & Saitta, A. M. (2012) Proton disorder and superionicity in hot dense ammonia ice. *Phys. Rev. Lett.* **108**.
- [9] Ciabini, L, Santoro, M, Gorelli, F. A, Bini, R, Schettino, V, & Raugei, S. (2007) Triggering dynamics of the high-pressure benzene amorphization. *Nature Mater.* **6**, 39–43.

- [10] Wen, X. D, Hoffmann, R, & Ashcroft, N. W. (2011) Benzene under high pressure: a story of molecular crystals transforming to saturated networks, with a possible intermediate metallic phase. *J. Am. Chem. Soc.* **133**, 9023–9035.
- [11] McMillan, P. F. (2002) New materials from high-pressure experiments. *Nature Mater.* **1**, 19–25.
- [12] Datchi, F, Mallick, B, Salamat, A, & Ninet, S. (2012) Structure of polymeric carbon dioxide CO₂-V. *Phys. Rev. Lett.* **108**, 125701.
- [13] Yoo, C. S, Cynn, H, Gygi, F, Galli, G, Iota, V, Nicol, M, Carlson, S, Hausermann, D, & Mailhot, C. (1999) Crystal structure of carbon dioxide at high pressure: “superhard” polymeric carbon dioxide. *Phys. Rev. Lett.* **83**, 5527–5530.
- [14] Dong, J. J, Tomfohr, J. K, Sankey, O. F, Leinenweber, K, Somayazulu, M, & McMillan, P. F. (2000) Investigation of hardness in tetrahedrally bonded nonmolecular CO₂ solids by density-functional theory. *Phys. Rev. B* **62**, 14685–14689.
- [15] Somayazulu, M, Madduri, A, Goncharov, A. F, Tschauner, O, McMillan, P. F, Mao, H. K, & Hemley, R. J. (2001) Novel broken symmetry phase from N₂O at high pressures and high temperatures. *Phys. Rev. Lett.* **87**, 135504.
- [16] Xiao, H, An, Q, Goddard, W. A, Liu, W.-G, & Zybin, S. V. (2013) Formation of the –N(NO)N(NO)– polymer at high pressure and stabilization at ambient conditions. *Proc. Natl. Acad. Sci. U.S.A.* **110**, 5321–5325.
- [17] Kim, H, Choi, J. M, & Goddard, W. A. (2012) Universal correction of density functional theory to include London dispersion (up to Lr, element 103). *J. Phys. Chem. Lett.* **3**, 360–363.
- [18] Kresse, G & Hafner, J. (1993) Ab initio molecular dynamics for liquid metals. *Phys. Rev. B* **47**, 558–561.
- [19] Kresse, G & Furthmuller, J. (1996) Efficiency of ab-initio total energy calculations for metals and semiconductors using a plane-wave basis set. *Comput. Mater. Sci.* **6**, 15–50.
- [20] Kresse, G & Furthmuller, J. (1996) Efficient iterative schemes for ab initio total-energy calculations using a plane-wave basis set. *Phys. Rev. B* **54**, 11169–11186.
- [21] Kresse, G & Joubert, D. (1999) From ultrasoft pseudopotentials to the projector augmented-wave method. *Phys. Rev. B* **59**, 1758–1775.
- [22] Monkhorst, H. J & Pack, J. D. (1976) Special points for Brillouin-zone integrations. *Phys. Rev. B* **13**, 5188–5192.

- [23] Oganov, A. R & Glass, C. W. (2006) Crystal structure prediction using ab initio evolutionary techniques: Principles and applications. *J. Chem. Phys.* **124**, 244704.
- [24] Glass, C. W, Oganov, A. R, & Hansen, N. (2006) USPEX – evolutionary crystal structure prediction. *Comput. Phys. Commun.* **175**, 713–720.
- [25] Lyakhov, A. O, Oganov, A. R, & Valle, M. (2010) How to predict very large and complex crystal structures. *Comput. Phys. Commun.* **181**, 1623–1632.
- [26] Mills, R. L, Olinger, B, Cromer, D. T, & Lesar, R. (1991) Crystal-structures of N₂O to 12 GPa by X-ray-diffraction. *J. Chem. Phys.* **95**, 5392–5398.
- [27] Hamilton, W. C & Petrie, M. (1961) Confirmation of disorder in solid nitrous oxide by neutron dffraction. *J. Phys. Chem.* **65**, 1453–1454.
- [28] Perdew, J. P, Ruzsinszky, A, Csonka, G. I, Vydrov, O. A, Scuseria, G. E, Constantin, L. A, Zhou, X, & Burke, K. (2008) Restoring the density-gradient expansion for exchange in solids and surfaces. *Phys. Rev. Lett.* **100**, 136406. erratum. (2009) **102**, 039902.
- [29] Yoo, C. S, Iota, V, Cynn, H, Nicol, M, Park, J. H, Le Bihan, T, & Mezouar, M. (2003) Disproportionation and other transformations of N₂O at high pressures and temperatures to lower energy, denser phases. *J. Phys. Chem. B* **107**, 5922–5925.
- [30] Iota, V, Park, J. H, & Yoo, C. S. (2004) Phase diagram of nitrous oxide: Analogy with carbon dioxide. *Phys. Rev. B* **69**, 064106.
- [31] Meng, Y, Von Dreele, R. B, Toby, B. H, Chow, P, Hu, M. Y, Shen, G. Y, & Mao, H. K. (2006) Hard X-ray radiation induced dissociation of N₂ and O₂ molecules and the formation of ionic nitrogen oxide phases under pressure. *Phys. Rev. B* **74**, 214107.
- [32] Song, Y, Somayazulu, M, Mao, H. K, Hemley, R. J, & Herschbach, D. R. (2003) High-pressure structure and equation of state study of nitrosonium nitrate from synchrotron X-ray diffraction. *J. Chem. Phys.* **118**, 8350–8356.
- [33] Katzke, H & Toledano, P. (2008) Theoretical description of pressure- and temperature-induced structural phase transition mechanisms of nitrogen. *Phys. Rev. B* **78**, 064103.
- [34] Togo, A, Oba, F, & Tanaka, I. (2008) First-principles calculations of the ferroelastic transition between rutile-type and CaCl₂-type SiO₂ at high pressures. *Phys. Rev. B* **78**, 134106.
- [35] Dovesi, R, Saunders, V. R, Roetti, C, Orlando, R, Zicovich-Wilson, C. M, Pascale, F, Civalleri, B, Doll, K, Harrison, N. M, Bush, I. J, DArco, P, & Llunell, M. (2009) *CRYSTAL 2009 User's Manual*. (University of Torino, Torino).

- [36] Krishnan, R, Binkley, J. S, Seeger, R, & Pople, J. A. (1980) Self-consistent molecular orbital methods. XX. A basis set for correlated wave functions. *J. Chem. Phys.* **72**, 650–654.
- [37] Bochevarov, A. D, Harder, E, Hughes, T. F, Greenwood, J. R, Braden, D. A, Philipp, D. M, Rinaldo, D, Halls, M. D, Zhang, J, & Friesner, R. A. (2013) Jaguar: A high-performance quantum chemistry software program with strengths in life and materials sciences. *Int. J. Quantum Chem.* **113**, 2110–2142.

Chapter 5

Development of ECP for eFF to extend application to high- Z elements

The contents presented in this chapter are based on [H. Xiao](#)¹, A. Jaramillo-Botero¹, P. L. Theofanis and W. A. Goddard, III, *submitted*, 2014.

The BO approximation, which decouples the nuclear and electronic motions, constitutes one of the fundamental assumptions for most atomistic modeling techniques, ranging from first principle electronic structure methods, such as HF and DFT for accurate description of PESs, to force field methods that enable MD simulations of large scale systems through classical approximations of PES. However, the BO approximation breaks down for systems in extreme conditions where the electronic portion of the wavefunction contains contributions from many stationary states[1], such as those found at extremes of temperature, shock, and radiation etc., which cause irreversible material transformations, fatigue, embrittlement, and ultimately failure.

Several methods have been developed to describe the coupling of nuclear and electronic motions, including surface hopping schemes[2] which rely on PES generated by high level *ab initio* methods, Ehrenfest dynamics with TDHF/TDDFT engines[3, 4], and fermionic dynamics[5, 6] approaches. All these techniques are computationally expensive and impractical for performing long time scale dynamics of large scale non-adiabatic materials phenomena.

The eFF method[7] was developed to overcome this limitation (see Figure 5.1) and recent improvements to it[1] confirm its scalability and applicability to challenging problems including, but not limited to: explaining electronic phenomena during brittle fracture of silicon[8], understanding the mechanisms of Auger induced chemical decomposition[9], characterizing hydrostatic and dynamic shock Hugoniot for different materials[1, 7, 10, 11], and tracking the dynamics of Coulomb explosion in silicon and diamond nanoparticles[12], among others[13].

¹These authors contributed equally to this work.

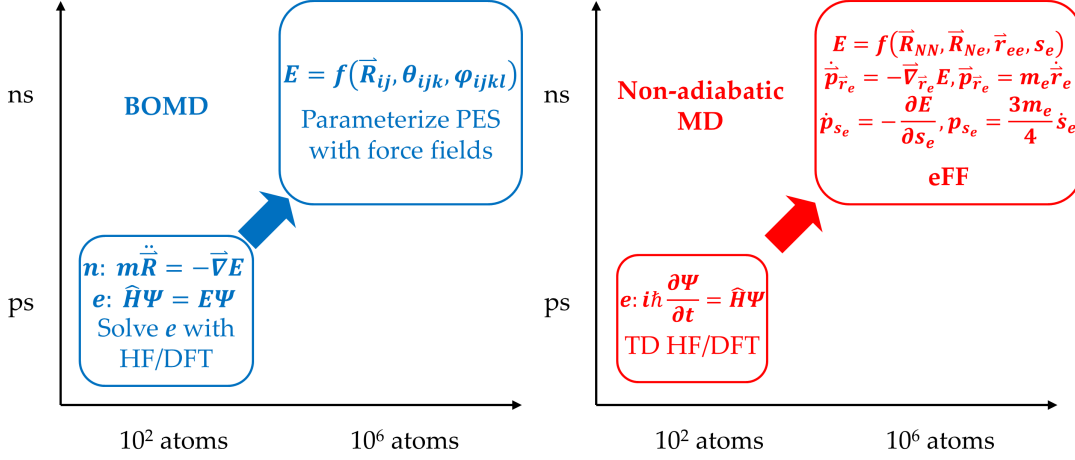


Figure 5.1. eFF aims at long term and large scale non-adiabatic MD simulations in which the electronic wavefunction positions and sizes vary dynamically.

Here, we present a formal extension to support high- Z elements in eFF using ECPs, and their validation on C, O, Si, and Al based systems (energetics and geometries) using QM.

In the framework of eFF, nuclei are classical point charges and the total electronic wavefunction is represented by a Hartree product of one-electron FSG wave packets, (5.1), whose positions, \vec{x}_i , and sizes, s_i , are both dynamic variables.

$$\Psi(\vec{r}_i) \propto \prod_i \exp \left[- \left(\frac{1}{s_i^2} - \frac{2p_{s_i}}{s_i} \frac{i}{\hbar} \right) (\vec{r}_i - \vec{x}_i)^2 \right] \exp \left[\frac{i}{\hbar} \vec{p}_{\vec{x}_i} \cdot \vec{r}_i \right] \quad (5.1)$$

This representation leads to a rather simple electronic energy expression, $\langle \Psi | \hat{H} | \Psi \rangle$, consisting of the sum of single-particle kinetic energies and pairwise Coulomb energies. Additionally, pairwise spin-dependent Pauli corrections are introduced to locally compensate for the lack of explicit wavefunction anti-symmetrization. As a result, the electronic contribution to the total energy is evaluated as in classical force field methods. Furthermore, semi-classical EOM for propagating the electronic wavefunction, as shown in Figure 5.1, are derived from the time dependent Schrödinger equation with a local harmonic potential approximation. The combination of force-field-like energy evaluation and semi-classical EOM in eFF enables long term and large scale non-adiabatic MD simulations of low- Z systems, as demonstrated in previous work[1].

However, an intrinsic limitation of the all-electron FSG-based eFF described above emanates from the spherical symmetry of the underlying basis functions. For atoms with valence electrons of higher angular momenta, such as p -block elements, the FSG representation misses part of the interaction between the core and valence electrons, due to the absence of explicit nodal structures.

In this chapter, we present in Sec. 5.1 one approach to mitigate this problem, in the form of ECP. This model form of ECP replaces the interaction between the core and the valence electrons with a potential energy given by their overlap. The corresponding parameters that define the ECP are obtained from first-principles QM. In Sec. 5.2, we show that the resulting ECP formulation appropriately captures part of the missing p -character of FSG valence electrons, which leads to a correct description of complex bonding structures (e.g., multiple bonds and lone pairs) for systems containing p -block elements of the second and third row of the periodic table. In particular, we demonstrate parameters for silicon, aluminum, carbon, oxygen, and binary combination SiC, and example applications using the open source implementation[1] available in the parallel molecular dynamics simulator LAMMPS[14].

5.1 Formulation of ECP models in eFF

The full eFF Hamiltonian, shown in (5.2), has a standard description for electrostatic interactions between a set of 0D points and Gaussian charges which include, nucleus-nucleus (E_{NN}), electron-electron (E_{ee}), and nucleus-electron (E_{Ne}). In addition to the electrostatics, eFF introduces quantum effects through an electron kinetic energy from the Gaussian (E_{KE}) and a spin-dependent Pauli repulsion potential term (E_{PR}) between Gaussians (further details can be found in previous work[1, 7]).

$$U(R, r, s, \sigma) = E_{NN}(R_{NN}) + E_{Ne}(R_{Ne}, s) + E_{ee}(r_{ee}, s) + E_{KE}(s) + E_{PR}(\sigma, s) \quad (5.2)$$

where R_{NN} , R_{Ne} , and r_{ee} correspond to the inter-nucleus, nucleus-electron, and inter-electron distances, respectively, s to the electron radius, and σ to the electron spin.

The eFF-ECP scheme presented here requires reformulating and parameterizing the Pauli energy term, E_{PR} , for pseudo particles with Gaussian charge replacing the core electrons and the nucleus, and adjusting the classical electrostatic energies between the pseudo-core and valence electrons (*core-elec*), nuclei (*core-nuc*), and other pseudo-core (*core-core*) particles as,

$$\begin{aligned} E_{core-elec} &= \sum_{i,j} \frac{Z_i Z_j}{R_{ij}} \text{Erf} \left(\frac{\sqrt{2} R_{ij}}{\sqrt{s_{core,i}^2 + s_{elec,j}^2}} \right), \\ E_{core-nuc} &= \sum_{i,j} \frac{Z_i Z_j}{R_{ij}} \text{Erf} \left(\frac{\sqrt{2} R_{ij}}{\sqrt{s_{core,j}^2}} \right), \\ E_{core-core} &= \sum_{i < j} \frac{Z_i Z_j}{R_{ij}} \text{Erf} \left(\frac{\sqrt{2} R_{ij}}{\sqrt{s_{core,i}^2 + s_{core,j}^2}} \right) \end{aligned} \quad (5.3)$$

where Z is the particle charge.

The new Pauli potentials in this model ECP representation are designed, according to the relation $E_{PR} \propto S^2$, where S is the overlap between two Gaussians, one representing the core and the other an interacting valence electron. By choice, two different types of overlaps are defined in this ECP representation as:

1. an s - s overlap, for an s -type valence electron, and
2. an s - p overlap, for an p -type valence electron.

The corresponding functional forms are derived as,

$$E_{PR_{s-s}} = \mathbf{a} \exp\left(-\frac{\mathbf{b}r^2}{\mathbf{c} + s^2}\right) \quad (5.4)$$

$$E_{PR_{s-p}} = \mathbf{a} \left(\frac{2}{\mathbf{b}/s + s/\mathbf{b}}\right)^5 (r - \mathbf{c}s)^2 \exp\left(-\frac{\mathbf{d}(r - \mathbf{c}s)^2}{\mathbf{e} + s^2}\right) \quad (5.5)$$

where r in (5.4) is the distance between the s -type pseudo-core and an interacting s -type valence electron, and in (5.5) it corresponds to the distance between the s -type pseudo-core and the s -type Gaussian representing one of the lobes of a p -type valence electron (see Figure 5.2). s is the size of the corresponding valence electron, \mathbf{a} corresponds to the pseudo-core wave function amplitude, \mathbf{b} in (5.4) and \mathbf{d} in (5.5) to the pseudo-core wavefunction decay factor, \mathbf{c} in (5.4) and \mathbf{e} in (5.5) to the square of effective pseudo-core particle size (not to be confused with the core size used in Coulomb energies, in (5.3), which is also a parameter). For the s - p case \mathbf{c} corresponds to an off-center measure and \mathbf{b} to a second effective size that adjusts the overlap amplitude.

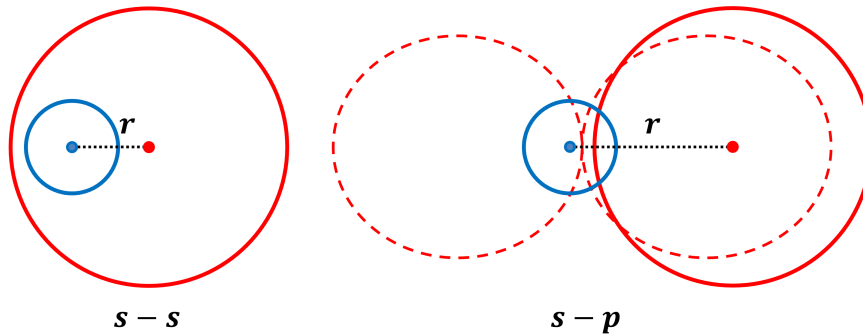


Figure 5.2. Illustration of distances used in the two functional types of ECP, where blue circles represent core electrons and red valence electrons. Note that the center of real p -type Gaussian is the nodal point.

(5.4) and (5.5) are derived from the square of the overlap between spherical Gaussians used in

eFF,

$$\phi_i(\vec{r}) = \left(\frac{\sqrt{2}}{\sqrt{\pi}s_i} \right)^{3/2} \exp \left[-\frac{(\vec{r} - \vec{r}_i)^2}{s_i^2} \right] \quad (5.6)$$

neglecting phase factors associated with dynamics (one Gaussian representing a valence electron and the other an atom's core set of electrons), with index $i = 1, 2$ for core and valence electrons, respectively.

The square of overlap between s -type core and s -type valence is given by

$$S^2 = \left(\frac{2}{s_1/s_2 + s_2/s_1} \right)^3 \exp \left[-\frac{2r_{12}^2}{s_1^2 + s_2^2} \right] \quad (5.7)$$

For a p -type Gaussian representing the valence electron,

$$\phi_2(\vec{r}) = \left(\frac{\sqrt{2}}{\sqrt{\pi}s_i} \right)^{3/2} \frac{2}{s_2} (\vec{r} - \vec{r}_2) \exp \left[-\frac{(\vec{r} - \vec{r}_2)^2}{s_2^2} \right] \quad (5.8)$$

the square of overlap between s -type core and p -type valence is given by

$$S^2 = \left(\frac{2}{s_1/s_2 + s_2/s_1} \right)^5 \frac{r_{12}^2}{s_1^2} \exp \left[-\frac{2r_{12}^2}{s_1^2 + s_2^2} \right] \quad (5.9)$$

In order to preserve the simple form of the semi-classical EOM in eFF, a spherical Gaussian is used to represent one of the two lobes of the p -type valence electron. Therefore, the center of an s -type valence electron is that of the spherical Gaussian, while that of a p -type valence electron, which is the nodal point, and its offset is determined by $s_2/\sqrt{2}$, with the reasonable assumption that the center of spherical Gaussian is at exactly the cusp of the lobe. So, (5.9) is recast into

$$S^2 = \left(\frac{2}{s_1/s_2 + s_2/s_1} \right)^5 \frac{(r_{12} - s_2/\sqrt{2})^2}{s_1^2} \exp \left[-\frac{2(r_{12} - s_2/\sqrt{2})^2}{s_1^2 + s_2^2} \right] \quad (5.10)$$

Following the design of $E_{PR} \propto S^2$, two types of ECP formulation can be constructed:

$$E_{PR_{s-s}} = a \left(\frac{2}{s_1/s_2 + s_2/s_1} \right)^3 \exp \left[-\frac{2r_{12}^2}{s_1^2 + s_2^2} \right] \quad (5.11)$$

$$E_{PR_{s-p}} = a \left(\frac{2}{s_1/s_2 + s_2/s_1} \right)^5 \frac{(r_{12} - s_2/\sqrt{2})^2}{s_1^2} \exp \left[-\frac{2(r_{12} - s_2/\sqrt{2})^2}{s_1^2 + s_2^2} \right] \quad (5.12)$$

(5.4) and (5.5) are directly obtained from (5.11) and (5.12), respectively, by defining and replacing with the corresponding parameter variables.

In Sec. 5.2, we present optimized eFF-ECP parameters for aluminum (s - s), silicon (s - s), carbon (s - p), and oxygen (s - p) and validate them on example applications. All parameters were optimized

against diverse training sets of geometries and energetics obtained from QM calculations of small representative molecules. A two-step parameter optimization scheme was used, consisting of:

- (1) a GA based search to determine the most probable global basin, and
- (2) a local conjugate gradient based optimization within the local search space of the GA-determined basin in order to remove any randomness in the solution.

The GA was configured with tournament selection and uniform mutation over the predefined range for each parameter and evaluation was done via a fitness function of geometric and energetic RMSDs from the QM reference set. Further details on the parameter optimization framework can be found in Ref. [15].

5.2 Performance of optimized eFF-ECP parameters

Table 5.1 summarizes the eFF-ECP parameters for Al, Si, C, and O. Al and Si can be accurately described using the s - s ECP form in (5.4), i.e., $E_{PR_{s-s}}$, while C and O require the higher-order s - p form in (5.5), i.e., $E_{PR_{s-p}}$, due to their more complex and dominant p -type interactions, including multiple bonds and lone pairs.

The core radii were initially estimated by calculating the sizes of corresponding all-electron ions (i.e., Al^{3+} , Si^{4+} , C^{4+} , and O^{6+}) with the all-electron eFF, and then optimized to fit the correct electrostatics in the ECP description. In total, 4 parameters were optimized for the corresponding s - s ECP cases, and 6 for the corresponding s - p cases.

Table 5.1. eFF-ECP parameters optimized for a few 2^{nd} and 3^{rd} row p -block elements.

	Element	a	b	c	d	e	s_{core} (Bohr)
<hr/>							
s - s (Eq. (5.4))							
	Al	0.486000	1.049000	0.207000			1.660000
	Si	0.320852	2.283269	0.814857			1.691398
<hr/>							
s - p (Eq. (5.5))							
	C	22.721015	0.728733	1.103199	17.695345	6.693621	0.621427
	O	25.080199	0.331574	1.276183	12.910142	3.189333	0.167813
<hr/>							

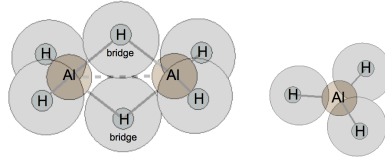
Hybrid (binary, tertiary, etc.) systems may be modeled using the parameters above, nonetheless, increased accuracy may be achieved by re-optimizing these parameters with QM cases that include all expected interactions. This will be exemplified here for silicon carbide.

5.2.1 Al and Si with s - s ECP

The effective core in Al is defined as a pseudo particle with wave-like properties, consisting of a nucleus and ten fixed electrons corresponding to the $1s^2 2s^2 2p^6$ configuration. This effective core plus three explicit valence electrons ($3s^2 3p^1$) completes the 4-particle eFF-ECP model representation of Al.

ECP parameters for Al were determined from ground state fcc bulk Al, lattice parameters and bulk modulus experimental values ($a_{\text{exp}} = 4.05 \text{ \AA}$ and $B_{\text{exp}} = 76 \text{ GPa}$), and finite aluminum hydride molecules, including those compared in Table 5.2. The resulting eFF-ECP lattice parameters and bulk modulus are $a_{\text{eFF-ECP}} = 4.05 \text{ \AA}$ and $B_{\text{eFF-ECP}} = 108 \text{ GPa}$, in contrast to the all-electron eFF values of $a_{\text{eFF}} = 4.23 \text{ \AA}$ and $B_{\text{eFF}} = 44 \text{ GPa}$. Emergent properties validated for Al include the aluminum hydride cluster bond energies as a function of cluster size as shown in Figure 5.3.

Table 5.2. Comparison of eFF-ECP, all electron eFF and DFT calculations on aluminum hydrides. The bond lengths d are in pm, bond angles θ in degree, bond energy E in kcal/mol.



Feature	Al_2H_6			AlH_3		
	B3LYP/M06	eFF-ECP	eFF	B3LYP/M06	eFF-ECP	eFF
$d_{\text{Al-Al}}$	258.3/261.382	267.142	220.0			
$d_{\text{Al-H}}$	157.7/157.3	148.241	159.7	158.4/158.1	151.932	160.4
$d_{\text{Al-H}_{\text{bridge}}}$	174.5,170.9/174.4,174.2	178.306	161.6			
$\theta_{\text{Al-Al-H}_{\text{bridge}}}$	42.105,41.051/41.386,41.441	41.486	47.111			
$\theta_{\text{H-Al-H}}$	127.493/128.168	128.647	116.71	120.0	120.0	120.0
$\theta_{\text{H-Al-H}_{\text{bridge}}}$	109.3/109.042	108.94	110.858			
$E_{\text{Al}_2\text{H}_6 \rightarrow 2\text{AlH}_3}$	32.74698/34.72389	33.3571	133.8163			

The effective core in Si has the same composition as the pseudo-core particle for Al, yet with four explicit valence electrons corresponding to the $3s^2 3p^2$ orbitals complete its 5-particle eFF-ECP model representation. The ECP parameters for Si were determined from first principle calculations on small silicon hydride motifs, including $\text{SiH}_3\text{-H}$ and $\text{H}_3\text{Si-SiH}_3$ energies, Si-H and Si-Si bond lengths, bulk lattice constant, and bond dissociation energies for several silicon and silicon hydride compounds (as described in Ref. [8]).

The Si eFF-ECP parameters were validated on emergent material properties, such as IP, Si_2H_6 rotational barriers, bulk modulus, and yield strength, and used to describe the non-adiabatic quantum dynamics during brittle fracture in silicon crystal in previous work[8]. The Si eFF-ECP simulations

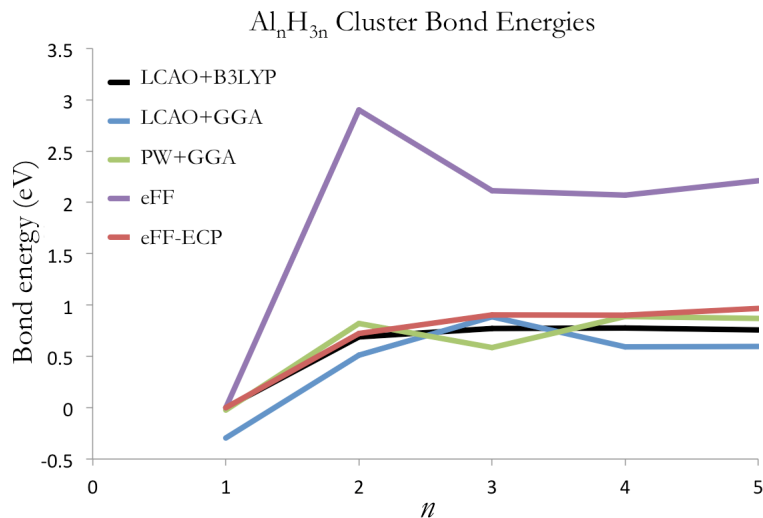


Figure 5.3. Comparison of cluster bond energies for different Al_nH_{3n} clusters. QM data from Ref. [16]

reproduce the correct response of the crack tip velocity to the threshold critical energy release rate (see Figure 5.4), a feat that is inaccessible to QM methods or conventional force-field-based MD, and describe the crack induced voltages, current bursts, and charge carrier production observed experimentally during fracture. This led to an explanation of how strain-induced surface rearrangements and local heating cause ionization of electrons at the fracture surfaces.

Our simulations reveal both local field-induced ionization and thermal ionization as a direct result of fracture, which leads to crack induced voltages across the fractured surfaces. We find that electron ionization is precipitated by the passing of the crack front (Figure 5.5a). Ionized electrons are excited by 5 eV, making them sufficiently energetic to escape the Si-surface barrier (Figure 5.5b). The initial excitation promotes the electrons to unbound states, but they subsequently relax to 4.1 eV above the ground state, well into the Si conduction band. An increase in potential energy causes ionization, primarily via heterolytic bond cleavage across the crack. In rare instances a heterolytic cleavage creates an anion on one crack face and a cation on the other crack face. As dangling bonds form 2×1 surface dimers, the excess electron causes Pauli exclusion clashes with adjacent surface pairs (Figure 5.5c) and the ionized electron's radius decreases to reduce its overlap with nearby same-spin electrons (Figure 5.5d). The spin clashing forces the electron further from the surface and the electron delocalizes (Figure 5.5e). Ultimately it relaxes and settles into the conduction band. $80 \pm 10\%$ of ionized electrons are ionized because of local field effects.

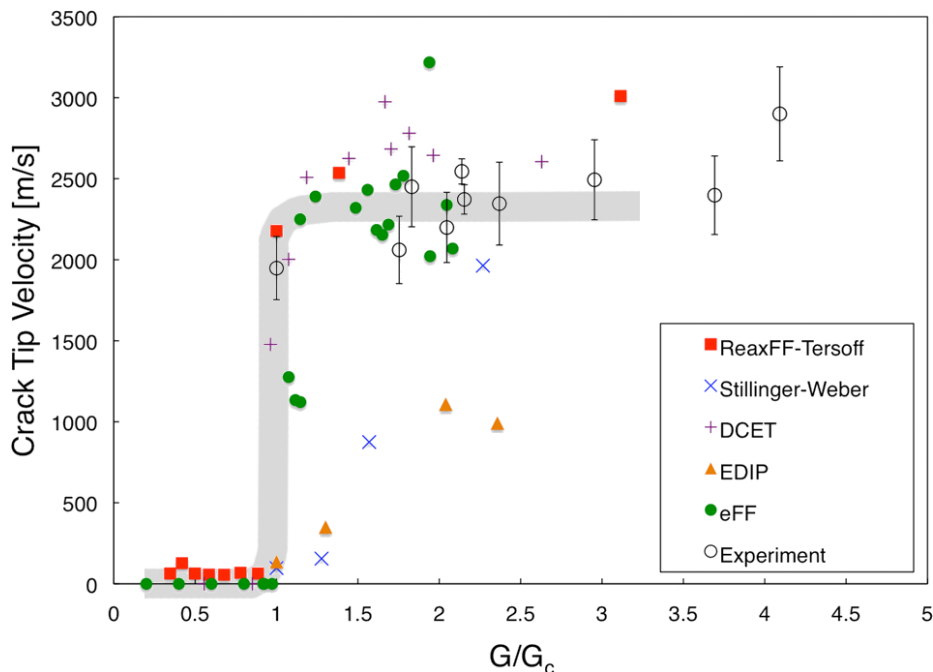


Figure 5.4. Crack tip velocity versus reduced load (normalized by the Griffith critical load value) for $\{111\}$ fracture from eFF-ECP, compared to experimental, ReaxFF+Tersoff simulations, and DCET and EDIP data. The grey line is a visual guide. From Ref. [8].

5.2.2 C with s - p ECP

The all-electron eFF formulation performs well in describing saturated hydrocarbons[11], yet it is inaccurate for unsaturated systems and fails at describing complex bonding structures, including multiple bonds and lone pairs, among others. Here we demonstrate the use of the $E_{PR_{s-p}}$ eFF-ECP (5.5) to overcome these issues, for the most part caused by increasingly non-spherical character in electrons.

In preparing the carbon eFF-ECP parameters, we set out to retain the all-electron eFF performance for saturated hydrocarbons, improve the bonding energy of C–C, and enable complex bonding descriptions. To this end, the prepared ECP training set includes geometries for CH_4 , C_2H_6 , $\text{CH}_2(\text{CH}_3)_2$, $\text{CH}(\text{CH}_3)_3$, C_2H_4 , C_2H_2 , and $\text{C}(\text{CH}_3)_4$, as well as the bonding energy of C–C in C_2H_6 . Table 5.3 includes the comparison of optimized results from eFF-ECP with the all-electron eFF representation and experiments.

In general, eFF-ECP improves the dependence of C–C and C–H bond lengths on the size of saturated hydrocarbons. The all-electron eFF predicts a large increase in both bond lengths as the hydrocarbon size increases, while eFF-ECP captures the correct trend. The $\sim 10\%$ reduction in the C–C bond length for bulk diamond is one example that confirms this (i.e., it is not part of the training set). On the other hand, the overestimation of C–C bonding energy in ethane is corrected,

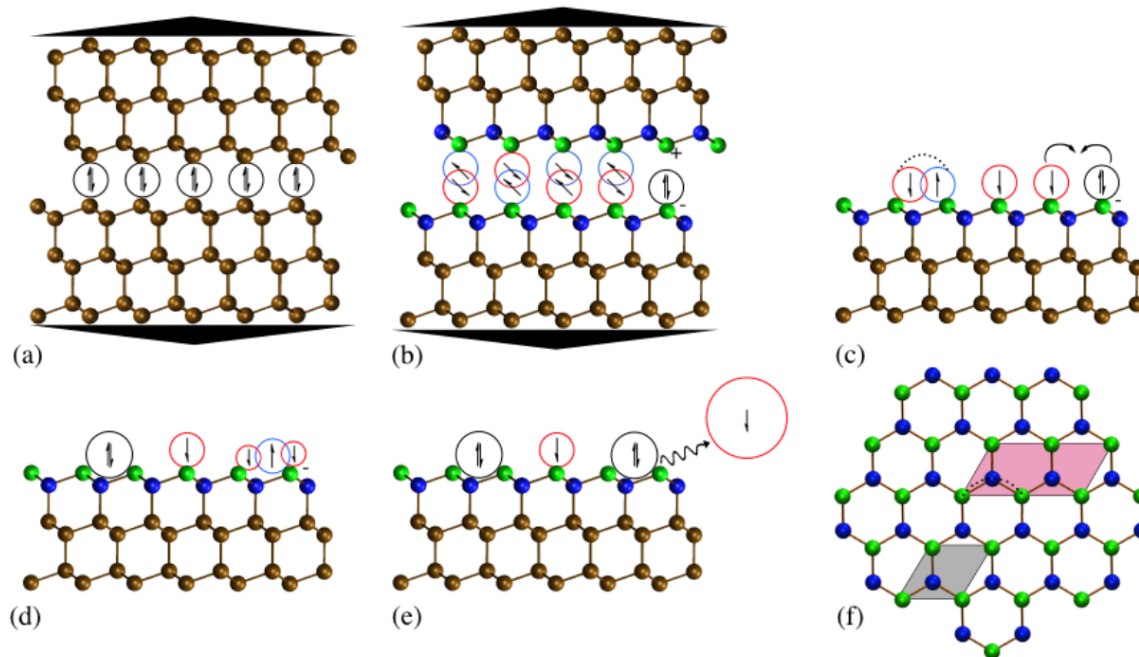


Figure 5.5. Mechanism of local field-induced ionization. (a) High strain rate cracking of Si leads to (b) surface electron ionization, (c) spin exchange, (d) increased electronic wavefunction kinetic energy for neighboring same-spin electrons, (e) and spin-clashing of surface electrons during 2×1 surface dimer reconstruction, which leads to the electron emissions observed experimentally.

from 163.5 kcal/mol in the all-electron eFF to an experimentally accurate value of 89.7 kcal/mol in eFF-ECP.

Table 5.3. Comparison of eFF-ECP and eFF on geometries of carbon-containing molecular and bulk systems.

Species	d_{CC} (pm)			d_{CH} (pm)			Θ (degree)		
	exact	eFF-ECP	eFF	exact	eFF-ECP	eFF	exact	eFF-ECP	eFF
CH ₄				109.4	105.6	114.3	109.5	109.5	109.5
C ₂ H ₆	153.6	152.0	150.1	109.1	106.5	117.3	110.9	111.3	110.8
CH ₂ (CH ₃) ₂	152.6	152.6	151.3	109.6	107.6	122.9	109.5	110.6	107.9
CH(CH ₃) ₃	152.5	153.0	152.9	110.8	108.7	142.4	109.4	109.9	101.8
C(CH ₃) ₄	153.4	153.2	157.3	111.4	106.7	117.8			
H ₂ C=CH ₂	133.9	137.7	151.7	108.6	97.2	108.9			
HC≡CH	120.3	115.4	138.3	106.3	91.8	105.2			
Diamond	154.5	155.1	168.1						

eFF-ECP now describes both single and multiple hydrocarbon bonds in a consistent manner,

i.e., the bond length decreases as the bond order increases. eFF-ECP also improves the stability of multiple bonds. For example, the hydrogenation energy of a double bond in ethene (not in the training set) is predicted to be exactly the same as the experimental value of 38.2 kcal/mol, while the all-electron eFF value results in 141.6 kcal/mol. Furthermore, rather than the non-planar diradical conformation given by all-electron eFF, eFF-ECP predicts the correct planar conformation for benzene molecule, although with alternating single and double bonds, which is inevitable from the localized nature of eFF framework.

Figure 5.6 shows a few molecules with conjugate double bonds, all of which are described with correct conformation by eFF-ECP. A more challenging system is the graphite bulk structure, which involves capturing the correct London dispersion energies. eFF-ECP predicts surprisingly good lattice parameters, with $a = 2.550 \text{ \AA}$ and $c = 6.943 \text{ \AA}$ (vs. the experimental value of $a = 2.461 \text{ \AA}$ and $c = 6.708 \text{ \AA}$). An interesting side effect is that the subtle London dispersion energies that stabilize graphite layers along the c axis is reasonably well captured with the eFF-ECP framework, while conventional DFT fails to capture this (without explicit dispersion corrections), as shown in Figure 5.7.

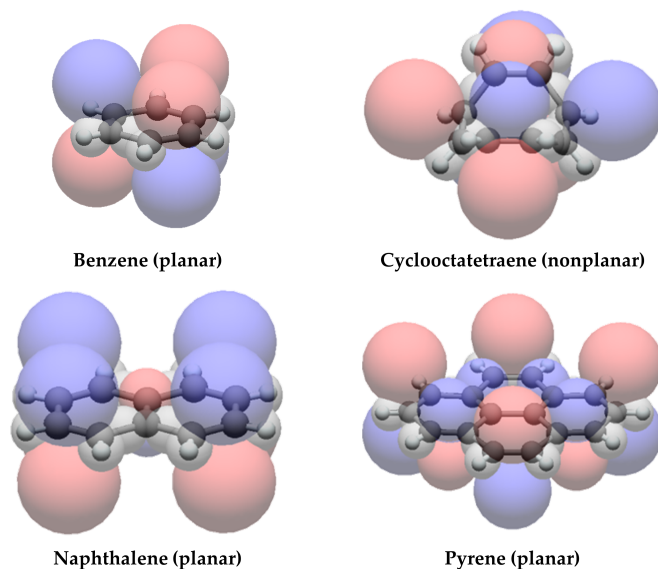


Figure 5.6. Gallery of molecules with conjugate double bonds. eFF-ECP is able to predict correct conformations for all of them. The red/blue colors stand for electronic spin up or down, respectively.

To test the non-adiabatic dynamics modeling capabilities of the C ECP, we applied it to study and understand the effect of induced energy excitations on the valence electrons of C–H bonds of a passivation layer in a diamond film and in the presence of atomic hydrogen gas, the idea being that surface selective chemistry may be achieved via excitation energy transfer from external sources, for example, an electron beam from an electron stimulated desorption (ESD) apparatus, onto resonant

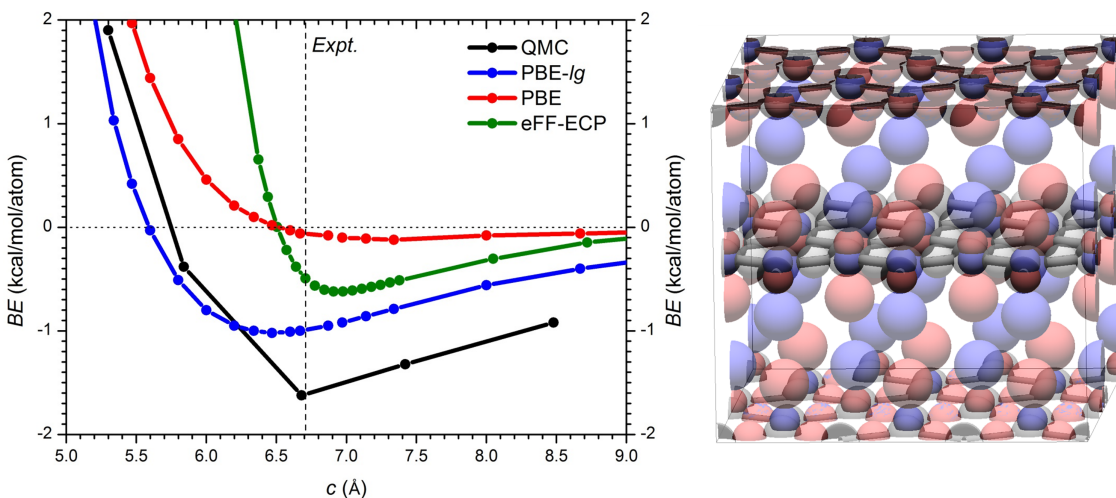


Figure 5.7. Comparison of various methods, including quantum Monte Carlo (QMC)[17] and dispersion-corrected PBE-*lg*[18], on the binding curve along the dispersion c axis of graphite.

modes on the material surface (in the case reported here, the valence electrons that participate in the C–H surface bonds). A 2×1 dimerized and H-capped diamond surface model slab was prepared and equilibrated to a temperature of 373 K, and subsequently combined with an atomic H gas equilibrated to 15,000 K in a single non-equilibrium NVE ensemble run (constant number of particles, volume and energy). Two separate systems were run concurrently, one in which the surface electrons were manually excited by a step-function of 5eV at $t = 0$ (i.e., the electron radii were reduced from 1.65 to 1.43 Bohr, which is equivalent to an electronic wavefunction kinetic energy input slightly below diamond’s bandgap energy) and one in which no manual excitation was introduced on the surface bonds. For the system that was manually excited, etching events were observed within 80 femtoseconds, while the un-excited systems ran for more than 1 picosecond without any hydrogen etching events. The enhanced hydrogen abstraction mechanism involves insertion and mobility of surface hydrogen between neighboring dimers, and subsequent recombination into an H_2 molecule (shown graphically in Figure 5.8.)

5.2.3 Oxygen with s - p ECP

One of the prominent features characterizing the chemistry of oxygen is the presence of lone pairs on it while bonding. These have a predominant p -character, and all-electron eFF fails in describing such systems, qualitatively and quantitatively. For example, the all-electron eFF predicts the water molecule to be linear, instead of bent. With the s - p ECP type, eFF-ECP is shown to handle lone pairs smoothly. Interestingly, the lone pair is represented by an open shell like configuration, i.e.,

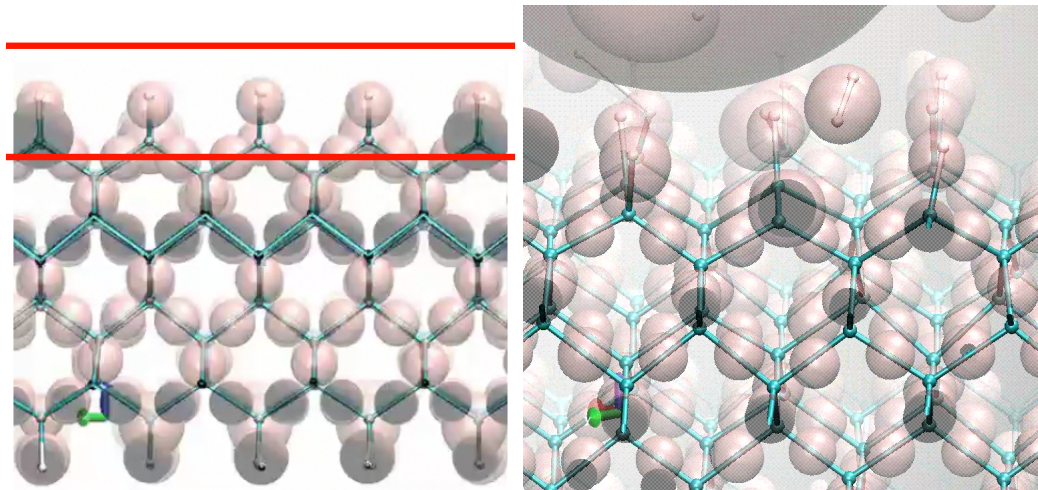


Figure 5.8. (left) Valence bond electrons (marked within a red box) in C-H surface excited with a step function of 5 eV, and (right) Femtosecond electronic excitation-induced desorption of hydrogen from a passivated diamond slab; a hydrogen molecule is ejected after 80 femtoseconds from surface dimer site (top-right side of surface). Electrons are shown as pink transparent spheres of different sizes (including ionized electrons in large spheres).

the size of electron with one spin being larger than that of electron with the other spin, as show in Figure 5.9, illustrated with water molecule.

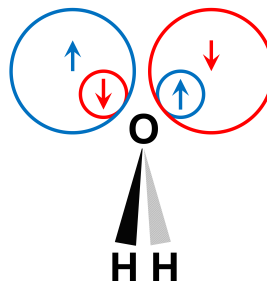
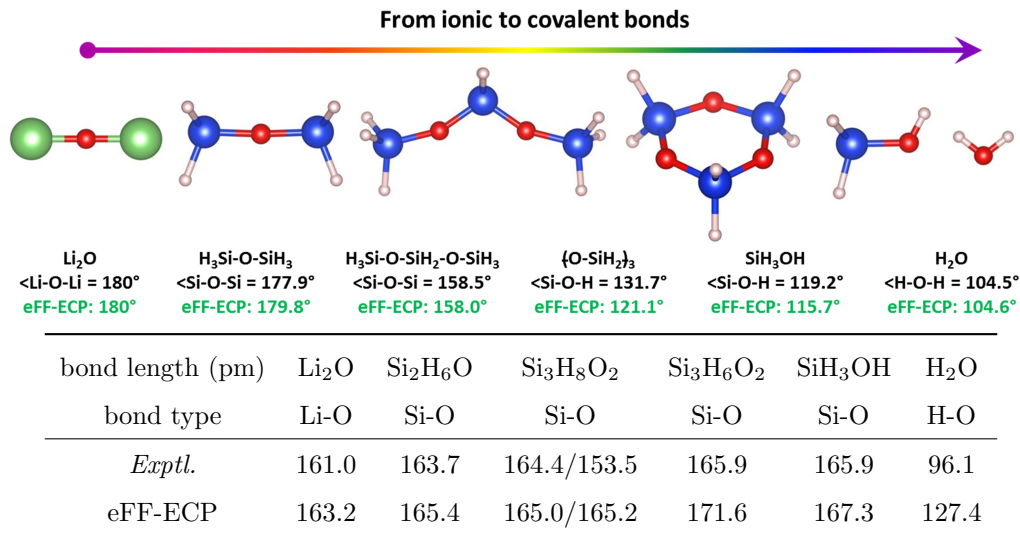


Figure 5.9. Open shell like representation of lone pairs in eFF-ECP, taking water molecule as an illustration.

The training set for O ECP includes Li_2O , $\text{Si}_2\text{H}_6\text{O}$, $\text{Si}_3\text{H}_8\text{O}_2$, $\text{Si}_3\text{H}_6\text{O}_2$, SiH_3OH , and H_2O , covering a variety of bonding characters, reflected by the various oxygen-centered angles (see Table 5.4). This is because, in addition to describing lone pairs, we wanted eFF-ECP to describe the subtle coupling between interacting lone pairs and bonding character. We validate that when oxygen atoms form purely ionic bonds, such as in Li_2O , the electrostatic repulsion between two cations dominates, leading to a linear molecular conformation; while as the degree of covalent bonding increases, the repulsion between lone pairs and bonding electrons becomes more dominant, leading to more bent molecular conformations, such as H_2O . Table 5.4 lists the comparison of optimized geometries

Table 5.4. Performance of eFF-ECP on geometries of various molecules with oxygen atom(s).



from eFF-ECP and experiments, demonstrating the ability of eFF-ECP to describe correctly the trending of oxygen-centered angles and thus the subtle response of lone pairs to varying chemical environments.

5.2.4 Silicon carbide with combined s - s and s - p eFF-ECP

We used GARFfield[15] to develop the eFF-ECP force field for SiC tabulated in Table 5.5. These were obtained by optimizing the parameters for a p -type carbon ECP expression (5.5) along with our previously published s -type silicon parameters[8]. In this eFF-ECP scheme, both silicon and carbon atoms are represented by a core effective potential and four valence electrons. Since the electrons are represented by spherical Gaussians with a position, size and spin, the parameter optimization for geometries with complex bonding structures is more challenging than that of a conventional force field. We used lower and upper parameter range values between 0.5-3 for the ECP-radius, and 0-100.0 for a, b, c, d, e .

Table 5.5. Carbon s - p functional form parameters in the SiC-ECP force field and Silicon s - s parameters from Ref. [8].

Atom	ECP-radius	a	b	c	d	e
Si	1.691	0.320852	2.283269	0.814857		
C	0.630348	21.344508	0.715963	0.954384	14.261287	5.314525

We find that the eFF-ECP force field accurately captures the proper lattice constant for 3C-SiC zinc blende, 4.3496 Å at 0 K and 4.3551 Å at 297 K. The latter was computed from the radial distribution function (RDF) between nuclear pairs and the corresponding coordination number. A

4096 atom 3C-SiC fully periodic cubic unit cell was minimized to a 10^{-8} a.u. energy difference using conjugate gradient minimization. 100 fs of equilibrated NVT MD at 297 K (controlled by Nose-Hoover thermostat) was run in LAMMPS with the *eff/cut pair style* [1] to determine the average RDF and coordination number. Experimental results report a value of 4.3596 Å at 297 K[19]).

The results for the Si-C bond, and Si-Si-C, Si-C-C, H-C-H, H-Si-H, C-C-Si, C-Si-C, C-Si-Si, Si-C-Si, Si-C-H, and C-Si-H angles from the different conformers in the training set are tabulated in Table 5.6.

Table 5.6. Silicon Carbide training set and optimization results using the *s-p* form ECP for Carbon. All bond lengths in Bohr and angles in degrees.

Structure	Feature	QM (BY3LYP)	eFF-ECP	% Error
SiH ₃ CH ₃	Si-C bond	3.5527	3.8177	7.4594
SiH ₂ CH ₂	Si-C bond	3.2314	4.0231	24.5002
2SiH ₂ 2CH ₂	Si-C bond	3.6417	3.5643	2.1241
2(SiH ₂ CH ₂)	Si-Si-C angle	78.500	80.1411	2.0906
2(SiH ₂ CH ₂)	Si-C-C angle	101.5000	99.8589	1.6168
2(SiH ₂ CH ₂)	H-C-H angle	106.5000	118.1523	10.9411
2(SiH ₂ CH ₂)	H-Si-H angle	107.6000	113.7215	5.6891
C ₂ H ₅ SiH ₃	C-C-Si angle	114.1000	114.8811	0.6846
2(CH ₃)SiH ₂	C-Si-C angle	112.1000	116.4574	3.8871
Si ₂ H ₅ CH ₃	C-Si-Si angle	112.0000	112.298	0.2662
2(SiH ₃)CH ₂	Si-C-Si angle	115.7000	111.8900	3.2930
SiCH	Si-C-H angle	111.3000	116.6054	4.7667
CSiH	C-Si-H angle	109.3000	101.8441	6.8215

In our previous work[20] we applied the SiC eFF-ECP force field to study the hypervelocity impact (HVI) effects of a nano-diamond cluster on a silicon carbide surface. We found that two distinct heat dissipation domains characterize the thermal transport in SiC during HVI: a stopping domain and the shock wave propagation domain. We bracketed the stopping domain between the time of impact and the reversal of momentum. On the other hand, the shock wave propagation domain is the time the impact shock wave traverses the cell. Energy is dissipated throughout the cell by onto phonon modes that couple with the shock wave. A greater number of electrons are ionized in the stopping phase, and energy is dissipated more effectively by thermal excitation of electrons than by phonon excitation and scattering.

5.3 Conclusions

We have developed an ECP representation in the framework of eFF that overcomes important problems associated with the spherical Gaussian basis set used, and enables the study of dynamic phenomena in materials exposed to extreme loading conditions (including mechanical, thermal, radiation, and other). The ECP enhancements to eFF enable:

- accurate simulation of high- Z elements, up to p -block (e.g., C, Si, O, SiC),
- substantial improvements in the description of multiple bonds (e.g., C),
- accurate description of lone pairs (e.g., O),
- accurate description of complex binaries (e.g., SiC).

In addition to enabling the simulation of systems with increasingly non-spherical electrons, the eFF-ECP representation leads to a significant reduction in the total number of degrees of freedom and filters out high frequency modes from core electrons. This results in larger integration time steps when solving EOM (up to an order of magnitude larger than the all-electron eFF) and enables longer simulation timescales. The eFF-ECP together with a fixed-core representation, which freezes the core electrons for elements $Z > 2$, are available along with the all-electron representation in the open source parallel code of eFF in LAMMPS. All the example cases presented here were calculated using this implementation[1].

References

- [1] Jaramillo-Botero, A, Su, J. T, An, Q, & Goddard, W. A. (2011) Large-scale, long-term nonadiabatic electron molecular dynamics for describing material properties and phenomena in extreme environments. *J. Comput. Chem.* **32**, 497–512.
- [2] Tully, J. C. (1990) Molecular-dynamics with electronic-transitions. *J. Chem. Phys.* **93**, 1061–1071.
- [3] Li, X. S, Tully, J. C, Schlegel, H. B, & Frisch, M. J. (2005) Ab initio Ehrenfest dynamics. *J. Chem. Phys.* **123**, 084106.
- [4] Isborn, C. M, Li, X. S, & Tully, J. C. (2007) Time-dependent density functional theory Ehrenfest dynamics: Collisions between atomic oxygen and graphite clusters. *J. Chem. Phys.* **126**, 134307.
- [5] Klakow, D, Reinhard, P. G, & Toepffer, C. (1997) Semiclassical dynamics in a fluctuating potential. *Ann. Phys.* **259**, 141–162.
- [6] Knaup, M, Reinhard, P. G, Toepffer, C, & Zwicknagel, G. (2003) Wave packet molecular dynamics simulations of warm dense hydrogen. *J. Phys. A: Math. Gen.* **36**, 6165–6171.
- [7] Su, J. T & Goddard, W. A. (2007) Excited electron dynamics modeling of warm dense matter. *Phys. Rev. Lett.* **99**, 185003.
- [8] Theofanis, P. L, Jaramillo-Botero, A, Goddard, W. A, & Xiao, H. (2012) Nonadiabatic study of dynamic electronic effects during brittle fracture of silicon. *Phys. Rev. Lett.* **108**, 045501.

- [9] Su, J. T & Goddard, W. A. (2009) Mechanisms of Auger-induced chemistry derived from wave packet dynamics. *Proc. Natl. Acad. Sci. U.S.A.* **106**, 1001–1005.
- [10] Kim, H, Su, J. T, & Goddard, W. A. (2011) High-temperature high-pressure phases of lithium from electron force field (eFF) quantum electron dynamics simulations. *Proc. Natl. Acad. Sci. U.S.A.* **108**, 15101–15105.
- [11] Theofanis, P. L, Jaramillo-Botero, A, Goddard, W. A, Mattsson, T. R, & Thompson, A. P. (2012) Electron dynamics of shocked polyethylene crystal. *Phys. Rev. B* **85**, 094109.
- [12] Chenard-Lemire, C, Lewis, L. J, & Meunier, M. (2012) Laser-induced Coulomb explosion in C and Si nanoclusters: The determining role of pulse duration. *Appl. Surf. Sci.* **258**, 9404–9407.
- [13] Su, J. T & Goddard, W. A. (2009) The dynamics of highly excited electronic systems: Applications of the electron force field. *J. Chem. Phys.* **131**, 244501.
- [14] Plimpton, S. (1995) Fast parallel algorithms for short-range molecular-dynamics. *J. Comput. Phys.* **117**, 1–19.
- [15] Jaramillo-Botero, A, Naserifar, S, & Goddard, W. A. (2014) General multiobjective force field optimization framework, with application to reactive force fields for silicon carbide. *J. Chem. Theory Comput.* **10**, 1426–1439.
- [16] Kawamura, H, Kumar, V, Sun, Q, & Kawazoe, Y. (2003) Cyclic and linear polymeric structures of Al_nH_{3n} ($n=3-7$) molecules. *Phys. Rev. A* **67**, 063205.
- [17] Spanu, L, Sorella, S, & Galli, G. (2009) Nature and strength of interlayer binding in graphite. *Phys. Rev. Lett.* **103**, 196401.
- [18] Liu, Y & Goddard, W. A. (2010) First-principles-based dispersion augmented density functional theory: From molecules to crystals. *J. Phys. Chem. Lett.* **1**, 2550–2555.
- [19] Taylor, A & Jones, R. M. (1960) *Silicon Carbide – A High Temperature Semiconductor*, eds. O'Connor, J. R & Smiltens, J. (Pergamon Press, Oxford, London, New York, Paris) Vol. 1, p. 147.
- [20] Jaramillo-Botero, A, Nielsen, R, Abrol, R, Su, J. T, Pascal, T. A, Mueller, J, & Goddard, W. A. (2012) First-principles-based multiscale, multiparadigm molecular mechanics and dynamics methods for describing complex chemical processes. *Top. Curr. Chem.* **307**, 1–42.

Chapter 6

Gaussian Hartree approximated QM with angular momentum projected effective core pseudopotential

The contents presented in this chapter are based on [H. Xiao](#), W. A. Goddard, III, A. Jaramillo-Botero and S. S. Dong, *in preparation*, **2015**.

eFF presents a promising framework to explicitly include electrons for modeling of large scale systems, and thus it not only can smoothly circumvent difficulties that traditional force field methods have associated with electrons (or electron densities) in, e.g., lone pairs (dipole moment of water molecule), polarizability, and charge variations (distinguishing between atoms and ions), but also it can enable propagation of electrons for non-adiabatic dynamics. The framework is based on the eFF concept, as stated in its name, that is evaluating QM energies of the total electronic wavefunction in a force field manner, by the sum of local (pairwise, 3- and/or 4-body) interactions. To realize this, two key approximations were introduced: the FSG representation of electrons and Pauli potentials accounting for the antisymmetry of electronic wavefunction.

Although eFF has demonstrated successful applications in several challenging systems (see Ch. 5 and reference therein), it is subject to limitations originated from approximations adopted in the framework. An essential one is the semi-empirical design of the kernel of eFF, i.e., the Pauli potentials: it is constructed with solely the kinetic energy penalty upon antisymmetrization, based on the fact that kinetic energy penalty is the dominant contribution, while the rest is partly accounted for by the parameters introduced and fitted against a set of molecules[1, 2]; however, we found later that the electron-electron Coulomb part contributes non-negligible stabilization of same-spin electron pairs (the so-called exchange energy), and the nucleus-electron Coulomb part is crucial to preventing unphysical coalescence of same-spin electron pairs; besides, the extra parameterization

diverts the Pauli potentials from rigorous description of Gaussian electron pairs. An associated concern is that whether the QM total energy can be evaluated as direct sum of pairwise energies is not explicitly justified. Another limitation is from the deficiency of single FSG representation of each electron, which is missing the cusp condition[3] and explicit nodal structures; the former results in weaker binding energies between nuclei and electrons, e.g., the IP of H is predicted to be only 11.5 eV by eFF (versus the exact value of 13.6 eV), and the latter leads to poor description of systems involving strong higher angular momentum characters, e.g., multiple bonds (unsaturated hydrocarbons) and lone pairs (water molecule) in compounds of *p*-block elements.

To overcome these, very recently we developed a new framework of two-level hierarchy that is more rigorous and accurate. The fundamental level is based on a new set of Pauli potentials that renders an exact QM level of accuracy for any FSG represented electron systems. To achieve this, we started with reproducing the exact QM energies of same and opposite spin FSG electron pairs, and then symmetric and asymmetric scaling factors were designed to recover the correct QM total energy from direct sum of local energies for systems with more than two electrons. Since the Hartree product formalism of total wavefunction is kept in the new framework, we termed this level as Gaussian Hartree approximated QM (GHA-QM), to distinguish from the original eFF method. With GHA-QM describing FSG electrons accurately, the remaining error comes entirely from the deficiency of basis set, and the second level is introducing the angular momentum projected effective core pseudopotential (AMPERE) to compensate for the missing cusp condition and nodal structures. It is worth emphasizing here that the AMPERE is not only to replace core electrons for reducing computational cost, but also more importantly to complement the FSG basis set, similar to the role of pseudopotentials for plane wave basis sets. Therefore, even for H, in which there is no core electron and the traditional ECP concept makes no sense, the AMPERE was introduced to improve the description. This chapter presents the framework of GHA-QM plus AMPERE in detail.

6.1 Exact QM energies of same spin FSG electron pair

The normalized one-electron wavefunction under FSG representation is, neglecting phase factors associated with dynamics,

$$\phi_i(\vec{r}) = \left(\frac{\sqrt{2}}{\sqrt{\pi}s_i} \right)^{3/2} \exp \left[-\frac{1}{s_i^2} (\vec{r} - \vec{R}_i)^2 \right]$$

where \vec{R}_i and s_i are electron position and size, respectively. Following the eFF derivation[1, 2], consider the Slater and Hartree forms for the same spin FSG electron pair:

$$\Psi_{\text{Slater}} = \frac{1}{\sqrt{2 - 2S^2}} [\phi_1(\vec{r}_1)\phi_2(\vec{r}_2) - \phi_2(\vec{r}_1)\phi_1(\vec{r}_2)]$$

$$\Psi_{\text{Hartree}} = \phi_1(\vec{r}_1)\phi_2(\vec{r}_2)$$

where the overlap

$$S = \langle 1|2 \rangle = \int \phi_1(\vec{r})\phi_2(\vec{r})d\vec{r} = \left(\frac{2s_1s_2}{s_1^2+s_2^2}\right)^{3/2} \exp\left(-\frac{R_{12}^2}{s_1^2+s_2^2}\right) \quad (6.1)$$

Then the energy difference upon antisymmetrization is evaluated as

$$\Delta H = \langle \Psi_{\text{Slater}} | \hat{H} | \Psi_{\text{Slater}} \rangle - \langle \Psi_{\text{Hartree}} | \hat{H} | \Psi_{\text{Hartree}} \rangle \quad (6.2)$$

In the eFF framework, only the kinetic energy penalty is included:

$$\begin{aligned} \Delta T &= \left\langle \Psi_{\text{Slater}} \left| -\frac{1}{2}\nabla_1^2 - \frac{1}{2}\nabla_2^2 \right| \Psi_{\text{Slater}} \right\rangle - \left\langle \Psi_{\text{Hartree}} \left| -\frac{1}{2}\nabla_1^2 - \frac{1}{2}\nabla_2^2 \right| \Psi_{\text{Hartree}} \right\rangle \\ &= \frac{S^2}{1-S^2} (t_{11} + t_{22} - 2t_{12}/S) \end{aligned} \quad (6.3)$$

where

$$\begin{aligned} t_{11} &= \left\langle 1 \left| -\frac{1}{2}\nabla^2 \right| 1 \right\rangle = \frac{3}{2} \frac{1}{s_1^2}, \quad t_{22} = \left\langle 2 \left| -\frac{1}{2}\nabla^2 \right| 2 \right\rangle = \frac{3}{2} \frac{1}{s_2^2} \\ t_{12} &= \left\langle 1 \left| -\frac{1}{2}\nabla^2 \right| 2 \right\rangle = \frac{1}{s_1^2+s_2^2} \left(3 - \frac{2R_{12}^2}{s_1^2+s_2^2} \right) \cdot S \end{aligned}$$

While the full Hamiltonian here is $\hat{H} = -\frac{1}{2}\nabla_1^2 - \frac{1}{2}\nabla_2^2 + \frac{1}{r_{12}} + \sum_n \left(-\frac{Z_n}{r_{1n}} - \frac{Z_n}{r_{2n}} \right)$, where the last term is summing over all nuclei, and we further evaluated other contributions. For the electron-electron ($e-e$) Coulomb repulsion, the energy gain is

$$\begin{aligned} \Delta C_{ee} &= \left\langle \Psi_{\text{Slater}} \left| \frac{1}{r_{12}} \right| \Psi_{\text{Slater}} \right\rangle - \left\langle \Psi_{\text{Hartree}} \left| \frac{1}{r_{12}} \right| \Psi_{\text{Hartree}} \right\rangle \\ &= \frac{S^2}{1-S^2} (J - K/S^2) \end{aligned} \quad (6.4)$$

where

$$\begin{aligned} J &= \left\langle 12 \left| \frac{1}{r_{12}} \right| 12 \right\rangle = \frac{1}{R_{12}} \text{Erf} \left(\frac{\sqrt{2}R_{12}}{\sqrt{s_1^2+s_2^2}} \right) \\ K &= \left\langle 12 \left| \frac{1}{r_{12}} \right| 21 \right\rangle = \sqrt{\frac{2}{\pi}} \frac{\sqrt{s_1^2+s_2^2}}{s_1s_2} \cdot S^2 \end{aligned}$$

the latter is traditionally termed as exchange energy. For the nucleus-electron (n - e) Coulomb attraction, the energy penalty is

$$\begin{aligned}\Delta C_{ne} &= \left\langle \Psi_{\text{Slater}} \left| -\frac{Z_n}{r_{1n}} - \frac{Z_n}{r_{2n}} \right| \Psi_{\text{Slater}} \right\rangle - \left\langle \Psi_{\text{Hartree}} \left| -\frac{Z_n}{r_{1n}} - \frac{Z_n}{r_{2n}} \right| \Psi_{\text{Hartree}} \right\rangle \\ &= \frac{S^2}{1-S^2} (j_{11} + j_{22} - 2j_{12}/S)\end{aligned}\quad (6.5)$$

where

$$\begin{aligned}j_{11} &= \left\langle 1 \left| -\frac{Z_n}{r_{1n}} \right| 1 \right\rangle = -Z_n \frac{\text{Erf} \left(\frac{\sqrt{2}}{s_1} R_{n1} \right)}{R_{n1}}, & j_{22} &= \left\langle 2 \left| -\frac{Z_n}{r_{1n}} \right| 2 \right\rangle = -Z_n \frac{\text{Erf} \left(\frac{\sqrt{2}}{s_2} R_{n2} \right)}{R_{n2}} \\ j_{12} &= \left\langle 1 \left| -\frac{Z_n}{r_{1n}} \right| 2 \right\rangle = -Z_n \frac{\sqrt{s_1^2 + s_2^2}}{s_1 s_2} \frac{\text{Erf} \left(\sqrt{\frac{R_{n1}^2}{s_1^2} + \frac{R_{n2}^2}{s_2^2} - \frac{R_{12}^2}{s_1^2 + s_2^2}} \right)}{\sqrt{\frac{R_{n1}^2}{s_1^2} + \frac{R_{n2}^2}{s_2^2} - \frac{R_{12}^2}{s_1^2 + s_2^2}}} \cdot S\end{aligned}$$

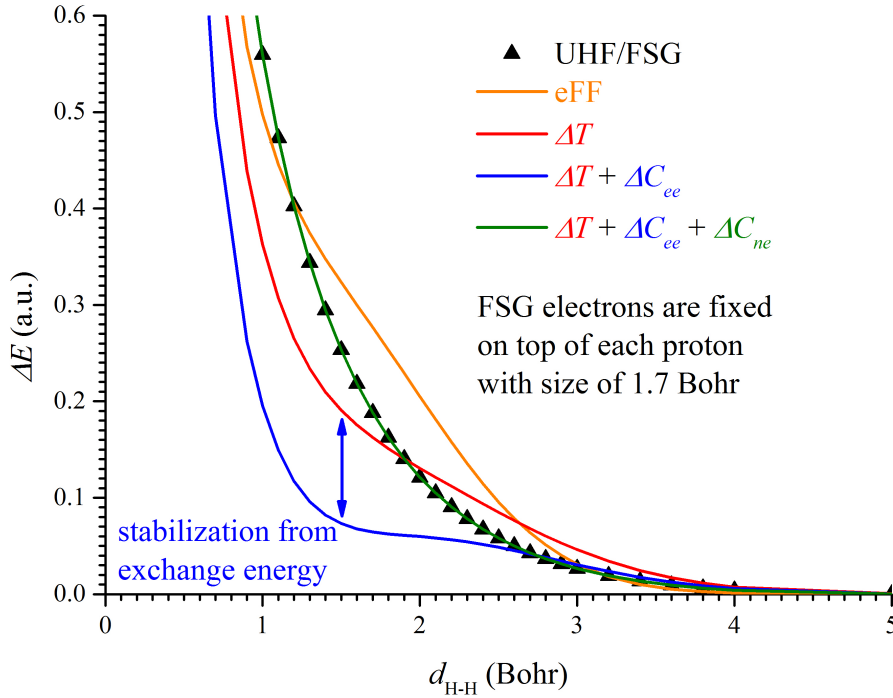


Figure 6.1. Comparison of different energy contributions upon antisymmetrization for total energies of triplet H_2 system. Note that the UHF results are exact here.

To understand the roles of these contributions, we calculated the energies of triplet H_2 system,

as shown in Figure 6.1. Indeed, the curve with only kinetic energy penalty (6.3) resembles the exact one (UHF) well, and based on it the eFF parameterization works reasonably to compensate for the left contributions and approach the exact curve. However, the e - e Coulomb part (6.4) contributes significant stabilization energy and has different dependence of e - e distance from the kinetic energy change, leading to its maximum effect at intermediate distances. Adding further the n - e Coulomb penalty, which is effectively shielding of nuclear charges, balances the exchange stabilization and restores the exact results. In fact, this term plays a crucial role, which is shown more clearly in Figure 6.2, where electron wavefunctions are relaxed, that the n - e Coulomb penalty prevents the unphysical coalescence of same spin FSG electrons (associated with sudden collapse in energies), while eFF and solely kinetic energy penalty both predict such violation of Pauli exclusion principle at a H-H distance of 1.6 Bohr.

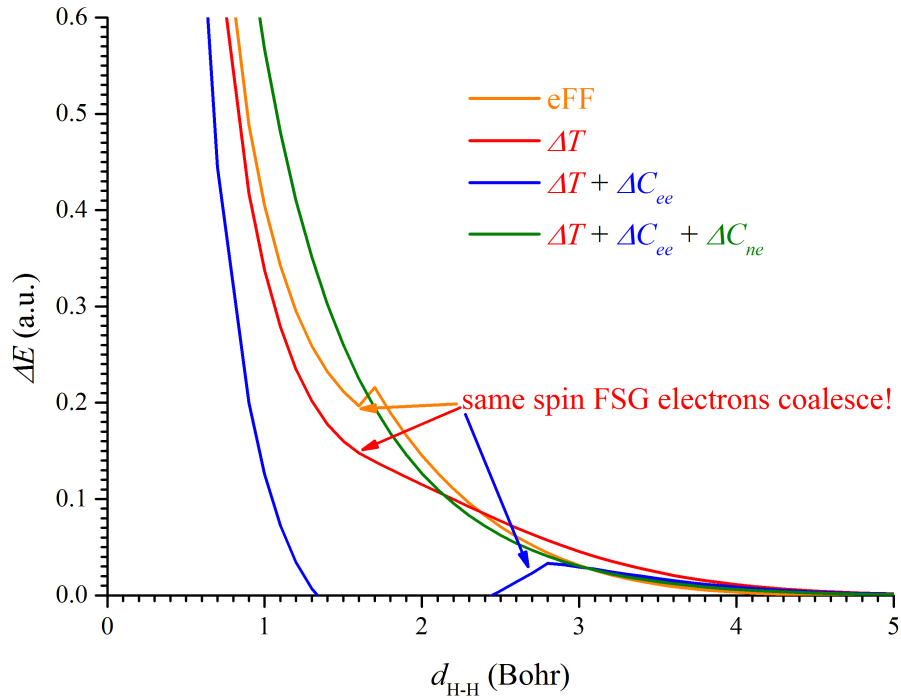


Figure 6.2. Comparison of different energy contributions upon antisymmetrization for optimizing electron wavefunctions of triplet H_2 system. Note that the coalescence of same spin FSG electrons violates the Pauli exclusion principle.

Therefore, in the GHA-QM framework, all three contributions are included to form the foundation of same spin Pauli potential:

$$E_{\text{Pauli}}^{\text{base}}(\uparrow\uparrow) = \Delta T + \Delta C_{ee} + \Delta C_{ne} \quad (6.6)$$

and upon it we next considered the scaling factors for recovering the QM total energy from direct sum of Pauli potentials. Note that (6.3)–(6.5) all introduce numerical instability when $S \rightarrow 1$, so we used series expansions of them (see Appendix A) when $1 - S^2 \leq 0.001$ in the practical implementation in LAMMPS[4].

6.2 Symmetric and asymmetric scaling factors for QM energies of multiple pairs of same spin FSG electrons

The core eFF concept is that the QM total energy can be approximated with the sum over pairs of electrons, while this was not thoroughly justified in the eFF development. Here we first considered two symmetric cases, as shown in Figure 6.3: D_{3h} quartet H_3 and T_d quintet H_4 , in which the overlaps between every pair of electrons are identical. It is clear that both eFF and directly summing of (6.6) over pairs of electrons significantly overestimate ($10^{-1} - 10^0$ a.u. larger) the QM total energies, except at large distances where H atoms are essentially isolated from each other (vanishing overlaps and pairwise interactions). This overestimation can be partly understood with the fact that the kinetic and n - e Coulomb energies are by nature one-body properties of electrons, and thus should scale as the number of electrons N , but the sum of pairwise primitive Pauli potentials makes them scale as N^2 . Therefore, we designed the second tier of GHA-QM, i.e., scaling factors, upon the basis (6.6).

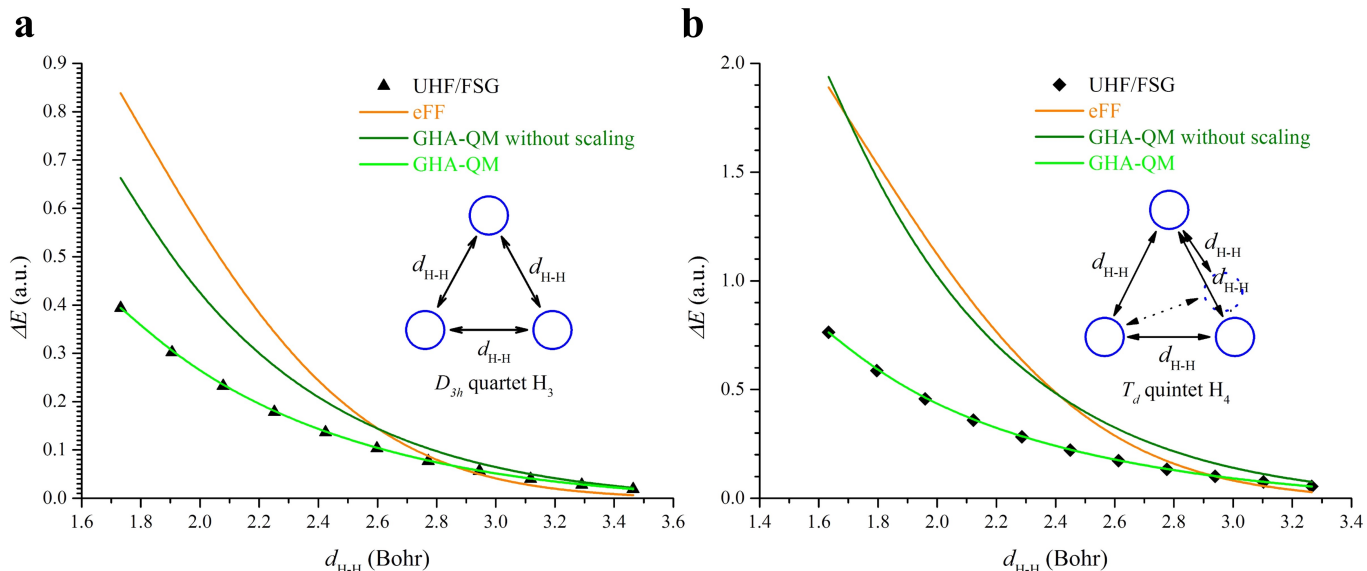


Figure 6.3. Benchmark of eFF, GHA-QM with and without scaling on (a) D_{3h} quartet H_3 and (b) T_d quintet H_4 . Note that the UHF results are exact here.

The scaling factors for pairwise Pauli potentials should be dependent of the environment of each

pair of electrons, and two basic quantities were chosen to characterize the environment of each (i, j) pair:

$$\sum S \equiv \frac{1}{2} \left(\sum_k S_{ik} + \sum_{k'} S_{jk'} \right) \quad (6.7)$$

$$\sum S^2 \equiv \frac{1}{2} \left(\sum_k S_{ik}^2 + \sum_{k'} S_{jk'}^2 \right) \quad (6.8)$$

which can be computed pairwise before evaluating the Pauli potentials, so they don't burden the computational scaling (except for the force evaluation, in which three- and four-body terms are introduced by them in theory, but are easily tailored into linear scaling by applying the tapered cutoff function). We found that the scaling factors for both kinetic and n - e Coulomb energy penalties can be derived, for the two symmetric cases in Figure 6.3, as exact formulas,

$$F_{ij, sym}(\Delta T, \Delta C_{ne}) = \frac{1 + S_{ij}}{1 + \sum S} \quad (6.9)$$

which reproduce the exact QM results, as shown in Figure 6.4. While the scaling factor function for ΔC_{ee} was fitted against the exact QM results, using the form,

$$F_{ij, sym}(\Delta C_{ee}) = f \left(\frac{a + S_{ij}}{a + \sum S} + \frac{\sum S - S_{ij}}{aS_{ij} + \sum S} \right)^b + (1 - f) \left(\frac{c + S_{ij}^2}{c + \sum S^2} + \frac{\sum S^2 - S_{ij}^2}{cS_{ij}^2 + \sum S^2} \right)^d \quad (6.10)$$

with the parameters, $a = 116.9718391437184124$, $b = 5.5068443857879181$, $c = 0.4615515285274991$, $d = 4.5458219639195647$, $f = 0.9763884223181994$, giving excellent performance as in Figure 6.3.

However, with (6.9) and (6.10) aiming at fully symmetric cases (with identical overlaps), it is expected that for asymmetric transitions, as shown in Figure 6.5, the total energies deviate slightly from the exact values. Therefore, for both eliminating these small errors and the completeness of framework, asymmetric scaling factor functions were designed with the form,

$$F_{ij, asym}(\Delta T, \Delta C_{ee}, \Delta C_{ne}) = 1 + a \left(S_{ij} \sum S - \sum S^2 \right) + b \left(S_{ij} \sum S - \sum S^2 \right)^2 + c \left(S_{ij} \sum S - \sum S^2 \right)^3 \quad (6.11)$$

and the fitted parameters are listed in Table 6.1.

Table 6.1. Fitted parameters for asymmetric scaling factor functions (6.11).

Type	a	b	c
ΔT	7.0275135953301424	-1.3235214678707308	-207.9886055974747308
ΔC_{ee}	-2.4227129678577675	18.2962351504751588	13.4791835822684352
ΔC_{ne}	2.3795506051854529	27.6722999507131213	-51.7840176813005328

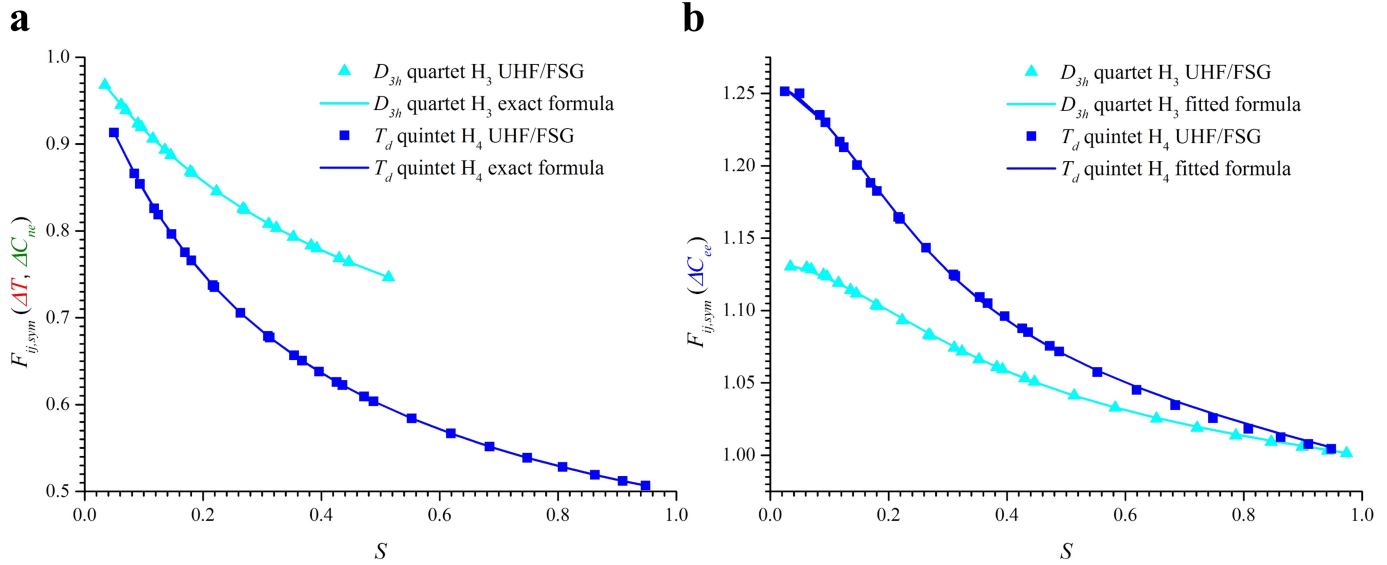


Figure 6.4. Performance of symmetric scaling factor functions for (a) ΔT , ΔC_{ne} and (b) ΔC_{ee} on D_{3h} quartet H_3 and T_d quintet H_4 . Note that the UHF results are exact here.

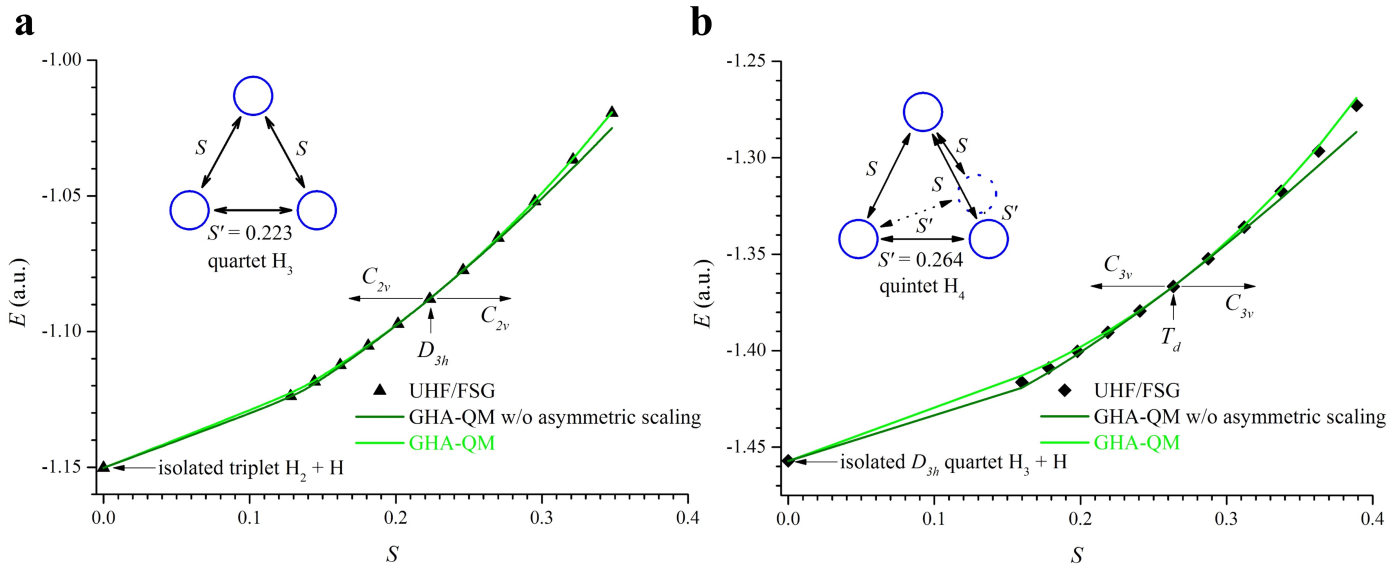


Figure 6.5. Performance of asymmetric scaling factor functions on (a) quartet H_3 transition from D_{3h} to C_{2v} and (b) quintet H_4 transition from T_d to C_{3v} . Note that the UHF results are exact here.

Summarizing, the same spin Pauli potential in the GHA-QM framework is evaluated as

$$\begin{aligned}
 E_{\text{Pauli}}(\uparrow\uparrow) = & F_{\text{asym}}(\Delta T) F_{\text{sym}}(\Delta T) \Delta T + F_{\text{asym}}(\Delta C_{ee}) F_{\text{sym}}(\Delta C_{ee}) \Delta C_{ee} \\
 & + F_{\text{asym}}(\Delta C_{ne}) F_{\text{sym}}(\Delta C_{ne}) \Delta C_{ne}
 \end{aligned} \tag{6.12}$$

This ultimate expression renders accurate description of FSG represented electrons with same spins, as shown in Figures 6.3 and 6.5, with deviations of order of magnitude of only 10^{-3} a.u. from exact QM results. Note that all scaling factor functions (6.9)–(6.11) equal exactly to 1 at the limit $S_{ij} = \sum S$, i.e., when the system has only one pair of same spin electrons, as in the case of triplet H_2 , and (6.12) goes back to (6.6), which is exact for two same spin electron systems as shown in Figure 6.1.

6.3 Design of opposite spin Pauli potential

For a pair of opposite spin electrons, its spin eigenfunction (singlet state) $\frac{1}{\sqrt{2}}(|\uparrow\downarrow\rangle - |\downarrow\uparrow\rangle)$ already assumes the antisymmetry, so there are multiple choices for the spatial wavefunction as long as it is symmetric, and three typical candidates are HF, VB, and GVB[5] descriptions as below,

$$\begin{aligned}\Psi_{\text{HF}} &= \frac{1}{2+2S} [\phi_1(\vec{r}_1)\phi_2(\vec{r}_2) + \phi_2(\vec{r}_1)\phi_1(\vec{r}_2) + \phi_1(\vec{r}_1)\phi_1(\vec{r}_2) + \phi_2(\vec{r}_1)\phi_2(\vec{r}_2)] \\ \Psi_{\text{VB}} &= \frac{1}{\sqrt{2+2S^2}} [\phi_1(\vec{r}_1)\phi_2(\vec{r}_2) + \phi_2(\vec{r}_1)\phi_1(\vec{r}_2)] \\ \Psi_{\text{GVB}} &= \frac{1}{\sqrt{2(1+g^2)(1+S^2)+8gS}} \{ \phi_1(\vec{r}_1)\phi_2(\vec{r}_2) + \phi_2(\vec{r}_1)\phi_1(\vec{r}_2) \\ &\quad + g[\phi_1(\vec{r}_1)\phi_1(\vec{r}_2) + \phi_2(\vec{r}_1)\phi_2(\vec{r}_2)] \}\end{aligned}$$

among those, VB was the choice of eFF framework. However, all these wavefunction-based approaches under single FSG representation suffer from a problem, that is, when two opposite spin electrons coalesce (e.g., in He atom), the FSG basis functions are completely linear dependent, and thus any wavefunction forms converge to the Hartree product and lead to zero energy gains (no correlation). This problem causes difficulty in properly describing such systems as He and H^- . Additional effort borrowing ideas from DFT is necessary to address the correlation. A hybrid scheme, in which a wavefunction-based approach is used to cover the UHF level and a DFT-like functional for the remaining correlation, was originally adopted (see Appendix B), but led to complicated parameterization and scaling considerations. Therefore, we later designed a simpler formula, inspired by the Wigner correlation functional[6],

$$E_{\text{Pauli}}^{\text{base}}(\uparrow\downarrow) = -\frac{p_0 S^{p_1} + p_2 S^{p_3} \bar{s}^{p_4}}{1 + p_5 S^{p_6} + p_7 S^{p_8} \bar{s}^{p_9}} \quad (6.13)$$

where $\bar{s} \equiv \frac{s_1 s_2}{\sqrt{s_1^2 + s_2^2}}$. The parameters were fitted against B3LYP results of open singlet H_2 cases with varying both H–H distances and electron sizes, as shown in Figure 6.6. The resulting parameters are listed in Table 6.2. Figure 6.7 illustrates the performance of GHA-QM on two-electron systems, with the open singlet and triplet H_2 cases. It is clearly shown that GHA-QM reproduces accurately

the QM results under single FSG representation, with errors less than 2 kcal/mol for opposite spin cases (GHA-QM is exact for same spin cases under single FSG representation). However, similar to the development of same spin Pauli potential, scaling factors are also necessary for opposite spin Pauli potential to recover the QM total energies of systems with multiple pairs of opposite spin electrons.

Table 6.2. Fitted parameters for (6.13).

p_0	p_1	p_2	p_3	p_4
0.7991062973926818	3.0784366182756111	0.6166511924591953	1.1405494582541387	-3.1346281136377732
p_5	p_6	p_7	p_8	p_9
6.6953936536408047	2.8848038115685481	16.0190065556333749	12.8490416580987876	0.0396897141066533

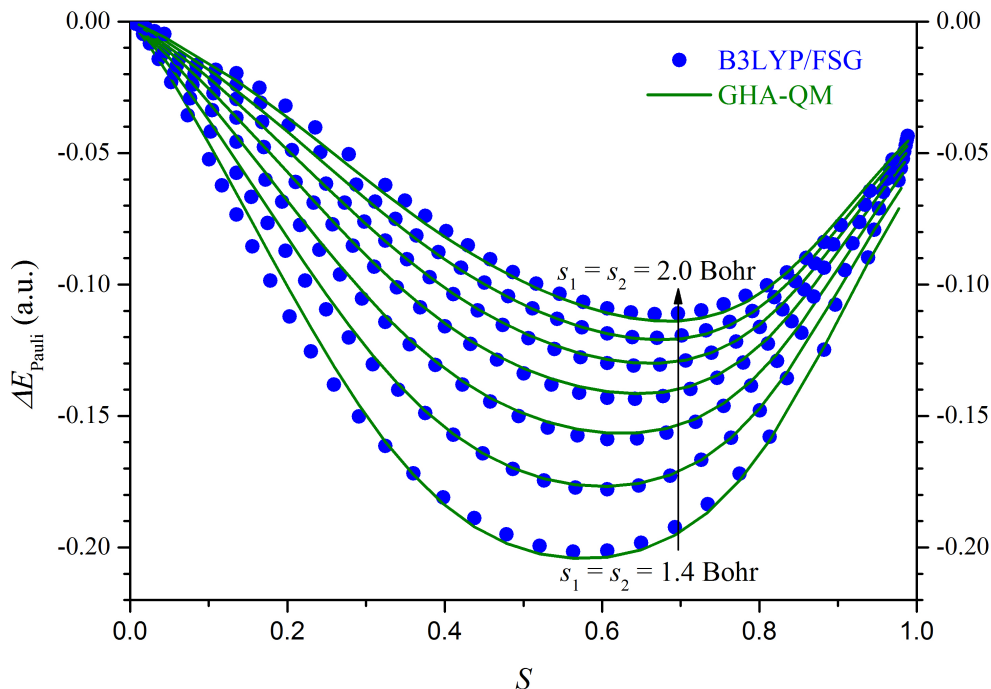


Figure 6.6. Fitting of opposite spin Pauli potential against open singlet H_2 at B3LYP level. Each curve has fixed electron sizes of a value from 1.4 to 2.0 Bohr, and H-H distances are varied to cover the whole range of overlap. ΔE_{Pauli} here is the difference between the QM bonding energy and classical contribution, so it includes the correlation energy.

Following the same strategy as the same spin case, the symmetric scaling factor was first designed, aiming at two classical cases, linear $D_{\infty h}$ doublet H_3 and square D_{4h} singlet H_4 TSs. Note that the D_{4h} H_4 TS with triplet state is lower in energy, but here it is more focused on examining the dissociation into two H_2 molecules, and spin flip would complicate the design of scaling factors. We

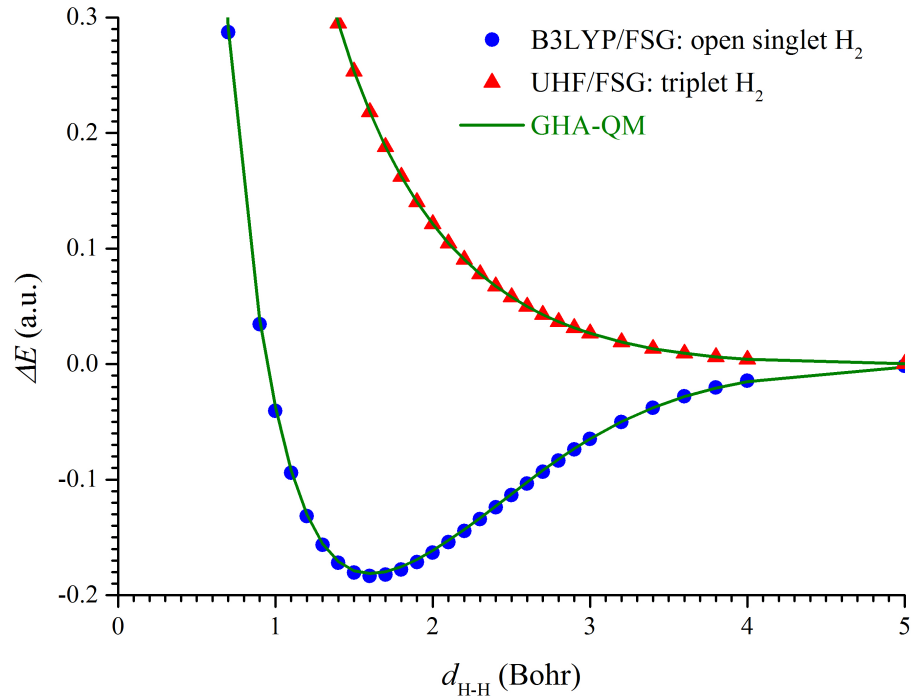


Figure 6.7. Performance of GHA-QM on the open singlet and triplet H_2 systems. Note that all electron sizes are fixed at 1.7 Bohr.

adopted a simple functional form for symmetric scaling factor,

$$F_{ij, sym}(\uparrow\downarrow) = f \left(\frac{1 + aS_{ij}}{1 + a \sum S} \right)^b + (1 - f) \left(\frac{1 + cS_{ij}^2}{1 + c \sum S^2} \right)^d \quad (6.14)$$

where the parameters $f = 1.2185048809195764$, $a = 0.7733298802023484$, $b = 6.0665565953273131$, $c = 6.2137768045322064$, and $d = 40.1429807287959051$ were fitted against the symmetric stretching modes in $D_{\infty h}$ doublet H_3 and D_{4h} singlet H_4 TSs. The performance is shown in Figure 6.8, and there is excellent agreement between GHA-QM and B3LYP on the $D_{\infty h}$ doublet H_3 symmetric stretching curve, but GHA-QM gives considerable overestimation of the D_{4h} singlet H_4 case. This is most likely due to the fact that the GHA-QM description is a pure singlet state with alternating spins on the square, while the open singlet state from single-determinant DFT method is a mixed state, contaminated by the triplet state with lower energy. Bearing this in mind, we put less focus on the D_{4h} singlet H_4 case, and the overestimation at short distances is neglected.

The asymmetric scaling was next introduced naturally to account for the dissociation of $D_{\infty h}$ doublet H_3 TS into H_2 molecule and H atom, and of D_{4h} open singlet H_4 TS into two H_2 molecules.

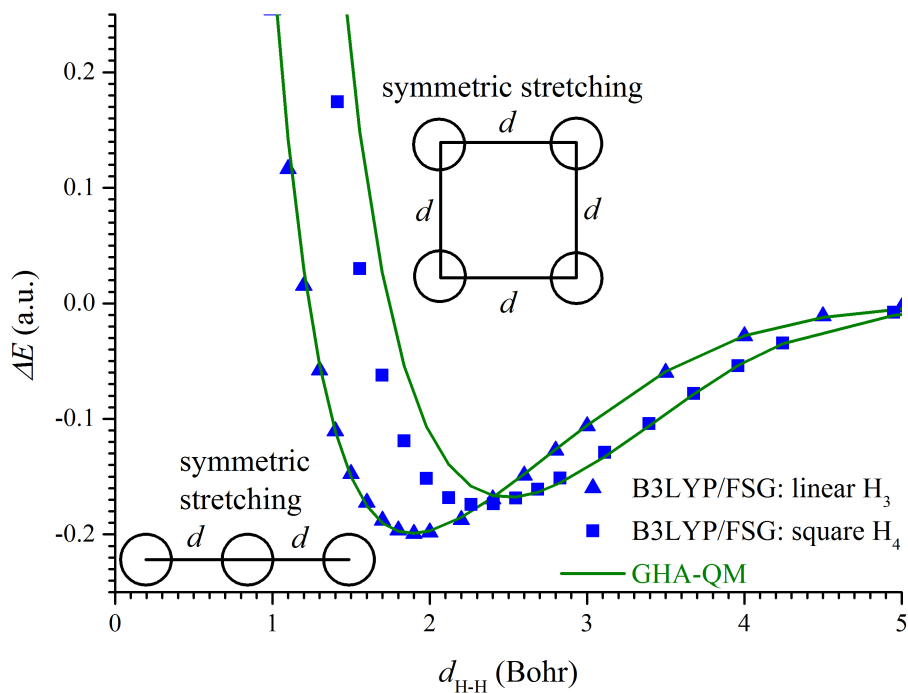


Figure 6.8. Performance of GHA-QM on symmetric stretching modes in $D_{\infty h}$ doublet H_3 and D_{4h} open singlet H_4 TSs.

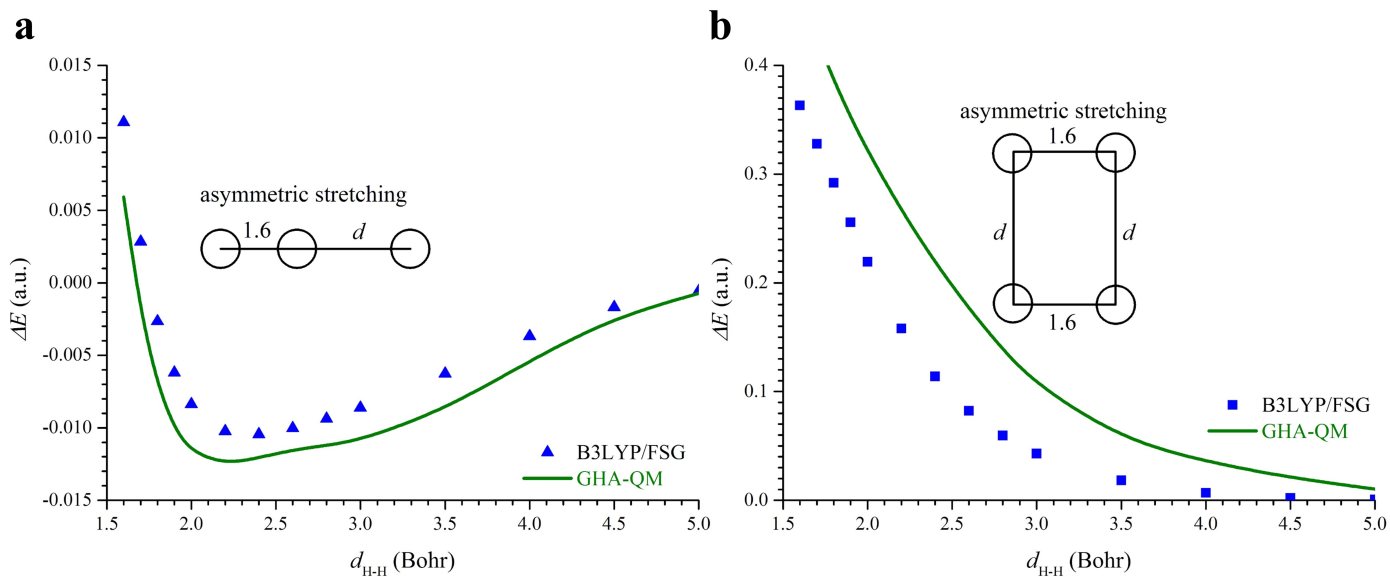


Figure 6.9. Performance of GHA-QM on asymmetric stretching modes in (a) $D_{\infty h}$ doublet H_3 and (b) D_{4h} open singlet H_4 TSs, those result in dissociation into the reference H_2 molecule(s) and H atom.

The functional form is

$$F_{ij,asym}(\uparrow\downarrow) = 1 + a \left(\frac{S_{ij} \sum S - \sum S^2}{S_{ij} \sum S + \sum S^2} \right) + b \left(\frac{S_{ij} \sum S - \sum S^2}{S_{ij} \sum S + \sum S^2} \right)^2 + c \left(\frac{S_{ij} \sum S - \sum S^2}{S_{ij} \sum S + \sum S^2} \right)^3 \quad (6.15)$$

where the parameters $a = 0.2083861613347705$, $b = 1.5231359602535302$, $c = -3.0614893533656828$ were fitted against the two dissociation processes, with much more weight on the H_3 case. The performance is shown in Figure 6.9. The small deviations (less than 2 kcal/mol) for the H_3 case originate from the reference energy of H_2 molecule (see discussions of the fitting of (6.13)), while the big overestimation for the H_4 case is just inherited from the symmetric scaling part, as discussed above.

Summarizing, the opposite spin Pauli potential in the GHA-QM framework is evaluated as

$$E_{\text{Pauli}}(\uparrow\downarrow) = F_{asym}(\uparrow\downarrow) F_{sym}(\uparrow\downarrow) E_{\text{Pauli}}^{\text{base}}(\uparrow\downarrow) \quad (6.16)$$

This final equation captures the essence of correlation and gives accurate description of FSG represented electron pair with opposite spins, as in H_2 molecule, and accommodates reasonably well the description of H_3 and H_4 TSs. This rational design of $E_{\text{Pauli}}(\uparrow\downarrow)$ stands as one of the great improvements over the eFF method, where the correlation is essentially missing.

6.4 The AMPERE extension

GHA-QM constitutes the foundation of our new method that approximates accurately QM under FSG representation, and AMPERE is the key natural extension to minimize the only remaining errors arising from the deficiency of underlying basis set. One intrinsic flaw of single FSG basis set is the absence of cusp condition of electron density on top of nucleus, and the traditional solution in quantum chemistry is using multiple Gaussian functions to approximate the Slater type orbital ($e^{-\zeta r}$)[7–9], which resembles much more the real AOs, but such scheme complicates much the framework on both energy evaluation and EOM (size variation especially). Plane wave type basis set faces the same problem, due to the formidable effort required to approximate electron density in the vicinity of nuclei, leading to exorbitant computational cost for practical applications, and thus pseudopotentials were introduced to embed the interactions associated with the sharp electron density in a predefined core region (see, e.g., Ref. [10]), and the corresponding pseudo eigen orbitals are much smoother in the core region and easily expanded in terms of plane waves. Therefore, in order to retain the simplicity of our framework, we resort to this solution, and introduced AMPERE, even for H element (no core electrons), to embed the cusp condition.

The other efficacy of AMPERE is to embed implicitly the interactions arising from the missing explicit nodal structures, and this can be conveniently achieved with the design of our framework. The FSG one-electron wavefunction, centered off from the nucleus or core (normally the case for valence electrons), can be expressed as a linear combination of angular momentum projections centered at the core, as illustrated in Figure 6.10. This implies that the floating nature of FSG provides the flexibility to describe orbitals with higher angular momenta.

$$|\phi_v\rangle = \sum_{\{lm\}_c} |\{lm\}_c\rangle \langle\{lm\}_c|\phi_v\rangle$$

Figure 6.10. Decomposition of valence FSG wavefunction into core-centered orbitals with various angular momenta.

Correspondingly, AMPERE is based on an angular momentum projected construction, borrowed from quantum chemistry[11, 12]. Consider a valence-only one-electron Hamiltonian:

$$\hat{h}_v = -\frac{1}{2}\nabla^2 - \frac{Z_c}{|\vec{r} - \vec{R}_c|} + V(\vec{r} - \vec{R}_c) \quad (6.17)$$

where $V(\vec{r} - \vec{R}_c)$ is the local pseudopotential centered at the core, and can be expanded as an infinite series of angular momentum projection operators:

$$V(\vec{r} - \vec{R}_c) = \sum_{l,m} V_l(|\vec{r} - \vec{R}_c|) |lm\rangle \langle lm|$$

Since it has been found[11] that in practice, there is an L such that $V_l(|\vec{r} - \vec{R}_c|) \cong V_L(|\vec{r} - \vec{R}_c|)$ for $l \geq L$, using the closure property, the expansion is approximated by a finite series:

$$\begin{aligned} V(\vec{r} - \vec{R}_c) &\cong V_L(|\vec{r} - \vec{R}_c|) + \sum_{l=0}^{L-1} \sum_m \left(V_l(|\vec{r} - \vec{R}_c|) - V_L(|\vec{r} - \vec{R}_c|) \right) |lm\rangle \langle lm| \\ &\equiv V_L(|\vec{r} - \vec{R}_c|) + \sum_{l=0}^{L-1} \sum_m V_{l-L}(|\vec{r} - \vec{R}_c|) |lm\rangle \langle lm| \end{aligned} \quad (6.18)$$

For ease in evaluation of integrals, the effective pseudopotentials V_i ($i = L, l - L$) are conventionally fitted to an analytical expansion of the Gaussian form:

$$V_i(|\vec{r} - \vec{R}_c|) = \sum_k C_{ik} |\vec{r} - \vec{R}_c|^{n_{ik}} \exp\left(-\zeta_{ik} |\vec{r} - \vec{R}_c|^2\right) \quad (6.19)$$

where $n_{ik} = -2, -1, 0$ are common choices. The core-valence interaction is then evaluated as, in our framework,

$$E_{cv} = \left\langle \phi_v \left| -\frac{Z_c}{|\vec{r} - \vec{R}_c|} + V(\vec{r} - \vec{R}_c) \right| \phi_v \right\rangle = -\frac{Z_c}{R_{cv}} \text{Erf} \left(\frac{\sqrt{2}R_{cv}}{s_v} \right) + \left\langle \phi_v \left| V(\vec{r} - \vec{R}_c) \right| \phi_v \right\rangle \quad (6.20)$$

Note that the first term implies that a point charge model is used for the core, and no corrections such as core polarization potential[13–15] and core-core repulsion correction with a Born-Mayer type ansatz[16, 17] are currently introduced, which might be necessary when large cores are considered. The last term in (6.20) is further decomposed into

$$\left\langle \phi_v \left| V(\vec{r} - \vec{R}_c) \right| \phi_v \right\rangle = \left\langle \phi_v \left| V_L(|\vec{r} - \vec{R}_c|) \right| \phi_v \right\rangle + \sum_{l=0}^{L-1} \sum_m \left\langle \phi_v \left| V_{l-L}(|\vec{r} - \vec{R}_c|) \right| lm \right\rangle \langle lm | \phi_v \rangle \quad (6.21)$$

in which each term corresponds to the local interaction within one particular angular momentum projection, and is evaluated as a finite series according to (6.19). Explicitly, ϕ_v is expanded about the core center \vec{R}_c [18], with assigning the z axis along \vec{R}_{cv} , as,

$$\begin{aligned} \phi_v &= \left(\frac{\sqrt{2}}{\sqrt{\pi}s_v} \right)^{\frac{3}{2}} \exp \left[-\frac{R_{cv}^2}{s_v^2} \right] \exp \left[-\frac{|\vec{r} - \vec{R}_c|^2}{s_v^2} \right] \\ &\quad \cdot \sum_{l=0}^{\infty} [4\pi(2l+1)]^{\frac{1}{2}} M_l \left(\frac{2R_{cv}}{s_v} \left| \vec{r} - \vec{R}_c \right| \right) Y_l^{m=0}(\theta_c, \phi_c) \\ &\equiv \sum_{l=0}^{\infty} |l0\rangle \langle l0 | \phi_v \rangle \end{aligned} \quad (6.22)$$

where $M_l(z)$ is the modified spherical Bessel function of the first kind, and $Y_l^m(\theta, \phi)$ is the spherical harmonics ($|lm\rangle$). So ϕ_v has nonzero expansion coefficients $\langle lm | \phi_v \rangle$ only for $m = 0$, and (6.21) is simplified as

$$\left\langle \phi_v \left| V(\vec{r} - \vec{R}_c) \right| \phi_v \right\rangle = \left\langle \phi_v \left| V_L(|\vec{r} - \vec{R}_c|) \right| \phi_v \right\rangle + \sum_{l=0}^{L-1} \left\langle \phi_v \left| V_{l-L}(|\vec{r} - \vec{R}_c|) \right| l0 \right\rangle \langle l0 | \phi_v \rangle \quad (6.23)$$

For each l (and L), every n_{ik} in (6.19) contributes an AMPERE energy term with two parameters (one linear coefficient and one exponent), and for brevity, we denote these terms as $l(n_{lk} + 2)$, e.g., $L1$, $s0$, and $p2$. Note that $+2$ comes from the volume element in integration under spherical coordinate system. All integrals emerging from here are evaluated in Appendix C, and the numerical implementation in LAMMPS by me (`pair_eff_eCP.h`) is described in Appendix D.

The very first case we tested the GHA-QM+AMPERE framework on is the H element, for it is an obvious touchstone of the cusp condition. To construct the AMPERE, currently we picked

6 terms, $L0$, $L1$, $L2$, $s0$, $s1$, and $s2$, while a refinement of the choice might be necessary in the future. We fitted the parameters (12 in total) against a small dataset, comprising H IP, H_2 bonding length and energy, which should be augmented with other important species such as H_3 linear transition state in the future work. The current best parameters are $L0$: (0.759292, 2.272014), $L1$: (0.390743, 0.082136), $L2$: (0.700182, 0.542541), $s0$: (-0.632059, 1.092219), $s1$: (-0.135945, 0.093336), $s2$: (-1.051977, 1.420820), which result in H IP of 13.8 eV versus the exact value of 13.6 eV, a great improvement over 11.5 eV from both eFF and GHA-QM. Figure 6.11 shows the performance of GHA-QM+AMPERE on the potential energy curve of H_2 molecule, and both predicted bonding length of 0.741 Å and bonding energy of 111.8 kcal/mol agree excellently with the exact values of 0.741 Å and 109.5 kcal/mol. Note that only the equilibrium point of the curve is included in the dataset for AMPERE fitting, but the rest part of curve is described very well by GHA-QM+AMPERE, which most likely benefits from the well-designed underlying GHA-QM level. Without AMPERE covering for the cusp condition, GHA-QM alone overestimates the bonding because the binding between electrons and protons is weaker, and electrons move more towards the bonding center. eFF performs poorly due to the lack of both correlation and cusp condition.

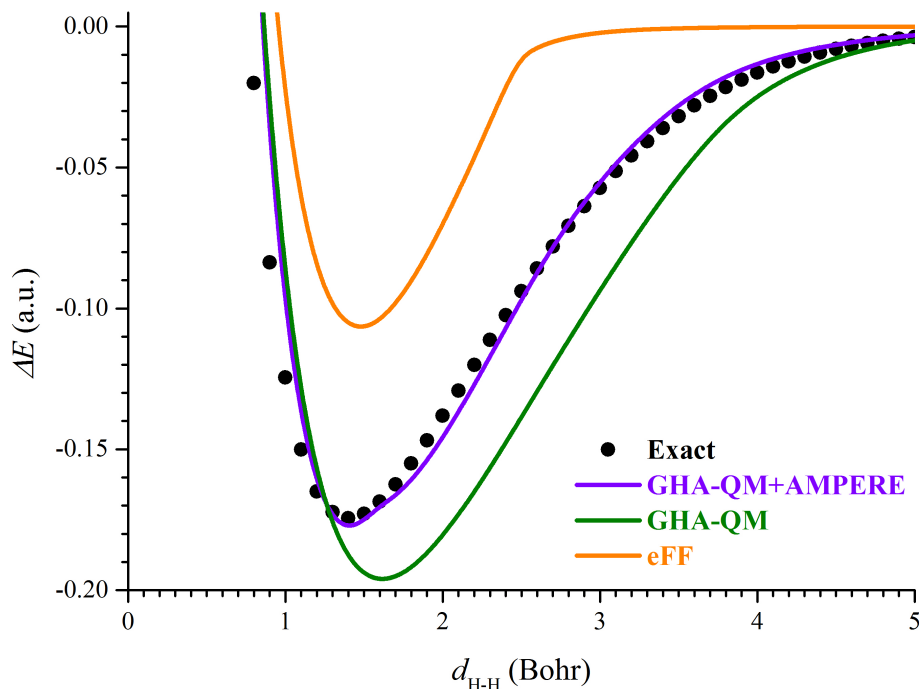


Figure 6.11. Comparison of performance of GHA-QM+AMPERE, GHA-QM and eFF on the dissociation curve of H_2 molecule. The exact curve is taken from Ref. [19].

6.5 Concluding remarks and future work

To conclude, we have built the new GHA-QM+AMPERE framework that is more rigorous and accurate than its predecessor, the eFF method. The GHA-QM forms the foundation and was designed to first describe FSG represented same- or opposite-spin electron pair systems with QM accuracy. This was achieved by using exactly derived energy expressions for same spin case, and fitting a simple functional form, inspired by DFT, against open singlet electron pair curves (H_2 systems). Symmetric and asymmetric scaling factors were then introduced at this level to recover the QM total energies of multiple electron pair systems from the sum of local interactions. To complement the imperfect FSG representation, the AMPERE extension was implemented, and aims at embedding the interactions associated with the cusp condition and explicit nodal structures. The whole GHA-QM+AMPERE framework was tested on H element, and the preliminary results are promising.

It is expected that we will explore widely the applications of GHA-QM+AMPERE, and one particular kind is the p -block elements such as C and O, since we have not well benchmarked the performance of GHA-QM+AMPERE on systems with strong p -character, like multiple bonds and lone pairs, and this will be a key demonstration of how well the AMPERE method embeds the interactions associated with explicit nodal structures.

Appendix

A. Series expansions of ΔT , ΔC_{ee} , and ΔC_{ne}

As $S \rightarrow 1$, $s_1 \rightarrow s_2$ and $R_{12} \rightarrow 0$ (in our implementation, the practical condition is $1 - S^2 \leq 0.001$), (6.3)–(6.5) are computed with the series expansions,

$$\Delta T = \frac{1}{s_1 s_2} - \frac{R_{12}^2}{2s_1^2 s_2^2} + \frac{R_{12}^4}{12s_1^3 s_2^3} + O\left(\frac{R_{12}^8}{s_1^5 s_2^5}\right) \quad (6.A1)$$

$$\Delta C_{ee} = \frac{2}{\sqrt{\pi}} A \left(-\frac{1}{3} + \frac{4}{15} A^2 R_{12}^2 - \frac{32}{315} A^4 R_{12}^4 + \frac{47}{1890} A^6 R_{12}^6 \right) + O(A^9 R_{12}^8) \quad (6.A2)$$

$$\begin{aligned} \Delta C_{ne} = & \frac{Z_n}{\sqrt{\pi}} \frac{\sqrt{s_1^2 + s_2^2}}{s_1 s_2} \cdot \left\{ A_1(R) + \left[\frac{A_2(R)}{2} - A_1(R) \right] x + \left[\frac{A_3(R)}{6} - \frac{A_2(R)}{2} + \frac{A_1(R)}{3} \right] x^2 \right. \\ & \left. + \left[\frac{A_4(R)}{24} - \frac{A_3(R)}{6} + \frac{A_2(R)}{6} \right] x^3 + O(x^4) \right\} \end{aligned} \quad (6.A3)$$

where

$$\begin{aligned} A & \equiv \frac{\sqrt{2}}{\sqrt{s_1^2 + s_2^2}} \\ x & \equiv \frac{R_{12}^2}{s_1^2 + s_2^2} \end{aligned}$$

$$\begin{aligned}
R &\equiv \frac{R_{n1}^2}{s_1^2} + \frac{R_{n2}^2}{s_2^2} \\
A_1(R) &\equiv R^{-3/2} \int_0^R t^{1/2} e^{-t} dt = \frac{\frac{1}{2}\sqrt{\pi}\text{Erf}(R^{1/2}) - R^{1/2}e^{-R}}{R^{3/2}} \\
A_2(R) &\equiv R^{-5/2} \int_0^R t^{3/2} e^{-t} dt = \frac{\frac{3}{4}\sqrt{\pi}\text{Erf}(R^{1/2}) - \frac{1}{2}R^{1/2}(3+2R)e^{-R}}{R^{5/2}} \\
A_3(R) &\equiv R^{-7/2} \int_0^R t^{5/2} e^{-t} dt = \frac{\frac{15}{8}\sqrt{\pi}\text{Erf}(R^{1/2}) - \frac{1}{4}R^{1/2}(15+10R+4R^2)e^{-R}}{R^{7/2}} \\
A_4(R) &\equiv R^{-9/2} \int_0^R t^{7/2} e^{-t} dt = \frac{\frac{105}{16}\sqrt{\pi}\text{Erf}(R^{1/2}) - \frac{1}{8}R^{1/2}(105+70R+28R^2+8R^3)e^{-R}}{R^{9/2}}
\end{aligned}$$

and when $R \rightarrow 0$,

$$\begin{aligned}
A_1(R) &= \frac{2}{3} - \frac{2}{5}R + \frac{1}{7}R^2 - \frac{1}{27}R^3 + \frac{1}{132}R^4 + O(R^4) \\
A_2(R) &= \frac{2}{5} - \frac{2}{7}R + \frac{1}{9}R^2 - \frac{1}{33}R^3 + \frac{1}{156}R^4 + O(R^4) \\
A_3(R) &= \frac{2}{7} - \frac{2}{9}R + \frac{1}{11}R^2 - \frac{1}{39}R^3 + \frac{1}{180}R^4 + O(R^4) \\
A_4(R) &= \frac{2}{9} - \frac{2}{11}R + \frac{1}{13}R^2 - \frac{1}{45}R^3 + \frac{1}{204}R^4 + O(R^4)
\end{aligned}$$

In (6.5), there is another particular source of numerical instability, i.e., the j_{12}/S term, when $x_3 \equiv \sqrt{\frac{R_{n1}^2}{s_1^2} + \frac{R_{n2}^2}{s_2^2} - \frac{R_{12}^2}{s_1^2 + s_2^2}} \rightarrow 0$ (in our implementation, the practical condition is $x_3^2 \leq 0.01$), it is computed with the series expansion,

$$j_{12}/S = -Z_n \frac{\sqrt{s_1^2 + s_2^2}}{s_1 s_2} \cdot \frac{2}{\sqrt{\pi}} \left[1 - \frac{x_3^2}{3} + \frac{x_3^4}{10} - \frac{x_3^6}{42} + \frac{x_3^8}{216} - \frac{x_3^{10}}{1320} + O(x_3^{12}) \right] \quad (6.A4)$$

B. A hybrid scheme to construct opposite spin Pauli potential

Observing that the HF, VB, and GVB representations of opposite spin electron pair lead to kinetic energy stabilization bearing similar forms,

$$\begin{aligned}
\Delta T_{\text{HF}} &= -\frac{S}{1+S} && (t_{11} + t_{22} - 2t_{12}/S) \\
\Delta T_{\text{VB}} &= -\frac{S^2}{1+S^2} && (t_{11} + t_{22} - 2t_{12}/S) \\
\Delta T_{\text{GVB}} &= -\frac{(1+g^2)S^2 + 2gS}{(1+g^2)(1+S^2) + 4gS} && (t_{11} + t_{22} - 2t_{12}/S)
\end{aligned}$$

we designed the base opposite spin Pauli potential for UHF level as,

$$E_{\text{Pauli}}^{\text{base,UHF}}(\uparrow\downarrow) = O(T)(t_{11} + t_{22} - 2t_{12}/S) + O(C_{ee})(J - K/S^2) \\ + O(C_{ne})(j_{11} + j_{22} - 2j_{12}/S) \quad (6.B1)$$

where the prefactors have the form,

$$O(T, C_{ee}, C_{ne}) = -\frac{\sum_{i=1}^6 p_i S^i}{1 + \sum_{i=1}^6 q_i S^i} \quad (6.B2)$$

which is in fact a Padé approximant of order of 6. The parameter sets are subject to constraints,

$$\sum_{i=1}^6 (p, q)_i = 1 \quad \text{for } O(T, C_{ne}) \\ \sum_{i=1}^6 (p, q)_i = 3 \quad \text{for } O(C_{ee}) \quad (6.B3)$$

and fitted against UHF results of open singlet H_2 cases. The fitting performance is shown in Figure 6.B1, and the resulting parameters are listed in Table 6.B1.

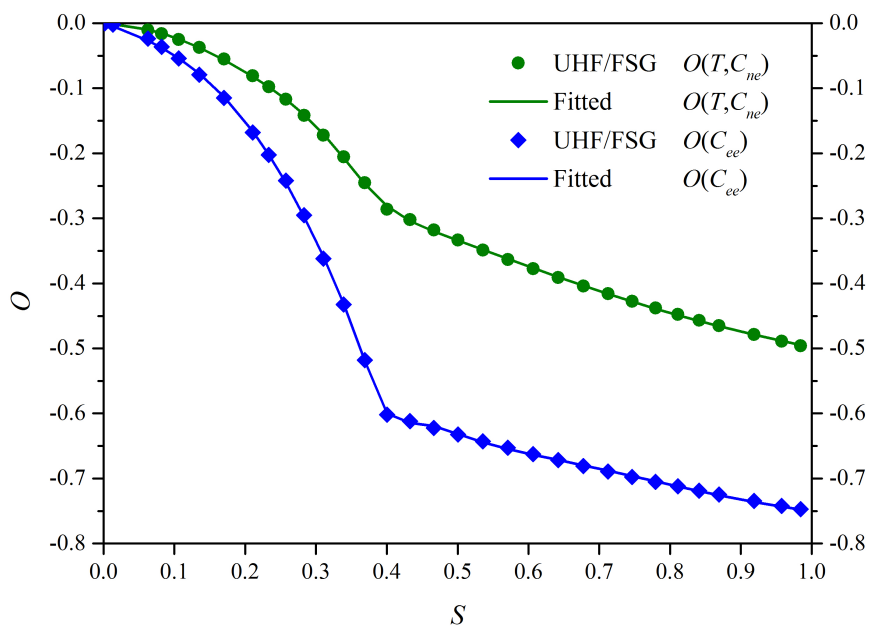


Figure 6.B1. Performance of fitting of prefactors in (6.B1) on open singlet H_2 at UHF level.

Table 6.B1. Fitted parameters for (6.B2) at UHF level.

i		2	3	4	5	6
$O(T, C_{ne})$	p_i	0.323933519549	263.657907116213	-1638.970416101778	3321.931428051212	-1946.189711223903
	q_i	-682.166181317656	1541.546562405113	-2664.652178554171	4522.235374741135	-2833.366958883348
$O(C_{ee})$	p_i	-2.051090853035	4.348307977954	-2.873915950474	-3.557953214220	6.800067465817
	q_i	40.676410634018	-90.009542854955	111.790239323678	-76.039966816661	26.422925814258

The $i = 1$ parameters can be derived from the constraints (6.B3).

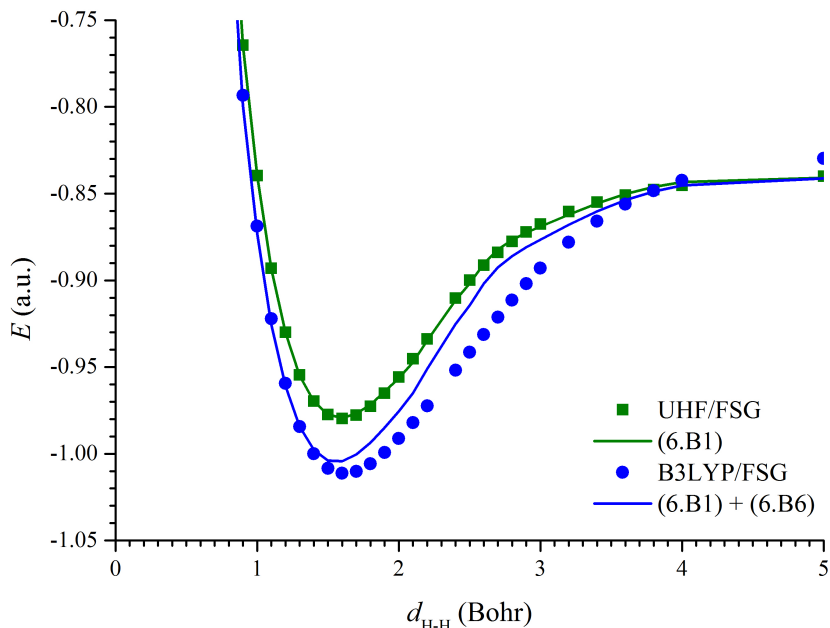


Figure 6.B2. Performance of the hybrid scheme on open singlet H_2 at UHF and B3LYP levels.

The extra correlation beyond UHF level was taken into account by the Wigner correlation functional[6],

$$\epsilon_c(\rho) = -\frac{\alpha}{1 + r_s/\beta} \quad (6.B4)$$

where $r_s \equiv \left(\frac{3}{4\pi\rho}\right)^{1/3}$, and α and β are parameters. Here we approximated r_s with the ‘‘overlap density’’ $\phi_1\phi_2$ (which is also Gaussian) size $s_o = \frac{s_1s_2}{\sqrt{s_1^2 + s_2^2}}$, scaled by the number of electrons in the overlap $N_o = 2S$,

$$r_s = \frac{s_o}{S^{1/3}} = \sqrt{\frac{s_1s_2}{2}} \exp\left[\frac{R_{12}^2}{3(s_1^2 + s_2^2)}\right] \quad (6.B5)$$

Assuming further that the overlap density is uniform, the correlation energy is simple evaluated as

$$E_C = N_o \epsilon_c(\rho) = -2S \frac{\alpha}{1 + r_s/\beta} \quad (6.B6)$$

The parameters $\alpha = 0.0248887589748153$ and $1/\beta = 0.1994033829664270$ were fitted against the Hooke's atom series, the ground state densities of which are Gaussian. The performance of this hybrid scheme is shown in Figure 6.B2, for both UHF and B3LYP levels of open singlet H_2 cases.

C. Integrals involved in energy evaluation with AMPERE

Algorithm for evaluation of integrals emergent in *ab initio* calculations with angular momentum projected pseudopotentials[11] has been proposed and implemented as a standard procedure[20–23]. Here, following the *ab initio* counterpart, we derived such algorithm for calculations of integrals arising from the AMPERE method.

In the derivation, four kinds of special functions are involved, including

$$\begin{aligned} \text{Error function} & : \quad \text{Erf}(x) = \frac{2}{\sqrt{\pi}} \int_0^x e^{-t^2} dt \\ \text{Dawson function} & : \quad F(x) = e^{-x^2} \int_0^x e^{t^2} dt = \frac{\sqrt{\pi}}{2} e^{-x^2} \text{Erfi}(x) \\ \text{Hybrid Dawson-error function} & : \quad H(x) = e^{-x^2} \int_0^x e^{t^2} \text{Erf}(t) dt \end{aligned}$$

where $\text{Erfi}(x) = -i\text{Erf}(ix) = \frac{2}{\sqrt{\pi}} \int_0^x e^{t^2} dt$ is the imaginary error function. The fourth one is the modified spherical Bessel function of the first kind $M_l(x)$, whose form is dependent of l , as listed below for the first two,

l	Notation	$M_l(x)$
0	s	$\frac{\sinh x}{x}$
1	p	$\frac{x \cosh x - \sinh x}{x^2}$

Type 1 integral

Type 1 integral arises from the term $\langle \phi_v | V_L(r_c) | \phi_v \rangle$, where

$$\phi_v = N \exp\left(-\frac{r_v^2}{s_v^2}\right) \quad \text{with } N \equiv \left(\frac{\sqrt{2}}{\sqrt{\pi}s_v}\right)^{\frac{3}{2}}$$

and $r_c \equiv |\vec{r} - \vec{R}_c|$, $r_v \equiv |\vec{r} - \vec{R}_v|$ for brevity. Together with (6.19), the term gives rise to integrals of the form

$$\chi_{Ln} \equiv C_{Ln} \int d\vec{r} \phi_v r_c^{n-2} \exp(-\zeta r_c^2) \phi_v \equiv C_{Ln} \int d\vec{r} \phi_v r_c^{n-2} \exp\left(-\frac{r_c^2}{s^2}\right) \phi_v \quad (6.C1)$$

where s can be roughly considered as the pseudopotential ‘‘size (or range)’’. Follow Ref. [21], and define

$$\begin{aligned} D &\equiv 4\pi N^2 \exp\left(-\frac{2R_{cv}^2}{s_v^2}\right) = \frac{8\sqrt{2}}{\sqrt{\pi}s_v^3} \exp\left(-\frac{2R_{cv}^2}{s_v^2}\right) \\ \vec{k} &\equiv -\frac{4(\vec{R}_v - \vec{R}_c)}{s_v^2} = -\frac{4\vec{R}_{cv}}{s_v^2}; \quad k = \frac{4R_{cv}}{s_v^2} \\ \alpha &\equiv \frac{2}{s_v^2} + \frac{1}{s^2} = \frac{1}{s_v^2} \left(2 + \frac{s_v^2}{s^2}\right) \end{aligned}$$

and a couple more,

$$\begin{aligned} x &\equiv \frac{k}{2\sqrt{\alpha}} = \frac{2R_{cv}}{s_v^2 \sqrt{\frac{1}{s_v^2} \left(2 + \frac{s_v^2}{s^2}\right)}} = \frac{2sR_{cv}}{s_v \sqrt{2s^2 + s_v^2}} \\ X &\equiv D \cdot \frac{\sqrt{\pi}}{4\alpha^{3/2}} \exp(x^2) \\ &= \frac{8\sqrt{2}}{\sqrt{\pi}s_v^3} \exp\left(-\frac{2R_{cv}^2}{s_v^2}\right) \cdot \frac{\sqrt{\pi}}{4\alpha^{3/2}} \exp\left(\frac{4s^2 R_{cv}^2}{s_v^2 (2s^2 + s_v^2)}\right) \\ &= \left(\frac{2}{s_v^2 \alpha}\right)^{3/2} \exp\left(-\frac{2R_{cv}^2}{2s^2 + s_v^2}\right) \end{aligned}$$

χ_{Ln} is simplified to

$$\chi_{Ln} = C_{Ln} \frac{D}{4\pi} \int d\vec{r} r_c^{n-2} \exp(-\alpha r_c^2) \exp(\vec{k} \cdot \vec{r}_c)$$

Here we don't follow the expansion used in Ref. [21] (Eq. (13)), but use the coordinate system with origin at \vec{R}_c , and z -axis along \vec{R}_{cv} ,

$$\begin{aligned} \chi_{Ln} &= C_{Ln} \frac{D}{4\pi} \int d\vec{r} r^{n-2} \exp(-\alpha r^2) \exp(-kr \cos \theta) \\ &= C_{Ln} \frac{D}{4\pi} \int_{r=0}^{\infty} r^2 dr r^{n-2} \exp(-\alpha r^2) \int_{\theta=0}^{\pi} \sin \theta d\theta \exp(-kr \cos \theta) \int_{\psi=0}^{2\pi} d\psi \\ &= C_{Ln} D \int_{r=0}^{\infty} dr r^n \exp(-\alpha r^2) \cdot \frac{\sinh(kr)}{kr} = C_{Ln} D \int_{r=0}^{\infty} dr r^n \exp(-\alpha r^2) M_{l=0}(kr) \\ &\equiv C_{Ln} D Q_{l=0}^n(k, \alpha) \end{aligned}$$

the last step uses the notation from Ref. [21]. $Q_{l=0}^n$'s are further evaluated as,

$$\begin{aligned} Q_{l=0}^{n=0}(k, \alpha) &= \frac{\sqrt{\pi}}{2\sqrt{\alpha}} \exp(x^2) \frac{F(x)}{x} \\ Q_{l=0}^{n=1}(k, \alpha) &= \frac{\sqrt{\pi}}{4\alpha} \exp(x^2) \frac{\text{Erf}(x)}{x} \\ Q_{l=0}^{n=2}(k, \alpha) &= \frac{\sqrt{\pi}}{4\alpha^{3/2}} \exp(x^2) \end{aligned}$$

Therefore,

$$\chi_{L0} = C_{L0} D Q_{l=0}^{n=0}(k, \alpha) = C_{L0} D \frac{\sqrt{\pi}}{2\sqrt{\alpha}} \exp(x^2) \frac{F(x)}{x} = C_{L0} X \cdot 2\alpha \frac{F(x)}{x} \quad (6.C2)$$

$$\chi_{L1} = C_{L1} D Q_{l=0}^{n=1}(k, \alpha) = C_{L1} D \frac{\sqrt{\pi}}{4\alpha} \exp(x^2) \frac{\text{Erf}(x)}{x} = C_{L1} X \cdot \sqrt{\alpha} \frac{\text{Erf}(x)}{x} \quad (6.C3)$$

$$\chi_{L2} = C_{L2} D Q_{l=0}^{n=2}(k, \alpha) = C_{L2} D \frac{\sqrt{\pi}}{4\alpha^{3/2}} \exp(x^2) = C_{L2} X \quad (6.C4)$$

Type 2 integral

Type 2 integral arises from the terms $\sum_{l=0}^{L-1} \langle \phi_v | V_{l-L}(r_c) \rangle$, which together with (6.19) gives rise to integrals of the form

$$\begin{aligned} \gamma_{ln} &\equiv C_{ln} \int_0^\infty r^2 dr \langle \phi_v | l0 \rangle r^{n-2} \exp(-\zeta r^2) \langle l0 | \phi_v \rangle \\ &\equiv C_{ln} \int_0^\infty dr \langle \phi_v | l0 \rangle r^n \exp\left(-\frac{r^2}{s^2}\right) \langle l0 | \phi_v \rangle \end{aligned} \quad (6.C5)$$

Note that the solid angle part is already integrated out with $Y_l^0(\theta, \phi)$, and the coordinate system is changed to with origin at \vec{R}_c , and z -axis along \vec{R}_{cv} . From (6.22),

$$\langle l0 | \phi_v \rangle = N \exp\left[-\frac{R_{cv}^2}{s_v^2}\right] \exp\left[-\frac{r_c^2}{s_v^2}\right] [4\pi(2l+1)]^{\frac{1}{2}} M_l\left(\frac{2R_{cv}}{s_v^2} r_c\right) \quad (6.C6)$$

Similarly, define

$$\begin{aligned} D &\equiv 4\pi N^2 \exp\left(-\frac{2R_{cv}^2}{s_v^2}\right) = \frac{8\sqrt{2}}{\sqrt{\pi} s_v^3} \exp\left(-\frac{2R_{cv}^2}{s_v^2}\right) \\ k &\equiv \frac{4R_{cv}}{s_v^2} \\ \alpha &\equiv \frac{2}{s_v^2} + \frac{1}{s^2} = \frac{1}{s_v^2} \left(2 + \frac{s_v^2}{s^2}\right) \\ x &\equiv \frac{k}{2\sqrt{\alpha}} = \frac{2sR_{cv}}{s_v \sqrt{2s^2 + s_v^2}} \end{aligned}$$

$$X \equiv D \cdot \frac{\sqrt{\pi}}{4\alpha^{3/2}} \exp(x^2) = \left(\frac{2}{s_v^2 \alpha}\right)^{3/2} \exp\left(-\frac{2R_{cv}^2}{2s^2 + s_v^2}\right)$$

and γ_{ln} is simplified to

$$\gamma_{ln} = C_{ln} D (2l + 1) \int_0^\infty dr r^n \exp(-\alpha r^2) \left[M_l \left(\frac{k}{2} r \right) \right]^2$$

By following the method proposed in Ref. [22] and [23], all relevant cases are evaluated as,

$$\gamma_{s0} = C_{s0} X \cdot 2\alpha \left[2 \frac{F(x)}{x} - \frac{1 - e^{-x^2}}{x^2} \right] \quad (6.C7)$$

$$\gamma_{s1} = C_{s1} X \cdot 2\sqrt{\alpha} \frac{H(x)}{x^2} \quad (6.C8)$$

$$\gamma_{s2} = C_{s2} X \cdot \frac{1 - e^{-x^2}}{x^2} \quad (6.C9)$$

$$\gamma_{p0} = C_{p0} X \cdot 4\alpha \left[-\frac{F(x)}{x} + \frac{3}{2} \cdot \frac{1 - e^{-x^2}}{x^2} - \frac{1 - \frac{1 - e^{-x^2}}{x^2}}{x^2} \right] \quad (6.C10)$$

$$\gamma_{p1} = C_{p1} X \cdot 6\sqrt{\alpha} \left[-\frac{H(x)}{x^2} - \frac{1}{\sqrt{\pi}} \frac{e^{-x^2}}{x^2} + \frac{\text{Erf}(x)}{x^3} - \frac{H(x)}{x^4} \right] \quad (6.C11)$$

$$\gamma_{p2} = C_{p2} X \cdot 3 \left\{ 2 \cdot \frac{1 - \frac{1 - e^{-x^2}}{x^2}}{x^2} - \frac{1 - e^{-x^2}}{x^2} \right\} \quad (6.C12)$$

D. Numerical implementation of AMPERE (pair_eff_ecp.h) in LAMMPS

Due to their recurrence and numerical instability near the origin, these formulas are implemented as individual functions in `pair_eff_ecp.h`:

<code>inline double erfoverx(double x, int d_order)</code>	:	$\frac{\text{Erf}(x)}{x}$
<code>inline double dawsonoverx(double x, int d_order)</code>	:	$\frac{F(x)}{x}$
<code>inline double hybridoverx2(double x, int d_order)</code>	:	$\frac{H(x)}{x^2}$
<code>inline double expoverx2(double x, int d_order)</code>	:	$\frac{1 - e^{-x^2}}{x^2}$
<code>inline double expoverx4(double x, int d_order)</code>	:	$\frac{1 - \frac{1 - e^{-x^2}}{x^2}}{x^2}$
<code>inline double l1n1terms(double x, int d_order)</code>	:	$\frac{\text{Erf}(x)}{x^3} - \frac{1}{\sqrt{\pi}} \frac{e^{-x^2}}{x^2} - \frac{H(x)}{x^4}$

The last entry only occurs in the $p1$ term, but gets separated out due to numerical instability concern. All functions have a second argument `int d_order`, which instructs the order of derivative to return.

Currently, only the original formulas (`d_order = 0`) and their first order derivatives (`d_order = 1`) are implemented.

After the above block, projection integrals are implemented as individual function for each case in Appendix C, and at last a wrap-up function is defined to parse a string `char *ECP_TYPE`, which dictates what projection terms are included in the AMPERE. Such set-up benefits both current development stage (for debug purpose) and future extensibility.

Please refer to `pair_eff_ecp.h` in LAMMPS for the detailed coding, and here some annotations are presented for better comprehension.

6.D.1 `inline double erfoverx(double x, int d_order)`

This piece of code is mostly based on the FORTRAN code of error function written by Cody, which uses algorithm in his 1969 paper[24]. The major changes are:

1. modified to evaluate $\frac{\text{Erf}(x)}{x}$ instead of $\text{Erf}(x)$;
2. the first order derivative is evaluated as $\frac{d\left[\frac{\text{Erf}(x)}{x}\right]}{dx} = \frac{2}{\sqrt{\pi}} \frac{e^{-x^2}}{x} - \frac{\text{Erf}(x)}{x^2}$, except for the first interval $|x| \leq 0.46875$, where $\frac{\text{Erf}(x)}{x}$ is approximated as $\frac{A(x)}{B(x)}$, so the first order derivative is evaluated as $\frac{A1(x)B(x) - A(x)B1(x)}{B^2(x)}$, where $A1(x)$ and $B1(x)$ are first order derivatives of $A(x)$ and $B(x)$, respectively.

6.D.2 `inline double dawsonoverx(double x, int d_order)`

This piece of code is based on the FORTRAN code of Dawson's integral also written by Cody, which uses algorithm in his 1970 paper[25]. The major changes are:

1. modified to evaluate $\frac{F(x)}{x}$ instead of $F(x)$;
2. the first order derivative is evaluated as

$$\left[\frac{F(x)}{x}\right]' = \frac{F'(x)x - F(x)}{x^2} = \frac{[1 - 2xF(x)]x - F(x)}{x^2} = \frac{1}{x} - \frac{F(x)}{x^2} (1 + 2x^2)$$

except for the first interval $|x| < 2.5$, where $\frac{F(x)}{x}$ is approximated as

$$\frac{P1(x)}{Q1(x)} = \frac{P_9 + P_8x^2 + \dots + P_0x^{18}}{Q_9 + Q_8x^2 + \dots + Q_0x^{18}}$$

so the first order derivative is evaluated as

$$\left[\frac{F(x)}{x}\right]' = \frac{1 - \frac{F(x)}{x}}{x} - 2F(x) = \frac{1 - \frac{P1(x)}{Q1(x)}}{x} - 2x \frac{P1(x)}{Q1(x)}$$

$$\begin{aligned}
&= \frac{Q_9 - P_9 + (Q_8 - P_8)x^2 + \cdots + (Q_0 - P_0)x^{18}}{x(Q_9 + Q_8x^2 + \cdots + Q_0x^{18})} - 2x \frac{P_1(x)}{Q_1(x)} \\
\because Q_9 = P_9 \quad \therefore &= \frac{(Q_8 - P_8)x + \cdots + (Q_0 - P_0)x^{17}}{Q_9 + Q_8x^2 + \cdots + Q_0x^{18}} - 2x \frac{P_1(x)}{Q_1(x)}
\end{aligned}$$

6.D.3 inline double hybridoverx2(double x, int d_order)

This piece of code evaluates the target formula in several intervals,

- when $|x| < 1$, series expansion is used

$$\begin{aligned}
H(x) &= e^{-x^2} \int_0^x e^{t^2} \operatorname{Erf}(t) dt \\
&= e^{-x^2} \int_0^x e^{t^2} \left(\frac{2}{\sqrt{\pi}} e^{-t^2} \sum_{n=0}^{\infty} \frac{2^n}{(2n+1)!!} t^{2n+1} \right) dt && \text{see (7.1.6) of [18]} \\
&= e^{-x^2} \sum_{n=0}^{\infty} \frac{2}{\sqrt{\pi}} \frac{2^n}{(2n+1)!!} \int_0^x t^{2n+1} dt \\
&= e^{-x^2} \sum_{n=0}^{\infty} \frac{1}{\sqrt{\pi}} \frac{2^n}{(2n+1)!!(n+1)} x^{2n+2} \\
\therefore \frac{H(x)}{x^2} &= e^{-x^2} \sum_{n=0}^{\infty} \frac{1}{\sqrt{\pi}} \frac{2^n}{(2n+1)!!(n+1)} x^{2n} \equiv e^{-x^2} \sum_{n=0}^{\infty} C_n x^{2n}
\end{aligned}$$

and the series is truncated at $n = 17$, where $C_n < 10^{-16}$. The first order derivative is evaluated as

$$\begin{aligned}
\left[\frac{H(x)}{x^2} \right]' &= -2xe^{-x^2} \sum_{n=0}^{\infty} \frac{1}{\sqrt{\pi}} \frac{2^n}{(2n+1)!!(n+1)} x^{2n} + e^{-x^2} \sum_{n=1}^{\infty} \frac{1}{\sqrt{\pi}} \frac{2^n \cdot 2n}{(2n+1)!!(n+1)} x^{2n-1} \\
&\equiv -2xe^{-x^2} \sum_{n=0}^{\infty} C_n x^{2n} + e^{-x^2} \sum_{n=1}^{\infty} C_{1n} x^{2n-1}
\end{aligned}$$

- when $1 \leq |x| < 10$, minimax rational approximation is used for each interval size of 1.0. Generally, $\frac{H(x)}{x^2}$ is approximated as $\frac{H(x)}{x^2} = \frac{P(x)}{Q(x)}$, and the orders of polynomials $P(x)$ and $Q(x)$ sufficient for accurate fitting are dependent of the target interval. In this range $1 \leq |x| < 10$, R(8,8) to R(4,4) are used to achieve accuracy of 10^{-16} . The first order derivative is evaluated as

$$\left[\frac{H(x)}{x^2} \right]' = \frac{P'(x)Q(x) - P(x)Q'(x)}{Q^2(x)}$$

- when $10 \leq |x|$, the asymptotic expansion from (77) of [20] is used,

$$\frac{H(x)}{x^2} = \frac{1}{x^2} \cdot \frac{1}{x} \sum_{n=0}^{\infty} \frac{(2n-1)!!}{2^{n+1}} \frac{1}{x^{2n}} \equiv \frac{1}{x^3} \sum_{n=0}^{\infty} A_n \frac{1}{x^{2n}}$$

and the series is truncated at $n = 12$. The first order derivative is evaluated as

$$\left[\frac{H(x)}{x^2} \right]' = \frac{1}{x^4} \sum_{n=0}^{\infty} \frac{(2n-1)!![-(2n+3)]}{2^{n+1}} \frac{1}{x^{2n}} \equiv \frac{1}{x^4} \sum_{n=0}^{\infty} A1_n \frac{1}{x^{2n}}$$

6.D.4 `inline double expoverx2(double x, int d_order)`

This piece of code uses Taylor expansion for $|x| < 1$,

$$\frac{1 - e^{-x^2}}{x^2} = e^{-x^2} \cdot \frac{e^{x^2} - 1}{x^2} = e^{-x^2} \sum_{n=0}^{\infty} \frac{x^{2n}}{(n+1)!} \equiv e^{-x^2} \sum_{n=0}^{\infty} C0_n x^{2n}$$

and the series is truncated at $n = 18$. The first order derivative is evaluated as

$$\begin{aligned} \left(\frac{1 - e^{-x^2}}{x^2} \right)' &= -2xe^{-x^2} \sum_{n=0}^{\infty} \frac{x^{2n}}{(n+1)!} + e^{-x^2} \sum_{n=1}^{\infty} \frac{2nx^{2n-1}}{(n+1)!} \\ &\equiv e^{-x^2} \left[-2x \sum_{n=0}^{\infty} C0_n x^{2n} + \sum_{n=1}^{\infty} C1_n x^{2n-1} \right] \end{aligned}$$

For $|x| \geq 1$, the original formula is evaluated, and the first order derivative is

$$\left(\frac{1 - e^{-x^2}}{x^2} \right)' = \frac{2 \left[(x^2 + 1) e^{-x^2} - 1 \right]}{x^3}$$

6.D.5 `inline double expoverx4(double x, int d_order)`

This piece of code uses Taylor expansion for $|x| < 1$,

$$\frac{1 - \frac{1 - e^{-x^2}}{x^2}}{x^2} = e^{-x^2} \left[\frac{e^{x^2} - \frac{e^{x^2} - 1}{x^2}}{x^2} \right] = e^{-x^2} \sum_{n=0}^{\infty} \frac{n+1}{(n+2)!} x^{2n} \equiv e^{-x^2} \sum_{n=0}^{\infty} C0_n x^{2n}$$

and the series is truncated at $n = 18$. The first order derivative is evaluated as

$$\begin{aligned} \left(\frac{1 - \frac{1 - e^{-x^2}}{x^2}}{x^2} \right)' &= -2xe^{-x^2} \sum_{n=0}^{\infty} \frac{n+1}{(n+2)!} x^{2n} + e^{-x^2} \sum_{n=1}^{\infty} \frac{(n+1) \cdot 2n}{(n+2)!} x^{2n-1} \\ &\equiv e^{-x^2} \left[-2x \sum_{n=0}^{\infty} C0_n x^{2n} + \sum_{n=1}^{\infty} C1_n x^{2n-1} \right] \end{aligned}$$

For $|x| \geq 1$, the original formula is evaluated, and the first order derivative is

$$\left(\frac{1 - \frac{1 - e^{-x^2}}{x^2}}{x^2} \right)' = -\frac{2 \left[(x^2 + 2) e^{-x^2} + x^2 - 2 \right]}{x^5}$$

6.D.6 inline double 11n1terms(double x, int d_order)

This piece of code uses Taylor expansion for $|x| < 1$,

$$\begin{aligned}
& \frac{\text{Erf}(x)}{x^3} - \frac{1}{\sqrt{\pi}} \frac{e^{-x^2}}{x^2} - \frac{H(x)}{x^4} = \frac{1}{x^2} \left[\frac{\text{Erf}(x)}{x} - \frac{1}{\sqrt{\pi}} e^{-x^2} - \frac{H(x)}{x^2} \right] \\
&= \frac{1}{x^2} \left[\frac{2}{\sqrt{\pi}} e^{-x^2} \sum_{n=0}^{\infty} \frac{2^n}{(2n+1)!!} x^{2n} - \frac{1}{\sqrt{\pi}} e^{-x^2} - \frac{1}{\sqrt{\pi}} e^{-x^2} \sum_{n=0}^{\infty} \frac{2^n}{(2n+1)!!(n+1)} x^{2n} \right] \\
&= \frac{1}{\sqrt{\pi}} e^{-x^2} \cdot \frac{1}{x^2} \left[2 + \sum_{n=1}^{\infty} \frac{2^{n+1}}{(2n+1)!!} x^{2n} - 1 - \left(1 + \sum_{n=1}^{\infty} \frac{2^n}{(2n+1)!!(n+1)} x^{2n} \right) \right] \\
&= \frac{1}{\sqrt{\pi}} e^{-x^2} \cdot \frac{1}{x^2} \sum_{n=1}^{\infty} \frac{2^n(2n+1)}{(2n+1)!!(n+1)} x^{2n} \\
&= e^{-x^2} \sum_{n=0}^{\infty} \frac{1}{\sqrt{\pi}} \frac{2^{n+1}}{(2n+1)!!(n+2)} x^{2n} \equiv e^{-x^2} \sum_{n=0}^{\infty} C_n x^{2n}
\end{aligned}$$

and the series is truncated at $n = 18$. The first order derivative is evaluated as

$$\begin{aligned}
& \left(\frac{\text{Erf}(x)}{x^3} - \frac{1}{\sqrt{\pi}} \frac{e^{-x^2}}{x^2} - \frac{H(x)}{x^4} \right)' \\
&= -2x e^{-x^2} \sum_{n=0}^{\infty} \frac{1}{\sqrt{\pi}} \frac{2^{n+1}}{(2n+1)!!(n+2)} x^{2n} + e^{-x^2} \sum_{n=1}^{\infty} \frac{1}{\sqrt{\pi}} \frac{2^{n+1} \cdot 2n}{(2n+1)!!(n+2)} x^{2n-1} \\
&\equiv e^{-x^2} \left[-2x \sum_{n=0}^{\infty} C_n x^{2n} + \sum_{n=1}^{\infty} C_{1n} x^{2n-1} \right]
\end{aligned}$$

For $|x| \geq 1$, the formula is evaluated as $\frac{1}{x^2} \left[\frac{\text{Erf}(x)}{x} - \frac{1}{\sqrt{\pi}} e^{-x^2} - \frac{H(x)}{x^2} \right]$, in order to utilize functions defined in 6.D.1 and 6.D.3, and the first order derivative is

$$\begin{aligned}
& \left(\frac{1}{x^2} \left[\frac{\text{Erf}(x)}{x} - \frac{1}{\sqrt{\pi}} e^{-x^2} - \frac{H(x)}{x^2} \right] \right)' \\
&= \frac{\left[\left(\frac{\text{Erf}(x)}{x} \right)' - \frac{1}{\sqrt{\pi}} (-2x) e^{-x^2} - \left(\frac{H(x)}{x^2} \right)' \right] x^2 - \left[\frac{\text{Erf}(x)}{x} - \frac{1}{\sqrt{\pi}} e^{-x^2} - \frac{H(x)}{x^2} \right] \cdot 2x}{x^4} \\
&= \frac{\left[\left(\frac{\text{Erf}(x)}{x} \right)' + \frac{2}{\sqrt{\pi}} x e^{-x^2} - \left(\frac{H(x)}{x^2} \right)' \right] x - 2 \left[\frac{\text{Erf}(x)}{x} - \frac{1}{\sqrt{\pi}} e^{-x^2} - \frac{H(x)}{x^2} \right]}{x^3}
\end{aligned}$$

6.D.7 projection terms

For each term, exactly the same variables are introduced as below for coding convenience,

$$\alpha \equiv \frac{2}{s_v^2} + \frac{1}{s^2}$$

$$\begin{aligned}
\frac{d\alpha}{ds_v} &= -\frac{4}{s_v^3} \\
\frac{\partial x}{\partial r_{cv}} &\equiv \frac{2}{s_v^2 \sqrt{\alpha}} \quad (\text{this is defined before } x \text{ as an implementation trick}) \\
x &\equiv \frac{\partial x}{\partial r_{cv}} r_{cv} = \frac{2sr_{cv}}{s_v \sqrt{2s^2 + s_v^2}} \\
\frac{\partial x}{\partial s_v} &= -x \left(\frac{1}{s_v} + \frac{s_v}{2s^2 + s_v^2} \right) \\
X &\equiv \left(\frac{2}{s_v^2 \alpha} \right)^{3/2} \exp \left(-\frac{2r_{cv}^2}{2s^2 + s_v^2} \right) \\
\frac{\partial X}{\partial r_{cv}} &= X \left(-\frac{4r_{cv}}{2s^2 + s_v^2} \right) \\
\frac{\partial X}{\partial s_v} &= \frac{X}{2s^2 + s_v^2} \left[-3s_v + \frac{4s_v r_{cv}^2}{2s^2 + s_v^2} \right]
\end{aligned}$$

and then the implementation is just as straightforward as formulated in Appendix C, with calling functions described above (6.D.1 – 6.D.6) on demand. Currently implemented are projection terms listed below,

```
inline void L0(double C, double s, double rcv, double sv, double *eecp, double *frcv, double *fsv)
```

L0 term (6.C2)

```
inline void L1(double C, double s, double rcv, double sv, double *eecp, double *frcv, double *fsv)
```

L1 term (6.C3)

```
inline void L2(double C, double s, double rcv, double sv, double *eecp, double *frcv, double *fsv)
```

L2 term (6.C4)

```
inline void s0(double C, double s, double rcv, double sv, double *eecp, double *frcv, double *fsv)
```

s0 term (6.C7)

```
inline void s1(double C, double s, double rcv, double sv, double *eecp, double *frcv, double *fsv)
```

s1 term (6.C8)

```
inline void s2(double C, double s, double rcv, double sv, double *eecp, double *frcv, double *fsv)
```

s2 term (6.C9)

```
inline void p0(double C, double s, double rcv, double sv, double *eecp, double *frcv, double *fsv)
```

p0 term (6.C10)

```
inline void p1(double C, double s, double rcv, double sv, double *eecp, double *frcv, double *fsv)
```

p1 term (6.C11)

```
inline void p2(double C, double s, double rcv, double sv, double *eecp, double *frcv, double *fsv)
```

p2 term (6.C12)

6.D.8 wrap-up function

```
inline void ECPwrapup(char *ECP_TYPE, double *ECP_PARAMS, double rcv, double sv, double *eecp,
                    double *frcv, double *fsv)
```

This final function simply scans the string `char *ECP_TYPE`, and calls all projection terms indicated, together with reading in corresponding parameters stored in `double *ECP_PARAMS`. With the flexible content of the string, arbitrary combinations can be made and tested in order to hunt the best AMPERE form.

References

- [1] Su, J. T. (2007) Ph.D. thesis (California Institute of Technology).
- [2] Su, J. T & Goddard, W. A. (2009) The dynamics of highly excited electronic systems: Applications of the electron force field. *J. Chem. Phys.* **131**, 244501.
- [3] Kato, T. (1957) On the eigenfunctions of many-particle systems in quantum mechanics. *Commun. Pure Appl. Math.* **10**, 151–177.
- [4] Plimpton, S. (1995) Fast parallel algorithms for short-range molecular-dynamics. *J. Comput. Phys.* **117**, 1–19.
- [5] Goddard, W. A, Dunning, T. H, Hunt, W. J, & Hay, P. J. (1973) Generalized valence bond description of bonding in low-lying states of molecules. *Acc. Chem. Res.* **6**, 368–376.
- [6] Wigner, E. (1938) Effects of the electron interaction on the energy levels of electrons in metals. *Trans. Faraday Soc.* **34**, 678–685.
- [7] Reeves, C. M & Fletcher, R. (1965) Use of Gaussian functions in the calculation of wavefunctions for small molecules. III. The orbital basis and its effect on valence. *J. Chem. Phys.* **42**, 4073–4081.
- [8] Oohata, K, Taketa, H, & Huzinaga, S. (1966) Gaussian expansions of atomic orbitals. *J. Phys. Soc. Jpn.* **21**, 2306–2313.
- [9] Hehre, W. J, Stewart, R. F, & Pople, J. A. (1969) Self-consistent molecular-orbital methods. I. Use of Gaussian expansions of Slater-type atomic orbitals. *J. Chem. Phys.* **51**, 2657–2664.
- [10] Troullier, N & Martins, J. L. (1991) Efficient pseudopotentials for plane-wave calculations. *Phys. Rev. B* **43**, 1993–2006.
- [11] Kahn, L. R & Goddard, W. A. (1972) Ab initio effective potentials for use in molecular calculations. *J. Chem. Phys.* **56**, 2685–2701.

- [12] Melius, C. F & Goddard, W. A. (1974) Ab initio effective potentials for use in molecular quantum mechanics. *Phys. Rev. A* **10**, 1528–1540.
- [13] Fuentealba, P. (1982) On the reliability of semiempirical pseudopotentials: dipole polarisability of the alkali atoms. *J. Phys. B: At. Mol. Phys.* **15**, L555.
- [14] Müller, W, Flesch, J, & Meyer, W. (1984) Treatment of intershell correlation effects in ab initio calculations by use of core polarization potentials. Method and application to alkali and alkaline earth atoms. *J. Chem. Phys.* **80**, 3297–3310.
- [15] Müller, W & Meyer, W. (1984) Ground-state properties of alkali dimers and their cations (including the elements Li, Na, and K) from ab initio calculations with effective core polarization potentials. *J. Chem. Phys.* **80**, 3311–3320.
- [16] Stoll, H, Fuentealba, P, Dolg, M, Flad, J, Szentpály, L. v, & Preuss, H. (1983) Cu and Ag as one-valence-electron atoms: Pseudopotential results for Cu_2 , Ag_2 , CuH , AgH , and the corresponding cations. *J. Chem. Phys.* **79**, 5532–5542.
- [17] Igel, G, Wedig, U, Dolg, M, Fuentealba, P, Preuss, H, Stoll, H, & Frey, R. (1984) Cu and Ag as one-valence-electron atoms: Pseudopotential CI results for CuO and AgO . *J. Chem. Phys.* **81**, 2737–2740.
- [18] Abramowitz, M & Stegun, I. A. (1964) *Handbook of Mathematical Functions with Formulas, Graphs, and Mathematical Tables*. (Dover Publications, Inc., New York), 9th Dover printing, 10th GPO printing edition.
- [19] Kolos, W & Wolniewicz, L. (1965) Potential-energy curves for the $X^1\Sigma_g^+$, $b^3\Sigma_u^+$, and $C^1\Pi_u$ states of the hydrogen molecule. *J. Chem. Phys.* **43**, 2429–2441.
- [20] Kahn, L. R, Baybutt, P, & Truhlar, D. G. (1976) *Ab initio* effective core potentials: Reduction of all-electron molecular structure calculations to calculations involving only valence electrons. *J. Chem. Phys.* **65**, 3826–3853.
- [21] McMurchie, L. E & Davidson, E. R. (1981) Calculation of integrals over *ab initio* pseudopotentials. *J. Comput. Phys.* **44**, 289–301.
- [22] Kolář, M. (1981) Pseudopotential matrix elements in the Gaussian basis. *Comput. Phys. Commun.* **23**, 275–286.
- [23] Bode, B. M & Gordon, M. S. (1999) Fast computation of analytical second derivatives with effective core potentials: Application to Si_8C_{12} , Ge_8C_{12} , and Sn_8C_{12} . *J. Chem. Phys.* **111**, 8778–8784.

- [24] Cody, W. J. (1969) Rational Chebyshev approximations for the error function. *Math. Comput.* **23**, 631–637.
- [25] Cody, W. J, Paciorek, K. A, & Thacher, H. C. (1970) Chebyshev approximations for Dawson's integral. *Math. Comput.* **24**, 171–178.